

AD A 042844

AFAL-TR-77-50

2

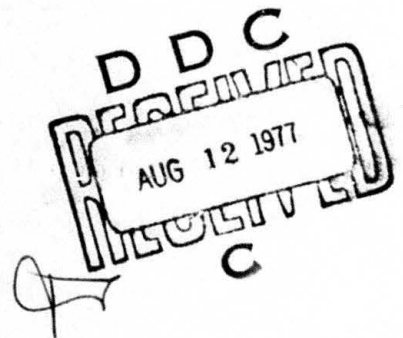
MULTISENSOR FINAL REPORT

The Charles Stark Draper Laboratory, Inc.

June 1977

TECHNICAL REPORT AFAL-TR-77-50

Final Report for Period 1 January - 31 December 1976



Approved for public release; distribution unlimited

AIR FORCE AVIONICS LABORATORY
AIR FORCE WRIGHT AERONAUTICAL LABORATORIES
AIR FORCE SYSTEMS COMMAND
WRIGHT-PATTERSON AIR FORCE BASE, OHIO 45433

DDC FILE COPY

NOTICE

When Government drawings, specifications, or other data are used for any purpose other than in connection with a definitely related Government procurement operation, the United States Government thereby incurs no responsibility nor any obligation whatsoever; and the fact that the government may have formulated, furnished, or in any way supplied the said drawings, specifications, or other data, is not to be regarded by implication or otherwise as in any manner licensing the holder or any other person or corporation, or conveying any rights or permission to manufacture, use, or sell any patented invention that may in any way be related thereto.

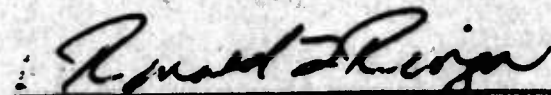
This report has been reviewed by the Information Office (IO) and is releasable to the National Technical Information Service (NTIS). At NTIS, it will be available to the general public, including foreign nations.

This technical report has been reviewed and is approved for publication.



EDWIN V. HARRINGTON, JR., CAPT, USAF
Technical Manager, Reference Systems
Technology Group, Reference Systems Branch

FOR THE COMMANDER



RONALD L. RINGO
Chief, Reference Systems Branch
Reconnaissance & Weapon Delivery Division

Copies of this report should not be returned unless return is required by security considerations, contractual obligations, or notice on a specific document.

| REPORT DOCUMENTATION PAGE | | READ INSTRUCTIONS BEFORE COMPLETING FORM |
|---|---|---|
| 1. REPORT NUMBER AFAL-TR-77-50 | 2. GOVT ACCESSION NO. | 3. RECIPIENT'S CATALOG NUMBER (21) |
| 4. TITLE (and Subtitle) MULTISENSOR FINAL REPORT ✓ | 5. TYPE OF REPORT & PERIOD COVERED Final Report January - December 1976 | 6. PERFORMING ORG. REPORT NUMBER R-1051 |
| 7. AUTHOR(s) M. Weinberg R. Lawson | 8. CONTRACT OR GRANT NUMBER(s) F33615-76-C-1048 / new | |
| 9. PERFORMING ORGANIZATION NAME AND ADDRESS The Charles Stark Draper Laboratory, Inc. 555 Technology Square Cambridge, Massachusetts 02139 ✓ | 10. PROGRAM ELEMENT, PROJECT, TASK AREA & WORK UNIT NUMBERS 62204F 60951206 | |
| 11. CONTROLLING OFFICE NAME AND ADDRESS Air Force Avionics Laboratory Air Force Wright Aeronautical Laboratories Air Force Systems Command Wright-Patterson Air Force Base, Ohio 45433 | 12. REPORT DATE January 1977 | 13. NUMBER OF PAGES 159 |
| 14. MONITORING AGENCY NAME & ADDRESS (if different from Controlling Office) ONRRR Massachusetts Institute of Technology Rm 5-19-628 Cambridge, Massachusetts 02139 (12) 160 p. | 15. SECURITY CLASS. (of this report) Unclassified | 16. DECLASSIFICATION/DOWNGRADING SCHEDULE |
| 16. DISTRIBUTION STATEMENT (of this Report) Approved for public release; distribution unlimited. | | |
| 17. DISTRIBUTION STATEMENT (of the abstract entered in Block 20, if different from Report) | | |
| 18. SUPPLEMENTARY NOTES | | |
| 19. KEY WORDS (Continue on reverse side if necessary and identify by block number) Multisensor Inertial Components Two-Function Instrument Gyroscope Accelerometer Single-Degree-Of-Freedom Floated Gyroscope | | |
| 20. ABSTRACT (Continue on reverse side if necessary and identify by block number) The Charles Stark Draper Laboratory (CSDL) multisensor is based upon a single-degree-of-freedom integrating gyroscope with the support axis purposely unbalanced to obtain pendulosity. Acceleration is obtained by monitoring the torque rebalance about the transverse axes while the instrument's symmetric axis contains angular rate information. The multifunction capability of each component will permit low cost, redundant systems in the 1 nmi/hr class. Three multisensors can instrument a six function platform with three redundant channels. The testing of a previously constructed feasibility multisensor is described. The test results are combined with analyses and design studies to project the performance of a ten size (nominal one inch diameter) instrument. | | |

↙ The feasibility instrument was constructed by modifying existing 18-size single-degree-of-freedom gyro hardware. Feasibility testing has demonstrated the basic potential of the multisensor concept for avionics, tactical guidance, and navigation applications. Although not optimized as a multisensor, the feasibility device performed, as follows, in a two position, one hundred hour stability test.

- (1) Gyro Bias stability of 0.1 meru (0.0015 deg/hr) and acceleration sensitive drift of 0.3 meru/g (0.0045 deg/hr/g).
- (2) Accelerometer Bias stability of 50 μ g and scale factor stability of 75 ppm. The dynamic and thermal characteristics of the feasibility instrument are well understood.

To obtain similar dynamic performance about the three axes, the projected 10-size multisensor utilizes very low viscosity damping fluid. The active control is wound and connected so that suitable dynamic performance is achieved, although the multisensor no longer functions as a traditional single-degree-of-freedom device. Other advantages of the low-viscosity fluid are quick warm-up reaction times, pull-in times in the order of one second, and rapid instrument fill. With increased pendulosity and advantages gained from geometric scaling of thermal errors, the accelerometer performance should improve significantly.

In addition to the multisensor, the demonstrated ability to sum torque about a transverse axis forms the foundation for a family of multifunction devices which could be constructed from similar hardware. Thus, economic development and fabrication of multisensors, two-degree-of-freedom gyros, two-degree-of-freedom accelerometers, three-degree-of-freedom angular rate sensors, and multisensors is possible.

↗

FOREWARD

This report was prepared under Project 62204F, covering the period 1 January through 31 December 1976, through Air Force Contract F33615-76-C-1048 by The Charles Stark Draper Laboratory, Inc., Cambridge, Massachusetts 02139.

The monitoring Air Force Project Engineer is Capt. Edwin V. Harrington, Jr., AFAL/RWN-2, Air Force Avionics Laboratory, Air Force Systems Command, Wright-Patterson Air Force Base, Ohio 45433. This report was submitted by the author in June 1977.

| | |
|-------------------------------|---|
| ACCESSION for | |
| NTIS | State Section <input checked="" type="checkbox"/> |
| DDC | Field Section <input type="checkbox"/> |
| Headquarters | <input type="checkbox"/> |
| USC | <input type="checkbox"/> |
| BY | |
| DISTRIBUTION/AVL ADITL COPIES | |
| 1. 1 | |
| A | |

TABLE OF CONTENTS

| SECTION | PAGE |
|---|------|
| 1. INTRODUCTION. | 1 |
| 1.1 GENERAL. | 1 |
| 1.2 SINGLE-DEGREE-OF-FREEDOM INSTRUMENTS | 1 |
| 1.3 MULTIFUNCTION INSTRUMENTS. | 3 |
| 1.4 ORGANIZATION OF REPORT | 4 |
| 2. FEASIBILITY MULTISENSOR TEST. | 5 |
| 2.1 SUMMARY. | 5 |
| 2.2 INSTRUMENT DESCRIPTION | 6 |
| 2.3 BUILD INTEGRITY. | 7 |
| 2.4 DATA PROCESSING. | 10 |
| 2.5 SENSITIVITY TESTS. | 11 |
| 2.6 STABILITY TESTS. | 17 |
| 2.7 ONE-POSITION STABILITY TEST. | 20 |
| 2.8 REACTION/WARM-UP CHARACTERISTIC. | 22 |
| 3. DESIGN CONSIDERATIONS | 75 |
| 3.1 GENERAL. | 75 |
| 3.2 EQUATIONS OF MOTION. | 75 |
| 3.3 MAGNETIC INTERACTIONS AND LOCATION OF AXES | 78 |
| 3.4 THERMALLY INDUCED ERRORS | 80 |
| 3.5 ACCELEROMETER ERRORS INTRODUCED BY WHEEL ANISOELASTICITY AND WHEEL HUNT | 81 |
| 3.6 ACCELEROMETER RESOLUTION CONSIDERING FORCER ELASTIC RESTRAINT AND SIGNAL GENERATOR NOISE AND NULL SHIFT | 82 |
| 3.7 REACTION TORQUES CAUSED BY AXIAL SUSPENSION. | 84 |
| 3.8 ADJUSTMENTS OF DAMPING CONSTANTS-INTERACTION BETWEEN INPUT AND OUTPUT AXES COUPLED THROUGH ANGULAR MOMENTUM | 84 |
| 3.9 CONTROL OF ROTATIONAL AND TRANSLATIONAL MOTIONS. | 86 |
| 3.10 MAXIMUM CASE RATES | 88 |



TABLE OF CONTENTS (Continued)

| SECTION | PAGE |
|---|------|
| 4. DESIGN PROTECTION | 91 |
| 5. CONCLUSIONS AND RECOMMENDATIONS | 97 |
| 5.1 CONCLUSIONS | 97 |
| 5.2 RECOMMENDATIONS | 95 |
| APPENDIX A MULTISENSOR EQUATIONS OF MOTION. | 101 |
| A.1 SUMMARY. | 101 |
| A.2 NOMENCLATURE | 101 |
| A.3 EQUATIONS OF MOTION. | 103 |
| APPENDIX B COUPLED ROTATIONAL AND TRANSLATIONAL MOTION. | 109 |
| B.1 SUMMARY. | 109 |
| B.2 BASIC MODEL. | 109 |
| B.3 EQUATIONS OF MOTION WITH SUSPENSION FORCES | 110 |
| B.4 DISCUSSION OF DECOUPLING | 111 |
| B.5 END DISPLACEMENT MEASUREMENT WITHOUT CROSS- FEEDBACK | 112 |
| B.6 THE MULTISENSOR RADIAL SUSPENSION. | 114 |
| APPENDIX C TWO-DEGREE-OF-FREEDOM FLOAT DYNAMICS WITH WHEEL COUPLING | 119 |
| C.1 SUMMARY. | 119 |
| C.2 SCOPE. | 119 |
| C.3 JUSTIFICATION FOR NEGLECTING INERTIA | 120 |
| C.4 REDUCED MOTION EQUATIONS | 121 |
| C.5 GENERAL EQUATIONS FOR TWO-DEGREE-OF-FREEDOM WITH CONTROL | 123 |
| C.6 MULTISENSOR ACTIVE CONTROLS. | 125 |
| C.7 LOW DAMPING CONFIGURATION. | 126 |
| APPENDIX D ACCELEROMETER RESOLUTION CONSIDERING ELASTIC RESTRAINT AND SIGNAL GENERATOR NOISE | 131 |
| D.1 SUMMARY. | 131 |
| D.2 ELASTIC RESTRAINT. | 131 |
| D.3 ACCELEROMETER EQUATIONS OF MOTION. | 133 |
| D.4 LOOP COMPENSATION. | 135 |
| D.5 DISCUSSION OF TRANSFER FUNCTIONS | 135 |
| D.6 MEASURED TORQUE UNCERTAINTY CAUSED BY SG NOISE IN THE FEASIBILITY INSTRUMENT | 137 |

TABLE OF CONTENTS (Continued)

| SECTION | PAGE |
|--|------|
| APPENDIX E CONVECTION TORQUES ABOUT TRANSVERSE AXIS | 143 |
| E.1 SUMMARY. | 143 |
| E.2 DISCUSSION | 143 |
| APPENDIX F STATIC CROSS-COUPLING IN MULTISENSORS. | 149 |
| F.1 SUMMARY. | 149 |
| F.2 MULTISENSOR MODEL AT STEADY-STATE. | 149 |
| F.3 COMMENTS | 155 |
| REFERENCES. | 157 |

LIST OF ILLUSTRATIONS

| FIGURE | | PAGE |
|--------|--|------|
| 1-1 | Multisensor | 2 |
| 2-1 | Feasibility multisensor | 7 |
| 2-2 | Feasibility multisensor mounted in test fixture | 8 |
| 2-3 | Multisensor normal and temperature gradient distribution. | 14 |
| 2-4 | Performance of SG and forcer. | 16 |
| 2-5 | Multisensor position for scale factor and bias calibration tests | 17 |
| 2-6 | I-Axis acceleration scale factor temperature sensitivity (uniform temperature change). | 24 |
| 2-7 | S-Axis acceleration scale factor temperature sensitivity (uniform temperature change). | 24 |
| 2-8 | I-Axis acceleration bias temperature sensitivity (uniform temperature change). | 25 |
| 2-9 | S-Axis acceleration bias temperature sensitivity (uniform temperature change). | 25 |
| 2-10 | Gyro bias drift temperature sensitivity (uniform temperature change) | 26 |
| 2-11 | Gyro acceleration drift temperature sensitivity (uniform temperature change). | 26 |
| 2-12 | I-Axis acceleration scale factor wheel power sensitivity (± 5 percent). | 27 |
| 2-13 | S-Axis acceleration scale factor wheel power sensitivity (± 5 percent). | 27 |
| 2-14 | I-Axis acceleration bias wheel power sensitivity. | 28 |
| 2-15 | S-Axis acceleration bias wheel power sensitivity. | 28 |
| 2-16 | Gyro bias drift wheel power sensitivity | 29 |
| 2-17 | Gyro acceleration drift wheel power sensitivity | 29 |
| 2-18 | I-Axis acceleration scale factor sensitivity to SG primary excitation (9.6 kHz). | 30 |
| 2-19 | S-Axis acceleration scale factor sensitivity to SG primary excitation (9.6 kHz). | 30 |
| 2-20 | I-Axis acceleration bias sensitivity to SG primary excitation (9.6 kHz). | 31 |

LIST OF ILLUSTRATIONS (Continued)

| FIGURE | | PAGE |
|--------|---|------|
| 2-21 | S-Axis acceleration bias sensitivity to SG primary excitation (9.6 kHz) | 31 |
| 2-22 | Gyro bias sensitivity to SG primary excitation (9.6 kHz) | 32 |
| 2-23 | Gyro acceleration drift sensitivity to SG primary excitation (9.6 kHz) | 32 |
| 2-24 | I-Axis scale factor sensitivity to axial position . . . | 33 |
| 2-25 | S-Axis scale factor sensitivity to axial position . . . | 33 |
| 2-26 | I-Axis acceleration bias sensitivity to axial position. | 34 |
| 2-27 | S-Axis acceleration bias sensitivity to axial position. | 34 |
| 2-28 | I-Axis acceleration scale factor sensitivity to I-axis displacement | 35 |
| 2-29 | I-Axis scale factor sensitivity to S-Axis displacement. | 35 |
| 2-30 | S-Axis acceleration scale factor sensitivity to S-axis displacement | 36 |
| 2-31 | S-Axis scale factor sensitivity to I-axis displacement. | 36 |
| 2-32 | I-Axis acceleration bias sensitivity to I-axis displacement. | 37 |
| 2-33 | I-Axis acceleration bias sensitivity to S-axis displacement. | 37 |
| 2-34 | S-Axis acceleration bias sensitivity to S-axis displacement. | 38 |
| 2-35 | S-Axis acceleration bias sensitivity to I-axis displacement. | 38 |
| 2-36 | I-Axis acceleration scale factor stability. | 39 |
| 2-37 | S-Axis acceleration scale factor stability. | 40 |
| 2-38 | I-Axis acceleration bias stability 10/22 - 10/26/76 . . . | 41 |
| 2-39 | S-Axis acceleration bias stability 10/22 - 10/26/76 . . . | 42 |
| 2-40 | Gyro BD stability 10/22 - 10/26/76. | 43 |
| 2-41 | Gyro AD stability 10/22 - 10/26/76. | 44 |
| 2-42 | SG end housing temperature 10/22 - 10/26/76 | 45 |
| 2-43 | Case temperature 10/22 - 10/26/76 | 46 |
| 2-44 | Base temperature 10/22 - 10/26/76 | 47 |
| 2-45 | 72-hour, I-axis acceleration drift (IA EA). | 48 |
| 2-46 | 72-hour, S-axis acceleration drift (SA EA) | 49 |

LIST OF ILLUSTRATIONS (Continued)

| FIGURE | | PAGE |
|--------|---|------|
| 2-47 | 72-hour gyro drift (IA \perp EA) | 50 |
| 2-48 | 72-hour, SG end housing temperature | 51 |
| 2-49 | 72-hour, table tilt, north-south plane. | 52 |
| 2-50 | 72-hour, table tilt, east-west plane. | 53 |
| 2-51 | 72-hour normalized wheel power. | 54 |
| 2-52 | I-Axis accelerometer power spectrum (trend removed) . . | 55 |
| 2-53 | S-Axis accelerometer power spectrum (trend removed) . . | 55 |
| 2-54 | Power spectrum of gyro torque (includes trend). | 56 |
| 2-55 | Power spectrum of temperature (includes trend). | 57 |
| 2-56 | Power spectrum of north-south table tilt (includes trend). | 58 |
| 2-57 | Power spectrum of east-west table tilt (includes trend). | 59 |
| 2-58 | Power spectrum of wheel power | 60 |
| 2-59 | SG end housing temperature (12/13/76) | 61 |
| 2-60 | SI forcer temperature reaction. | 62 |
| 2-61 | TI forcer temperature reaction. | 63 |
| 2-62 | I-Axis acceleration temperature reaction (IA vertical) (12/13/76). | 64 |
| 2-63 | SS forcer temperature reaction (SA horizontal) (12/13/76). | 65 |
| 2-64 | TS forcer temperature reaction (SA horizontal) (12/13/76). | 66 |
| 2-65 | S-Axis acceleration temperature reaction (SA horizontal) (12/13/76). | 67 |
| 2-66 | Gyro torque during temperature warm-up (IA down \perp EA) (11/4/76) | 68 |
| 2-67 | I-Axis acceleration, SG end forcer (SI) output during axial position. | 69 |
| 2-68 | I-Axis acceleration, TG end forcer (TI) output during axial pull-in | 70 |
| 2-69 | Gyro torque during axial pull-in. | 71 |
| 2-70 | SG end housing temperature during axial pull-in | 72 |
| 2-71 | TG end housing temperature during axial pull-in | 73 |
| 3-1 | Schematic of radial forcer connections, individual end control | 87 |
| 3-2 | Schematic of radial forcer connection, separate rotational and translational mode control | 88 |

LIST OF ILLUSTRATIONS (Continued)

| FIGURE | | PAGE |
|--------|--|------|
| 4-1 | Multisensor (low damping - 10 size) | 92 |
| B-1 | Coordinates for rotational-translational model. | 116 |
| B-2 | Root locus for multisensor suspension | 116 |
| B-3 | Time traces for active suspension (Equation B.16) end measurement, no crossfeedback | 117 |
| C-1 | Schematic root locus justifying omission of inertia from motion equation. Poles at origin will only be moved in shaded area far from fast poles. | 122 |
| C-2 | Coupled integral loops. Float angles for steps in input torque. | 128 |
| C-3 | Coupled integral loops. Rebalance torques for steps in input torques. | 129 |
| D-1 | Schematic of push-pull clapper forces | 132 |
| D-2 | Block diagram of idealized single loop of multisensor . | 134 |
| D-3 | Bode plot measured versus applied torque for multi- sensor accelerometer. | 136 |
| E-1 | Coordinates for convection analysis | 144 |
| F-1 | Schematic of forces and torques in multisensor. | 154 |

LIST OF TABLES

| TABLE | | PAGE |
|-------|---|------|
| 2-1 | BUILD INTEGRITY TEST PARAMETERS | 9 |
| 2-2 | FEASIBILITY INSTRUMENT SENSITIVITY TEST RESULTS | 13 |
| 2-3 | MULTISENSOR STABILITY GOALS AND TEST RESULTS (100 HOURS) | 19 |
| 4-1 | DESIGN PARAMETERS FOR 10-SIZE MULTISENSOR | 93 |
| C-1 | VALUES FOR INTEGRAL-INTEGRAL STUDY. | 125 |
| C-2 | POLES AS C_I CHANGES FOR INTEGRAL-INTEGRAL STUDY | 126 |
| D-1 | RMS TORQUE UNCERTAINTIES CAUSED BY SG NOISE | 139 |

SECTION 1

INTRODUCTION

1.1 GENERAL

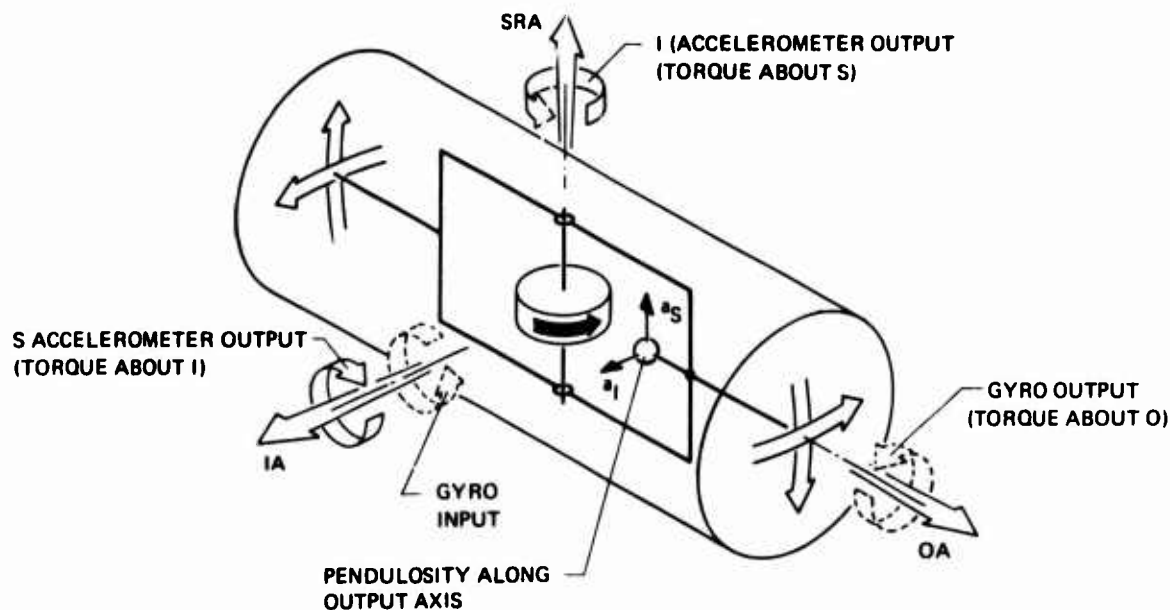
Inertial systems must sense six quantities (three angular position and three acceleration). Current mechanization of such systems requires six single-degree-of-freedom instruments or a combination of two-degree-of-freedom and single-degree-of-freedom instruments (totaling four or five instruments). Multisensors are currently being developed at CSDL and their successful development will reduce the number of instruments needed for navigation to three, or possibly two, thus, both platform size and total system cost will be reduced. The multiple outputs could also be used to increase system reliability.

The multisensor program leads directly into a family of multi-function instruments which will decrease the costs of navigation components and systems. The multisensor also contributes immediately to high accuracy gyro technology. These benefits will be reviewed after single-degree-of-freedom instruments and their extension to multisensors are discussed.

1.2 SINGLE-DEGREE-OF-FREEDOM INSTRUMENTS

A floated single-degree-of-freedom gyro consists of a case, a float, a wheel, and electromagnetic sensors and torquers. The wheel is spun at high angular velocity and is mounted rigidly to the float (see Figure 1-1). The float-case gap is filled with viscous fluid having a density such that almost no residual gravity-buoyancy force is exerted on the float. Small mismatches in fluid density and float unbalance are countered by a magnetic suspension which centers the float with respect to the case. Angular velocity of the case (hence, torques on the wheel) about the input axis (see Figure 1-1) interacts with the wheel angular momentum to rotate the float about the output axis. This angular rotation is sensed by an electromagnetic signal generator, and is used in feedback loops with a stabilized platform or with an electromagnetic torquer mounted inside the instrument case to maintain the float at null position. The instrument output is either the stable-platform position or the torque required to null the float.

As illustrated in Figure 1-1, the CSDL multisensor is a single-degree-of-freedom floated gyroscope with pendulosity intentionally added along the gyro output axis. Although a cylindrical float is depicted in Figure 1-1, analyses indicate that noncylindrical shapes merit consideration. The gyro functions conventionally, while — because of the added pendulosity — specific force inputs along the spin or input axes produce torques about the input and spin axes respectively. These applied torques are rebalanced by the float suspension to maintain a null position. The rebalance torques are measurement outputs which are proportional to the input specific forces.



NOTE THAT EITHER ONE OR BOTH OF THE
ACCELEROMETER CHANNELS CAN BE USED.

8/73 3373

Figure 1-1. Multisensor concept.

The CSDL multisensor is simple; conceptually, the instrument performs no functions beyond those required of a conventional single-degree-of-freedom gyro. The gyro functions as a traditional single-degree-of-freedom gyro, while mass unbalance has always been countered by suspension forces. The main difference between the multisensor and conventional instruments is the greater output-axis unbalance and the additional measurements which must be taken to sense specific force.

Autonetics, Northrop, and Litton have investigated unrelated multisensor concepts. Autonetics employed an electrostatically suspended two-degree-of-freedom gyro. A tuned rotor suspension with an essentially independent gyro and accelerometer was studied by Litton. The Northrop device used quartz crystals for sensing a pressure differential in liquid mercury to sense gyro function, and used compressed crystals to support the instrument and sense acceleration. Teledyne, also, is actively pursuing multisensor development.

1.3 MULTIFUNCTION INSTRUMENTS

Traditionally, single-degree-of-freedom instruments have utilized the cylinder's axis of symmetry as the measurement axis. Rather than merely demonstrating an added accelerometer function, the multisensor uses the transverse axis as a measurement axis. Considerable fabrication and maintenance cost savings could be realized from the following devices, assembled from one design with only modification to the float:

- (1) Three-degree-of-freedom rate sensor where the float is constructed with no rotating parts and the center of buoyancy nominally coincides with the center of gravity.
- (2) Two-degree-of-freedom gyroscope, in which the float contains a spinning angular momentum generator.
- (3) Two-degree-of-freedom accelerometer whose float contains no rotating members but incorporates a mass unbalance to effect an acceleration sensitive response.
- (4) Multisensor which features both rotating wheel and mass unbalance.

The multisensor program is contributing directly to the development of high performance gyroscopes. To realize loop response required for navigation, the multisensor incorporates active suspensions which are planned for use in advanced gyroscopes. Multisensor analyses and experiments study radial forces and motions, phenomena which must be understood in order to design advanced third and fourth generation single-degree-of-freedom instruments. In designing multisensors, damping constants and their effects are carefully considered, thereby gaining insight for other programs which seek to change damping by decreasing fluid viscosity or by increasing the fluid gaps.

This program combined analyses and testing of a feasibility instrument in order to predict the performance of an optimized multisensor. The following were used as guidelines:

- (1) Traditional gyro drift stability less than one meru (0.015 deg/hr);
- (2) Accelerometer stability of 100 μ g bias and 50 ppm scale factor;
- (3) Strapdown application with maximum case rate of 300 deg/s.

The feasibility device was constructed under internal funding, from existing 18 IRIG Mod D hardware, to minimize cost and permit testing in a short time scale. The feasibility device is not optimized in any sense and is merely intended to enable projection of optimized configurations. Previous testing was minimal because of suspected contamination in the fluid. Except for new flex leads, the removal of contamination, and a fluid change, the instrument was unchanged from previous builds.

Previous testing and analytic work resulted in the following changes external to the instrument prior to test:

- (1) The axial suspension was made active to minimize reaction torques (Paragraph 3.7);
- (2) The accelerometer and gyro loops were built to implement the desired control laws and enhance experimental flexibility;
- (3) The instrument mounting arrangement was redesigned to assure end-to-end thermal symmetry (Paragraph 3.4).

1.4 ORGANIZATION OF REPORT

Section 2 describes the feasibility instrument and test results. In Section 3, the tests results and analyses, which are included as appendices, are combined to clarify the principal factors contributing to multisensor performance. Section 4 presents the design recommended for a 10 size (approximately one inch case diameter) instrument. The report is summarized in Section 5 with recommendations for further testing which should be accomplished before finalizing the multisensor design.

SECTION 2

FEASIBILITY MULTISENSOR TEST

2.1 SUMMARY

The feasibility multisensor test program was designed as an experimental investigation rather than a qualification test, although performance guidelines were stated (see Section 1). Understanding the instrument's behavior must be emphasized. Analyses have shown that the present feasibility instrument is probably not an optimal configuration. That knowledge coupled with analysis (see Section 4) will indicate improvements and the potential of future multisensor designs.

The performance objectives are 1 meru (0.015 deg/hr) gyro drift stability, and 100 μ g bias and 50 ppm scale factor stability for the accelerometer function. The 100 hour drift stability test accelerometer uncertainties about the mean are 80 ppm scale factor and 50 μ g bias. The gyro bias drift stability is 0.09 meru (0.0015 deg/hr) and acceleration sensitive drift stability is 0.29 meru/g (0.0045 deg/hr/g). Stability data is discussed in Paragraph 2.6.

All priority tests listed in Reference 8 were completed except for closed loop frequency response measurements and noise errors within the instrument's bandwidth.

Tests which demonstrated the multisensor parameter sensitivity to changes in float position, temperature, wheel power, excitation voltage and current are described in Paragraph 2.5.

In addition to parameter stability, a 72 hour one position stability test is discussed in Paragraph 2.7. Calculations of drift uncertainty results were made using data which includes trends. After the trends are removed, improvements of 0-40 percent in parameter stability are realized.

A warm-up characterization test was performed from only one level of temperature dormancy. The test results including instrument temperature are presented in Paragraph 2.8.

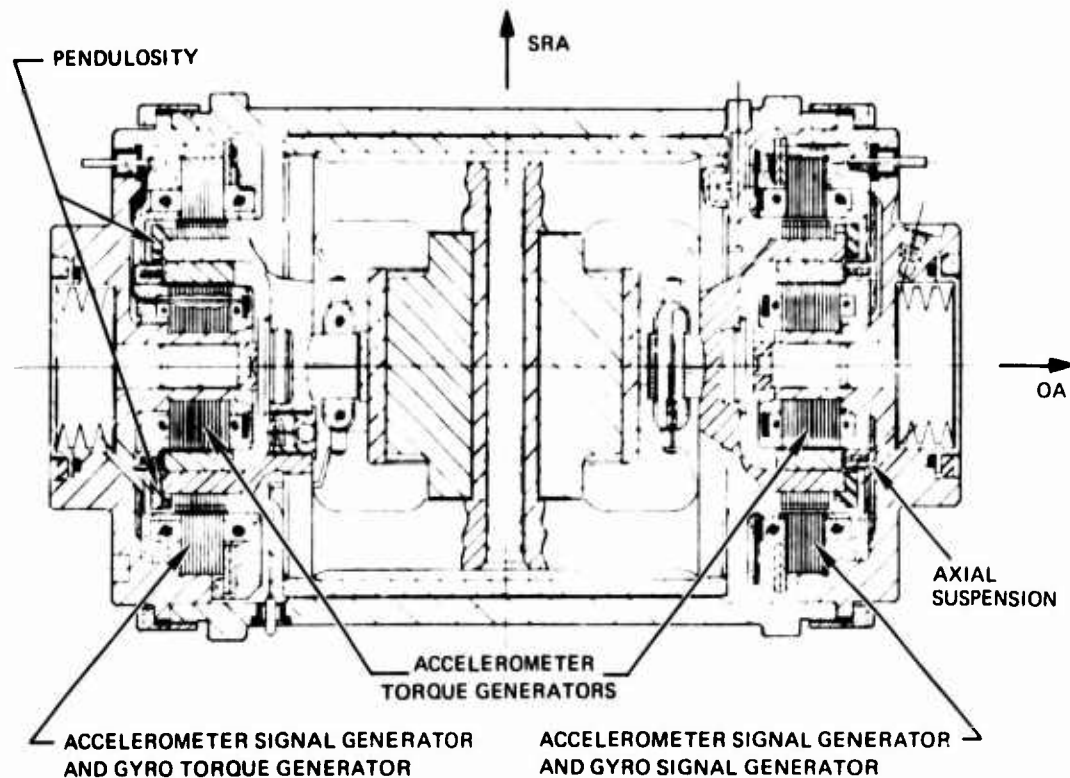
Multisensor cross-coupling tests have been conducted to evaluate the effects of misalignment since the accelerometer's input axis probably will not be on the reference axes or coincident with the gyro input axis. Also, the accelerometer outputs contain rate information (Paragraph 3.2 and 3.3). The data reduction algorithms are available, however, since some difficulty has been experienced in transferring the raw data to a new computer system, the results of this test are not available at this time.

Tests were conducted to determine the cause of the accelerometer's long settling time which was previously reported (October 1976) at Quarterly Review. The tests revealed that the readout active filters require up to 30 minutes for the output to reach its final value. The settle time is related to the initial value of the filter's input. During instrument tumbling, large rate torques cause the filter to saturate or nearly saturate. The filter's settling characteristic is attributed to capacitance dielectric which is somewhat analogous to magnetic disaccommodation. A mylar capacitor which replaced the original tantulum capacitor eliminated this problem. The instrument response with mylar filter capacitor is given in Paragraph 2.8.

2.2 INSTRUMENT DESCRIPTION

The feasibility multisensor is a single-degree-of-freedom floated gyroscope with pendulosity intentionally added along the gyro output axis.

The instrument closely resembles the schematic shown in Figure 1-1, and is depicted in cutaway form in Figure 2-1. Pertinent characteristics are tabulated in Table 2-1. The feasibility instrument was designed to minimize cost and to produce data in a short time frame; thus, the instrument is an Inertial Reference Integrating Gyroscope (18 IRIG Mod D) with modifications. As discussed in Chapter 4, optimized configurations will probably differ from the feasibility instrument. Pendulosity was added by reworking the balance rings. The tapered suspension was replaced by separate radial and axial suspensions. The gyro signal and torque generators were redesigned to yield accelerometer loop displacement signals (in addition to performing their normal functions) so that active control of the accelerometer rebalance could be implemented. End housings were altered so that separate leads (see Figure 2-2) for each winding are available to increase experimental flexibility. The float-case gap was tapered to reduce the rotational damping coefficients about the spin and output axes.



5/73 CD3395 REV A 11/76

Figure 2-1. Feasibility multisensor.

Figure 2-2 shows the multisensor mounted in the test fixture which was designed so that the instrument will be thermally symmetric from end to end in order to reduce accelerometer scale factor and bias instabilities.

2.3 BUILD INTEGRITY

After discovery of a broken pivot in the signal generator end, the instrument was refabricated and returned to test on 24 September 1976. The multisensor was wired and connected with passive suspensions to determine the acceptability of the rebuilt instrument. All measured parameters are within the specifications of a normal (18 series) gyro except flotation temperature is 10°F higher than specified (132°F) in Table 2-1. This flotation discrepancy resulted because the flotation rings were removed from the float while the instrument was filled with low viscosity fluid during a previous IR&D program. The measured output axis damping is reduced by a factor of 2 as a result of the increased operating temperature.



80009

Figure 2-2. Feasibility multisensor mounted in test fixture.

TABLE 2-1. BUILD INTEGRITY TEST PARAMETERS.

| | |
|---|---------------------------|
| Axial centering ratio | = 0.93 |
| Radial centering ratio | SS = 0.56 |
| | SI = 0.66 |
| | TS = 0.90 |
| | TI = 0.83 |
| Gyro SG-TG null coincidence | < 1.0 mr |
| OA damping (C_d) | = 1.14×10^5 dc s |
| Gyro SG sensitivity with $Q = 4$ at 6 mA/leg (I ori) | = 95.8 mv/mr |
| OA float stop angles | +15.3 mr, -12.1 mr |
| Wheel power (total) | = 9.11 watts |
| ASG electrical centers (nulls) were determined | |
| Float freedom ramp test indicated no problems | |
| Flotation along I axis | 142.6° F |
| Flotation along O axis | 144.8° F |

When the accelerometer's active suspension control loops were closed, the output signals were very noisy. The spin axis forcer (which sums torques about IA) signals exhibited noise level greater than the loop capability of 2.5 gravities. In particular, the forcers on the float TG end showed a greater rms noise level than the SG end. This observation verified that the gyro torque rebalance current interacts magnetically with the accelerometer's signal generator since both share the same electromagnetic circuit. Also, small signal generator noise propagates into large forcer noise because of the large gain required to achieve wide bandwidth with high damping about the transverse axes (see Section 3.6). To allow further testing of the multisensor, the accelerometer bandwidth (refer to Appendixes B, C, and D) was reduced from 22 to 0.8 Hz and a small transformer was added which couples the gyro torquer secondary and the accelerometer's signal generator to cancel the magnetic coupling which occurs within the instrument.

2.4 DATA PROCESSING

The multisensor data was processed on a digital computer. After the data is recorded on magnetic tape using the Data Acquisition System (DAS), it is mounted on the tape deck of the PDP8 computers. The tape is read by a program which converts files produced by the DAS into files which can be used by the PDP8.

The analog signal files are the input to another program where they are transformed. Each raw data point X is modified by the equation $Y = A X + B$. The normal values of the analog signals which have been suppressed by passing each accelerometer output through a Fluke differential voltmeter are reintroduced. Also, each raw data point is scaled. The scaling constant A (Sections 3.3 and 3.9) was determined by a calibration test for each accelerometer axis to minimize off-flotation-effects. The test consisted of producing a small gravity change to the accelerometer input axis and measuring the corresponding change in output force voltage on each end of the float. The constant is then calculated by the ratio of the two voltages for each axis. These constants reduce the errors between the two voltage outputs of an accelerometer axis because of mismatched electromagnetic windings and readout electronics. The value of B for a given axis is the suppressed voltage for that axis times A . The resulting transformed files were processed by the following options:

- (1) Statistics - mean, standard deviation, and coefficient of vibration.
- (2) Linear regression - drift analysis.
- (3) Plotting - graphical representation of data.
- (4) Average points - filters the data.
- (5) Combining files - Sum of force signals for each accelerometer.

Four mean values of force signals E_{SI} , E_{TI} , E_{SS} , and E_{TS} are obtained. To compute scale factor and bias for each accelerometer, mean values are processed from a two point test (2 from IA up and 2 from IA down). The values are an input to a program that computes SF and bias according to the following equations.

1 Accelerometers

$$I \text{ Axis SF} = \frac{1}{2 g \cos \theta} \left\{ \left[E_{SI}(\theta) + E_{TI}(\theta) \right] - \left[E_{SI}(\theta+\pi) + E_{TI}(\theta+\pi) \right] \right\}$$

$$I \text{ Axis Bias} = \frac{1}{2 SF_I} \left\{ \left[E_{SI}(\theta) + E_{TI}(\theta) \right] + \left[E_{SI}(\theta+\pi) + E_{TI}(\theta+\pi) \right] \right\}$$

where:

E_{SI} = transformed voltage SG end I axis

E_{TI} = transformed voltage TG end I axis

For the S accelerometers: Substitute $\theta = \theta - \pi/2$; and

E_{SS} = transformed voltage SG end S axis for E_{SI}

E_{TS} = transformed voltage TG end S axis for E_{TI}

Gyro bias and acceleration sensitive drifts are computed by:

$$\text{Bias Drift (BD)} = \frac{1}{2SF} (E_{\text{down}} + E_{\text{up}})$$

$$\text{Accelerometer Drift} = \frac{1}{2SF} (E_{\text{down}} - E_{\text{up}})$$

Where gyro SF is determined from an OA vertical, IA horizontal north to IA east test

$$SF = \frac{E_{\text{north}} - E_{\text{east}}}{738.9 \text{ meru}}$$

2.5 SENSITIVITY TESTS

Sensitivity testing was conducted to provide a basis for comparison with stability data and a better understanding of the feasibility instrument's behavior. These tests demonstrated the multisensor sensitivity to the following conditions:

- (1) Temperature - uniform and gradient (end to end).
- (2) Wheel power.
- (3) SG primary excitation.

- (4) Radial and axial position, and
- (5) Forces primary current.

Sensitivity test results are listed in Table 2-2. All test data is plotted in Figures 2-6 through 2-35.

The uniform temperature sensitivity was conducted by varying the case temperature controller $\pm 0.8^{\circ}\text{F}$. The end housing temperature monitors indicated the same temperature change occurred end to end, therefore, no gradient was introduced. The scale factor and bias measurements were made after the temperature had settled at least 1/2 hour. An interesting result of this test is that the S-axis SF sensitivity is 2.3 times greater than the I-axis. The S-axis bias is 1.8 times larger than I-axis and of opposite slope. The test was performed twice with similar results. The differences between axes are attributed to non-ideal temperature distribution and the voltage scaling factors. Further testing is required.

A thermal gradient test was performed. A disc type heater was cemented to the SG end housing to produce an end unbalance heater power. An increase in SG end temperature (0.072°F) caused the case temperature controller to respond with a decrease and a reduced temperature in the TG end -0.02°F . The new result is a nonlinear temperature gradient along the instrument's OA as shown in Figure 2-3. Note that the end mounted thermistors indicated a 1.5°F cooler than normal operating temperature than the center of the instrument. Because the OA thermal gradient is not linear, the sensitivities for this test, listed in Table 2-2, should be interpreted as approximate values only.

Wheel power sensitivity was determined by varying the excitation ± 5 percent from a normal of 9.1 watts. Sufficient time was allowed for temperature settling before scale factor and bias measurements were made. A 5 percent change in wheel power causes a 0.02°F change in instrument case temperature. The temperature controller responds to decreasing wheel power by increasing heater power. The S-axis scale factor sensitivity is 4.5 times larger than along the I-axis. The difference between axes is attributed to uncertainty in temperature distribution and/or in the voltage scaling factors.

The accelerometer scale factor sensitivities to SG primary excitation are small and nearly identical in both axes. The S-axis bias sensitivity is 20 times larger than the I-axis sensitivity. Similarly, the reaction torque attributed to the forcer primary is 20 times

TABLE 2-2. FEASIBILITY INSTRUMENT SENSITIVITY TEST RESULTS.

| | I-Axis Acceleration | | S-Axis Acceleration | | Gyro | |
|---------------------------------------|---------------------|----------------------------------|---------------------|-----------------------------------|-------------------|--------------------|
| | SF | Bias | SF | Bias | Bias Drift | Accel. Drift |
| Temperature (uniform) | 3100 ppm/°F | 530 $\mu\text{g}/^\circ\text{F}$ | 7120 ppm/°F | -950 $\mu\text{g}/^\circ\text{F}$ | -0.019 meru/°F | 0.72 meru/g/°F |
| Temperature (gradient) | 10" ppm/°F | 500 $\mu\text{g}/^\circ\text{F}$ | 10" ppm/°F | 1200 $\mu\text{g}/^\circ\text{F}$ | (DATA LOST) | |
| Wheel power | 850 ppm/watt | 380 $\mu\text{g}/\text{watt}$ | 3870 ppm/watt | -680 $\mu\text{g}/\text{watt}$ | -0.048 meru/watt | -0.3 meru/g/watt |
| SG primar exc. | -30 ppm/% | 71 $\mu\text{g}/\%$ | -32 ppm/% | -1460 $\mu\text{g}/\%$ | -0.15 meru/% | -0.0065 meru/g/% |
| Axial position | 8.7 ppm/lin. | 4.2 $\mu\text{g}/\text{lin.}$ | 6.5 ppm/lin. | 5.2 $\mu\text{g}/\text{lin.}$ | <0.001 meru/lin. | <0.001 meru/g/lin. |
| I-Axis radial position | 6.7 ppm/lin. | 250 $\mu\text{g}/\text{lin.}$ | 2.6 ppm/lin. | 3.6 $\mu\text{g}/\text{lin.}$ | 0.013 meru/lin. | <0.001 meru/g/lin. |
| S-Axis radial position | 5.0 ppm/lin. | 4.6 $\mu\text{g}/\text{lin.}$ | 26.5 ppm/lin. | -10.7 $\mu\text{g}/\text{lin.}$ | -0.0034 meru/lin. | <0.001 meru/g/lin. |
| Reaction torque due to forcer primary | — | 7000 μg | — | 1.65 $\times 10^4 \mu\text{g}$ | -1.92 meru | — |

larger in the S-axis than in the I-axis. These three observations are explained by misalignments between the zero force positions of the signal generator, the forcer primary zero force position, and the signal generator zero displacement signal position.

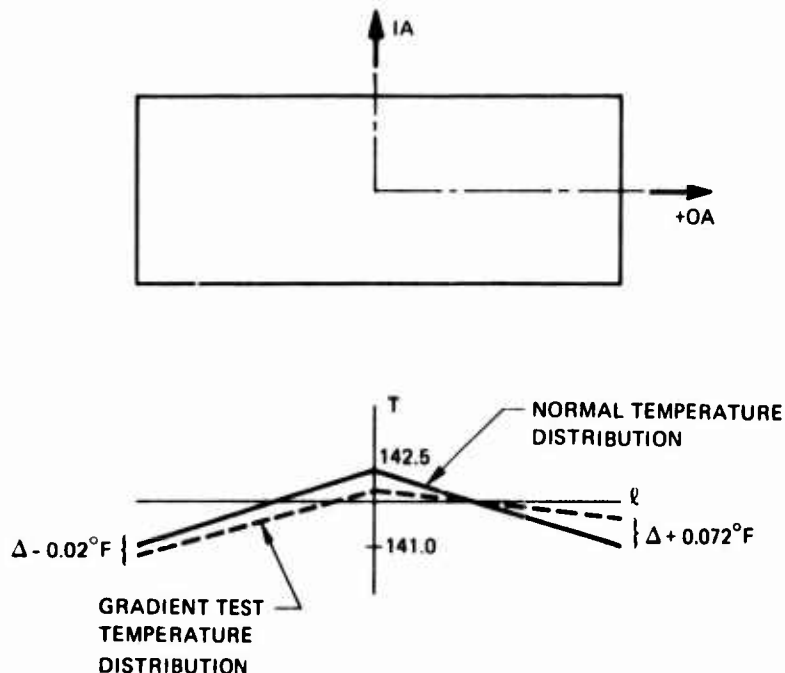


Figure 2-3. Multisensor normal and temperature gradient distribution.

In preliminary air bearing tests at the component level, the accelerometer signal generators were tuned with positive elastic restraint to balance the negative restraint of the constant magnitude square wave forcer primaries. Elastic restraint is defined as a position sensitive force. This technique's success is reflected in the I-axis bias sensitivity to I-axis radial position (250 $\mu\text{g}/\mu\text{in}$, not very good since this is near the restraint of forcer primary alone) and similarly for the S-axis (10 $\mu\text{g}/\text{min}$, an acceptable value) (Appendix D elaborates). To account for asymmetries between components and other sources of elastic restraint such as the axial suspension, the elastic restraint tuning should be done in the actual instrument as will be discussed shortly.

Return to the alignment of the various null conditions. Because of the integrator in the accelerometer loops, the float position with

respect to the case is determined when the output of the signal generator is null. With current transformers, this corresponds to equal currents on opposite magnetic cores. The signal generator is tuned as a passive suspension so that the zero force point which depends on the capacitors may differ from the equal current position. The sensitivity to signal generator excitation is proportional to the displacement between the two centers. If the centers do not coincide, changing the excitation causes the signal generator to exert a force. The controller then alters the forcer secondary current so that the equal current condition is met and the sum of forces exerted on the float is zero. Similarly, a displacement between the SG zero current position and the forcer primary null force point results in the reaction torque attributed to the forcer primary.

A further explanation of the situation and estimate of the degree of misalignment are offered in Figure 2-4 which models the forcer and SG at one end. The letters refer to the following:

- (1) Line A is the force displacement characteristics of the forcer primary.
- (2) Line B is the force-displacement characteristic of the signal generator.
- (3) Point C is the zero force point for the signal generator.
- (4) Point D is the zero force for the forcer primary.
- (5) Axis E is the equal current null position of the signal generator. Because of the integral control loop, steady-state operation will result on this axis.
- (6) Force F is the reaction of the forcer primary.
- (7) Force G is the reaction of the signal generator.
- (8) Force H is the force exerted by the forcer secondary so that the sum of forcer (H plus F) and signal generator forces (G) is zero (with no external forces operating).
- (9) Slope I is the elastic restraint of the forcer.
- (10) Slope J is the elastic restraint of the signal generator.

The situation in the actual instrument is complicated by the presence of two ends; however, the basic argument remains valid. For the forcer restraint of $1.6 \times 10^5 \mu\text{g}$ and measured elastic restraint (air bearing tests) of $2 \times 10^5 \text{ dyn-cm/cm}$, the displacement between

signal generator null and forcer null is 260 μ in. a figure certainly possible with manufacturing tolerances.

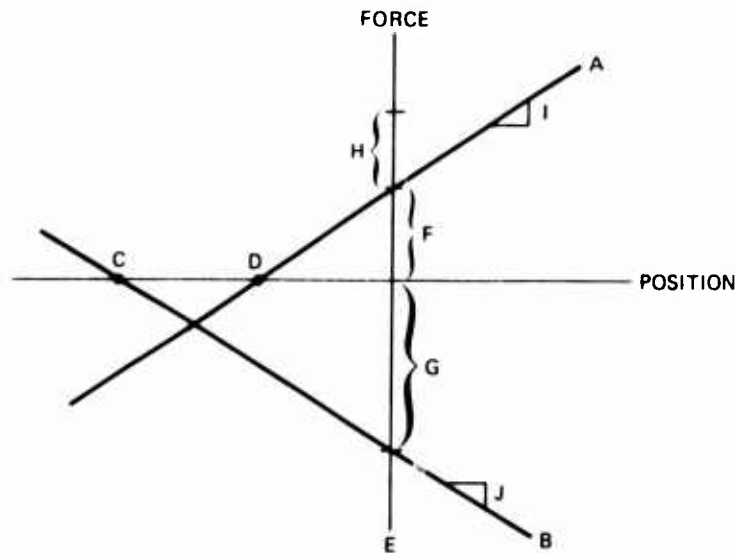


Figure 2-4. Performance of SG and forcer.
(see text for nomenclature)

In future testing, bias and elastic restraint tuning will be performed in the instrument. For the present device where the signal generator is connected in series parallel connection, elastic restraint can be adjusted by increasing the capacitance on both legs of a given axis simultaneously. Bias can be adjusted by either of the following techniques:

- (1) Change the SG null by adding a dummy signal;
- (2) Push-pull the SG capacitors; and/or
- (3) Add shunt resistors parallel to the legs of the forcer primary.

Since future designs will arrange the SG legs in bridge circuits, option 2 can be implemented by adding shunting capacitors parallel to the inductances.

The instrument's float position sensitivity was determined by dummy directing the active suspension loops along each of the S-, I-, O-axes. Sufficient time was allowed for transients to settle before

taking data. Axial and cross-axis displacement scale factor sensitivities are less than 10 ppm/min. I-axis and S-axis scale factor as a function of position along their respective axes display a distinct nonlinear characteristic particularly with I-axis position as shown in Figure 2-28. The test was repeated with similar results; however, more data points will be required to fully characterize the instrument's behavior. The nonlinearity in scale factor could be caused by non-linearity in the force position relationships of magnetic components.

2.6 STABILITY TESTS

The multisensor was tested for a period of 100 hours concentrating on the accelerometer scale factor and bias stability. The instrument was positioned OA horizontal east, parallel to the table, with IA up and down perpendicular to the earth's axis to minimize $H_W \omega_{OA}$ coupling (see Figure 2-5 and Paragraph 3.2). At each position, sufficient time was allowed for the forcer signals to settle before accumulating data. Ten-minute segments of one second sampled data is recorded on a data acquisition system magnetic tap for computer analysis. Additional measurements recorded during the stability tests monitored the following:

- (1) Instrument end housing and case temperature;
- (2) Changes in wheel power;
- (3) Axial force, and
- (4) Primary excitation.

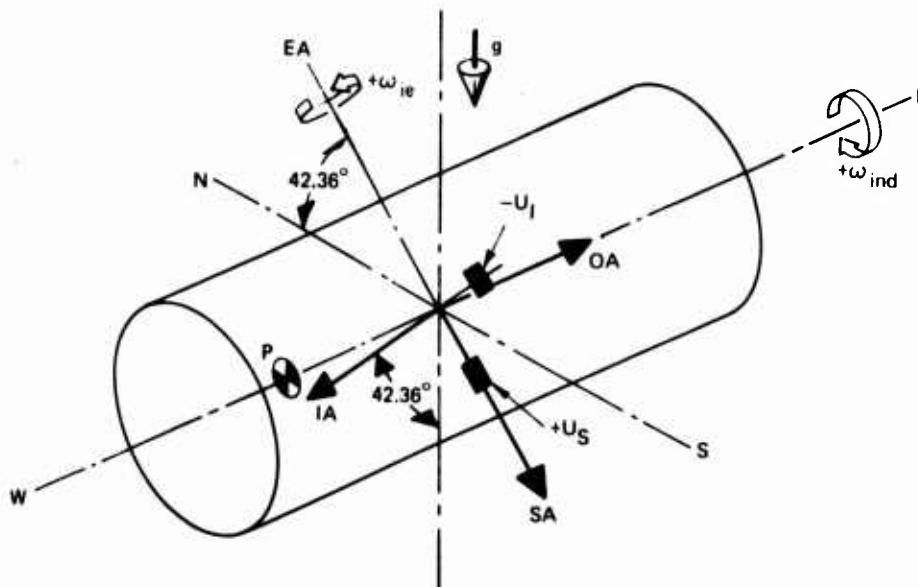


Figure 2-5. Multisensor position for scale factor and bias calibration tests.

The stability test results and performance objectives are listed in Table 2-3. All data is plotted as shown in Figures 2-36 through 2-44. These results indicate that excellent gyro performance has been obtained. The bias drift standard deviation exceeds the goal (0.015 deg/hr) by at least a factor of ten (0.00135 deg/hr). This performance is attributed to the independent active control of the radial and axial suspensions despite the large OA pendulosity (by gyro standards).

The accelerometer performance data is within the goals except for the marginal SF (62.3 ppm) uncertainty of the S-axis. Wheel power and SG primary excitation stability measurements do not contribute significantly to the accelerometer uncertainties. Wheel power stability is <0.002 watts contributing a maximum uncertainty of 8 ppm scale factor based on independent sensitivity measurements listed in Table 2-2. The SG primary excitation stability was measured at 0.045 percent but due to equipment difficulties at the time the source was not monitored, during the stability test. The contribution of this source to scale factor uncertainty is 1.5 ppm. The S-axis has a major bias sensitivity (65 μ g/0.045 percent) to primary excitation while the I-axis is 20 times smaller (3.2 μ g/0.045 percent). The bias standard deviations are nearly the same for both axes during stability testing; therefore, it is reasonable to assume then that this excitation did not change significantly during the test.

Multisensor temperature variation is a major source of scale factor instability according to analysis and sensitivity measurements, (see Paragraphs 2.5 and 3.4). Based on correlation of thermal measurements with accelerometer data, temperature was the major contributor to the stability test uncertainties. A careful examination of test data plotted in Figures 2-36, 2-37 and 2-42 shows a definite agreement in scale factor and temperature characteristics. In addition, the -0.009^oF temperature drift will produce approximately 10 ppm drift in scale factor. Also, scale factor variations about the trend line have relative magnitudes that agree well with temperature oscillations.

The temperature plot of Figure 2-42 was produced from strip chart recordings with the instrument IA-SA positioned down. This plot is also representative of the other three thermistor characteristics which are not presented. Instrument case temperature is shown plotted in Figure 2-43. Despite some difficulty with a noisy Sanborn strip chart recording, particularly during the first half of the test, the

TABLE 2-3. MULTISENSOR STABILITY GOALS AND TEST RESULTS (100 HOURS).

| Accelerometer | Mean | Trend | 1 σ about Trend | Goals 1 σ |
|--------------------------|---|------------------|------------------------|-------------------------|
| I-Axis Scale Factor | 8,159,544.0 (nano V/cm/s ²) | -1.9 ppm/hr | 47.0 ppm | 50 ppm |
| S-Axis Scale Factor | 8,327,450.1 (nano V/cm/s ²) | -1.0 ppm/hr | 62.3 ppm | |
| I-Axis Bias | 961.5 μ g | -1.0 μ g/hr | 46.3 μ g | 100 μ g |
| S-Axis Bias | -20,730.0 μ g | -0.5 μ g/hr | 44.3 μ g | |
| Gyro | | | | |
| Scale-Factor Calibration | 0.45 meru/mV | | | |
| Bias Drift | -12.31 meru | 0.0006 meru/hr | 0.09 meru | <0.015 ⁰ /hr |
| Acceleration Drift* | 38.62 meru/g | 0.0014 meru/g/hr | 0.29 meru/g | 1 meru |

The acceleration sensitive drift coefficients were measured separately.

* Acceleration drift = $AD_{SRA} - AD_{IA}$

where: $AD_{SRA} = 115.9$ meru/g (unbalance along IA)

$AD_{IA} = 70.5$ meru/g (unbalance along SA)

case temperature oscillations agree with the end housing measurements from 72 hours to 100 hours of the test. The case temperature positive trend is due to the temperature controller reaction to a decreasing trend in ambient temperature as indicated by base and end housing measurements.

2.7 ONE-POSITION STABILITY TEST

The multisensor was operated with output axis horizontal and east with the input axis up and perpendicular to earth axis (42 degrees from vertical) for 72 consecutive hours. A commercial tilt meter mounted on the test stand measured tilt angles in the north-south and east-west planes. The IA-SA plane lies in the north-south plane.

Data was recorded on the data acquisition system. The four radial forcers, the gyro torquer, four case thermistors, wheel power and the platform tilt were monitored. Sampled at ten second intervals and averaged over two minutes, the data versus time is plotted with statistical information in Figures 2-45 through 2-51. Since the four thermistors were nearly identical, only one temperature plot is included.

Power spectral densities are plotted in Figures 2-52 through 2-54. Aliasing effects were assumed small for the following reasons:

- (1) Data averaging acted as a low pass filter;
- (2) The accelerometer channels were filtered at 0.02 Hz;
- (3) Analog strip chart recordings did not reveal rising spectral characteristics beyond the Nyquist frequency.

Leakage (the sampling of a nonintegral number of cycles) has affected the spectral plots significantly. The tilt versus time plots clearly demonstrate spectral peaks which leakage spreads as a $1/f^2$.

The accelerometer standard deviations about the trend are 16.5 ppm for the I-axis and 26.3 ppm for the S-axis, figures which are two and three times better than the scale factor and bias measurements of the two position tests described in Paragraph 2.6. The S-axis accelerometer drifted -33 ppm during the 72 hours while the I-axis drifted -169 ppm. The drift of the two axes is similar if the step at 55 hours in the I-axis data is omitted. This shift could be caused by a capacitor shift since this axis has a large position sensitivity (250 $\mu\text{g}/\mu\text{in}$). Appendix D describes this phenomenon more completely. With the sensitivities

calculated for average temperature changes, the trend of $0.0023^{\circ}\text{F/hr}$ could account for -13.8 and -8 ppm in the S- and I-axes respectively.

Both accelerometer channels exhibit low frequency oscillation (less than two in the 72 hours) which leak to form the accelerometer spectra, $1/f^2$ slope at low frequencies. The temperature spectrum between 10^{-4} Hz and 4×10^{-3} Hz is approximately white noise of amplitude $6 \times 10^{-4} \text{ }^{\circ}\text{F}^2/\text{Hz}$. Multiplying the temperature spectrum by the I-axis average temperature sensitivity and using 5.9 volts as one gravity, one obtains an accelerometer spectrum of $2 \times 10^{-7} \text{ volt}^2/\text{Hz}$ which is the value of the I-accelerometer spectrum between 2×10^{-3} and 4×10^{-3} Hz. Performing a similar calculation on the S-axis results in $2 \times 10^{-6} \text{ volt}^2/\text{Hz}$, a value which is an order of magnitude less than the horizontal portion of the spectrum.

The wheel-power spectrum and the accelerometer sensitivities also contribute to the accelerometer errors. Fitting the wheel spectrum with white noise of $0.0015 \text{ watt}^2/\text{Hz}$, accelerometer spectra attributed to wheel-power variation are $6 \times 10^{-7} \text{ volt}^2/\text{Hz}$ for the S-accelerometer and $4 \times 10^{-8} \text{ volt}^2/\text{Hz}$ (see Figure 2-58). Both figures are an order of magnitude less than the plotted spectra. Consideration of this sensitivity is not entirely valid since wheel-power shifts affect temperature which has been considered separately. However, gyro testing has revealed coupling between flex leads and motor windings which do not depend on temperature so that the wheel-power correlation is included. Although the precise cause of the S-accelerometer spectrum between 10^{-5} Hz and 4×10^{-3} is unclear, the following comments are offered:

- (1) The spin axis contains information about case rates about the output axis.
- (2) The coupling of the accelerometer signal generator and the gyro is probably not the source. With white torque noise, the erroneous signal in the accelerometer signal generator would also be white noise because of the inductive coupling. From Appendix D, the torque rebalance noise at low frequencies would rise proportional to frequency squared which disagrees with the plotted spectrum.
- (3) Because of uncertainties in measuring sensitivities and temperature profiles, estimated sensitivities could be in error by a factor of two. An increase in sensitivity of scale factor to temperature level would explain the flat portion of the S curve.

The time data and spectrum for tilt indicate that tilt has only a small effect on stability data. Figures 2-55 and 2-56 show an rms tilt of 2.7×10^{-6} rads at one cycle per day which represents an accelerometer error of only 2 ppm when the axes are 45° to the vertical.

To summarize the accelerometer data, temperature stability impacts accelerometer stability greatly although other factors are present. The sensitivities to radial positions and the drift data and low frequency spectra strongly indicate another mechanism such as capacitor shift. Further study is recommended.

The gyro torque spectrum, Figure 2-54, approximately agrees with data compiled from conventional 18 IRIG and TGG. The cited references attribute the noise to internal disturbances such as temperature gradients across the float, turbulence in the air bearing, and signal generator noise and to environmental input. As indicated in the temperature spectrum, several areas of the temperature spectrum closely match those of the gyro; however attempts to correlate the two through the gyro scale factor sensitivity to average temperature result in gyro torque spectra of 3×10^{-4} meru²/Hz compared to the plotted spectra of 0.5 meru²/Hz. Temperature gradient along a radial axis, a principle driver of gyro error (Reference 7), was not monitored.

2.8 REACTION/WARM-UP CHARACTERISTIC

The purpose of this test was to demonstrate:

- (1) The thermal time constant of the instrument, and
- (2) Pull-in characteristics.

The reaction time of the multisensor was tested by removing the instrument heater power, decreasing the operating temperature 1.5°F . The temperature controller causes a 2.0°F overshoot during warm-up as shown in Figure 2-59. The test was performed with the input axis vertical and the spin axis horizontal. A decrease in measurement resolution was required to maintain on-scale recordings of instrument response. Because of reduced resolution capability, baseline measurements were conducted for comparison purposes prior to and following the transient test. The multisensor outputs were stable within five minutes after the temperature settled. I-axis forcer output plots (gravity sensitive) are shown in Figures 2-60 and 2-61, with the resultant summed (note cancellation by summation) outputs in Figure 2-62. The S-axis (insensitive to gravity) outputs are plotted in Figures 2-63, 2-64 and 2-65. Multisensor temperature presented in

Figure 2-59 is monitored by one of the four thermistors mounted on the end housings. The other thermistor responses are the same.

The gyro response from this test is not presented here, because of large gyro output voltage due to the vertical component of earth rate (673.8 meru) about the gyro input axis and the DAS automatic ranging limited resolution capability of ± 1.0 millivolt (0.5 meru). Voltage suppression was not used on the gyro output prior to data acquisition. Based on data from a trial test (gyro IA perpendicular to EA), the gyro output is stable within five minutes after the temperature has settled. The gyro response characteristic during warm-up from this test is plotted in Figure 2-66.

The multisensor's reaction to axial float motion was measured as the float returned to its center position from a 120 microinch TG displacement during sensitivity testing. The SG end S-axis force output and axial suspension current did not record properly on the DAS during this test. Strip chart recording of the S-axis accelerometer shows similar results (not shown) as the I-axis outputs plotted in Figures 2-67 and 2-68. Strip chart recordings indicate a 50 minute axial suspension settling time. The accelerometers and gyro are stable 35 minutes after the suspension is turned on. The gyro response is plotted in Figure 2-69.

Temperature measurements made on the SG and TG end housings are shown in Figures 2-70 and 2-71. Since the float was initially in the TG end, the active suspension applied pull-in current to the SG end winding causing a 0.075°F increase in end temperature. The temperature controller responded by a decrease in power, cooling the Tg end by 0.045°F . Approximately 16 or 17 minutes was required for the temperature to stabilize after turn-on. The accelerometer's long settling characteristic is caused by large reaction forces due to the axial suspension's stator/rotor relative cocking and/or uncovering. The axial suspension's large reaction forces were discovered during a previous multisensor IR&D program.

Section 4 introduces design modification which will speed pull-in time considerably.

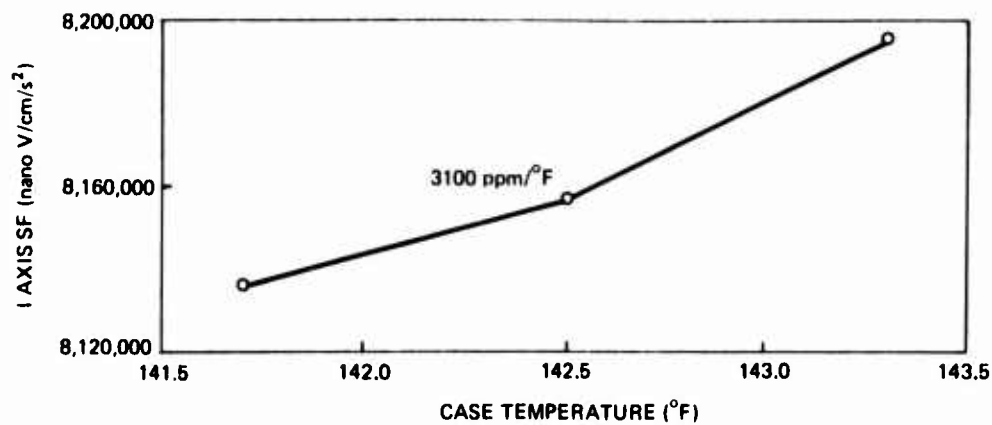


Figure 2-6. I-Axis acceleration scale factor temperature sensitivity (uniform temperature change).

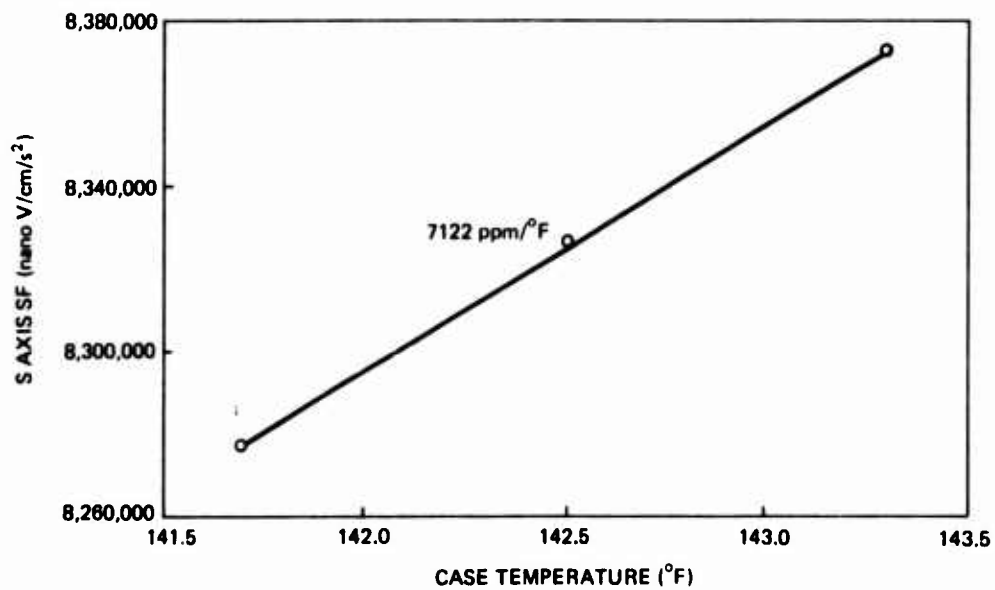


Figure 2-7. S-Axis acceleration scale factor temperature sensitivity (uniform temperature change).

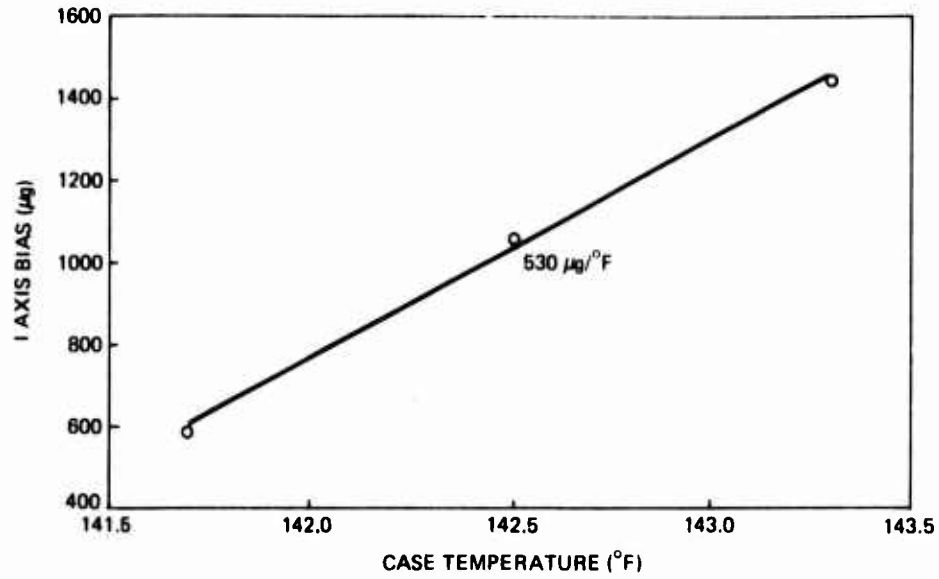


Figure 2-8. I-Axis acceleration bias temperature sensitivity (uniform temperature change).

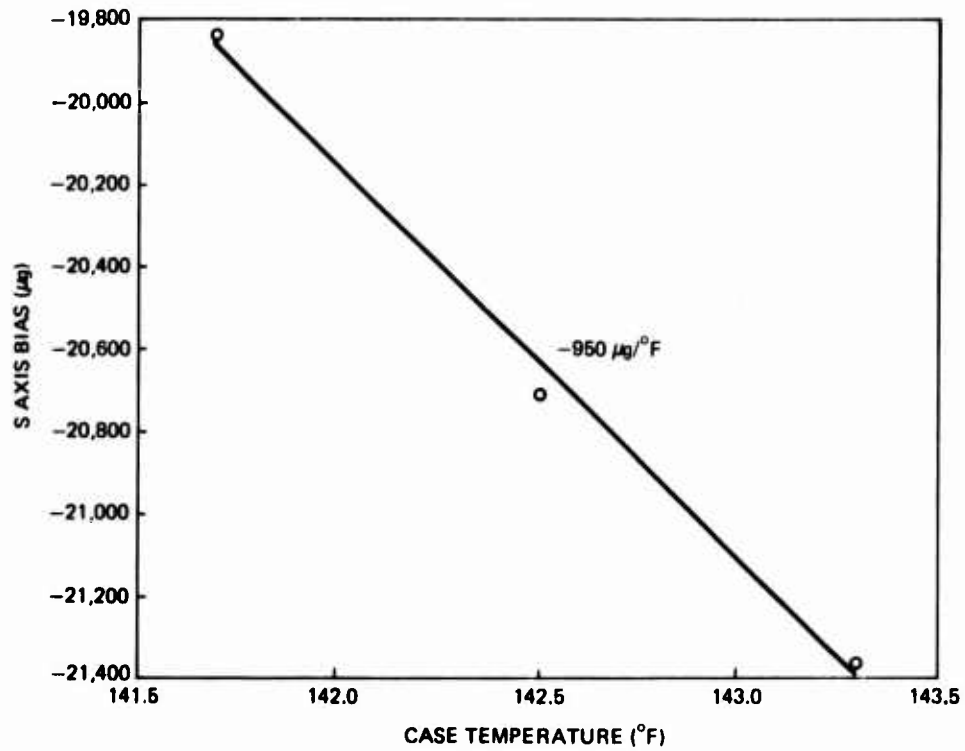


Figure 2-9. S-Axis acceleration bias temperature sensitivity (uniform temperature change).

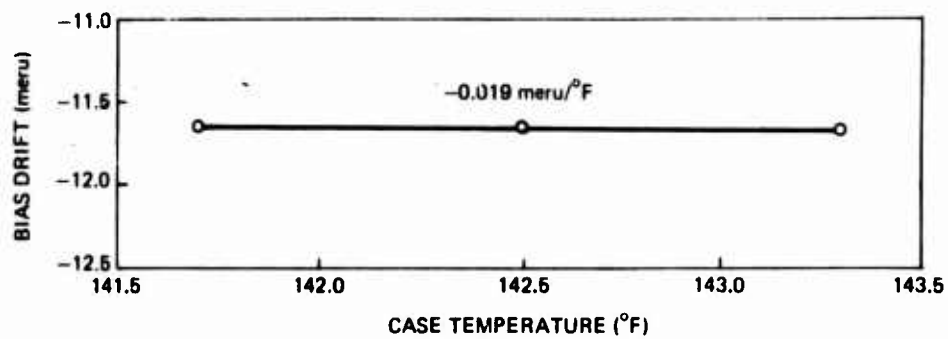


Figure 2-10. Gyro bias drift temperature sensitivity (uniform temperature change).

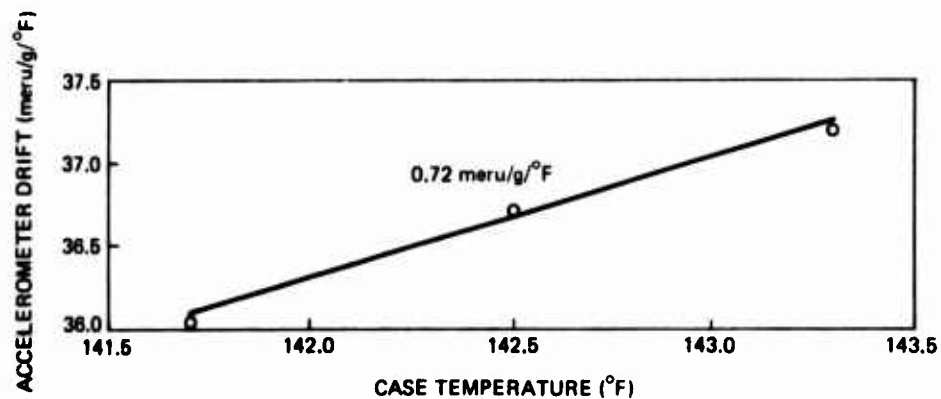


Figure 2-11. Gyro acceleration drift temperature sensitivity (uniform temperature change).

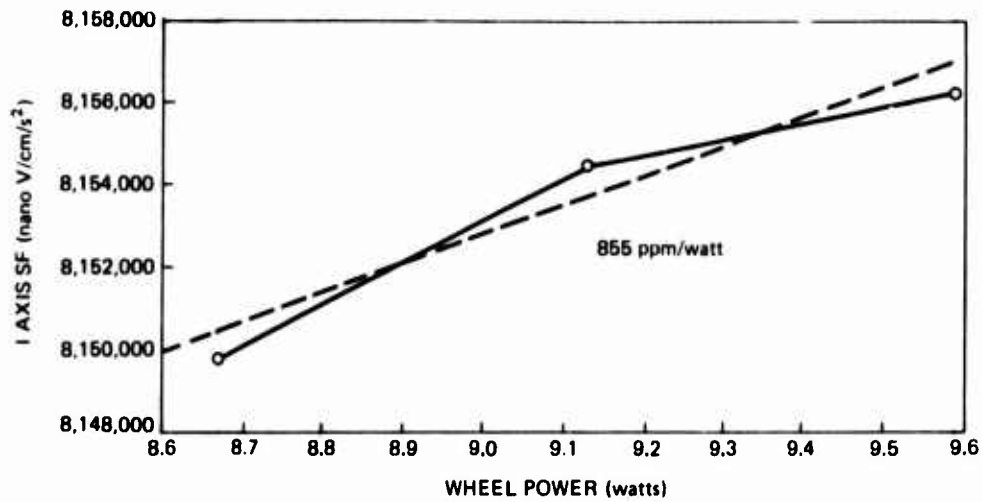


Figure 2-12. I-Axis acceleration scale factor
wheel power sensitivity (± 5 percent).

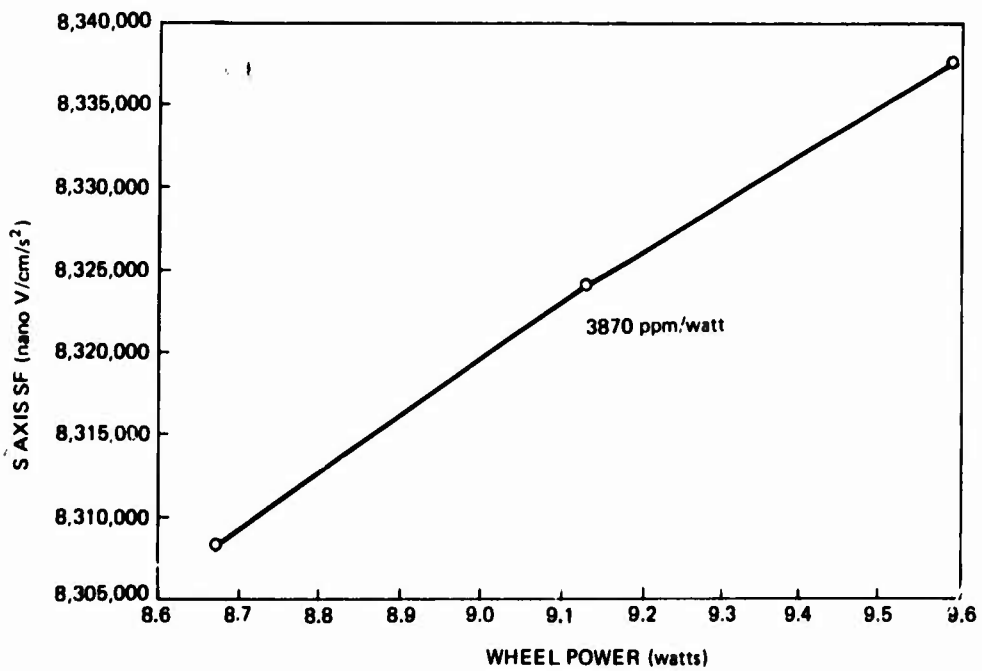


Figure 2-13. S-Axis acceleration scale factor
wheel power sensitivity (± 5 percent).

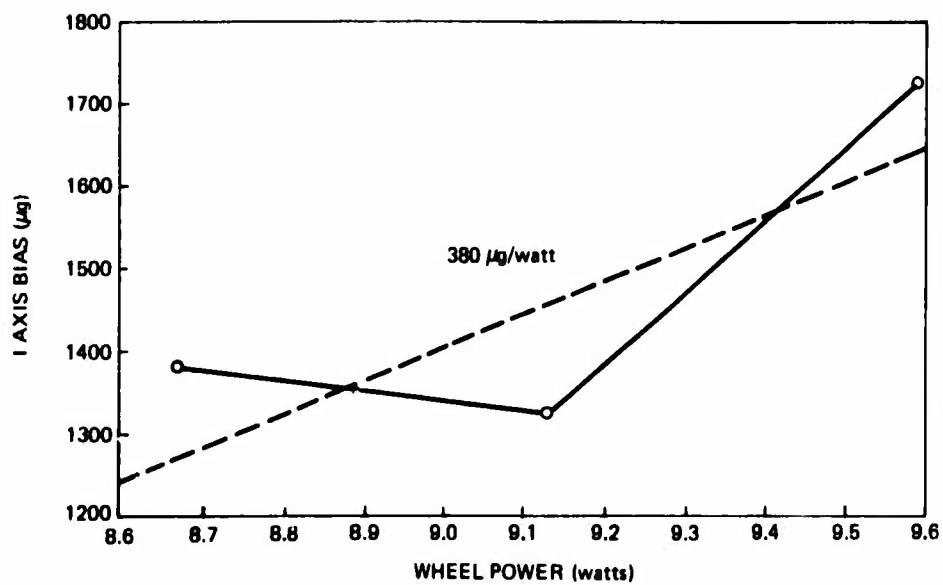


Figure 2-14. I-Axis acceleration bias wheel power sensitivity.

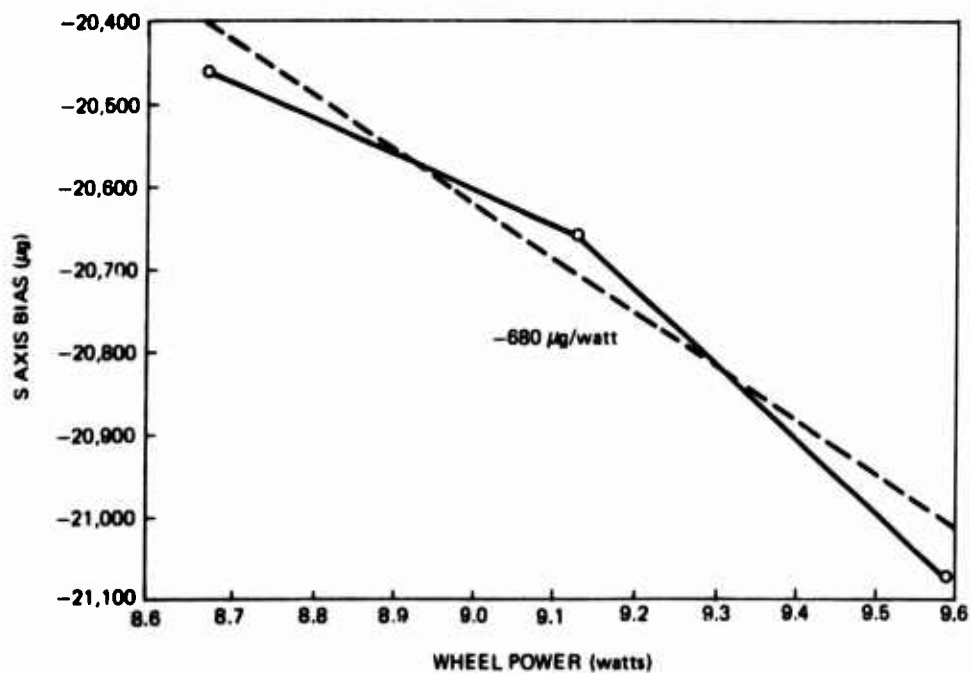


Figure 2-15. S-Axis acceleration bias wheel power sensitivity.

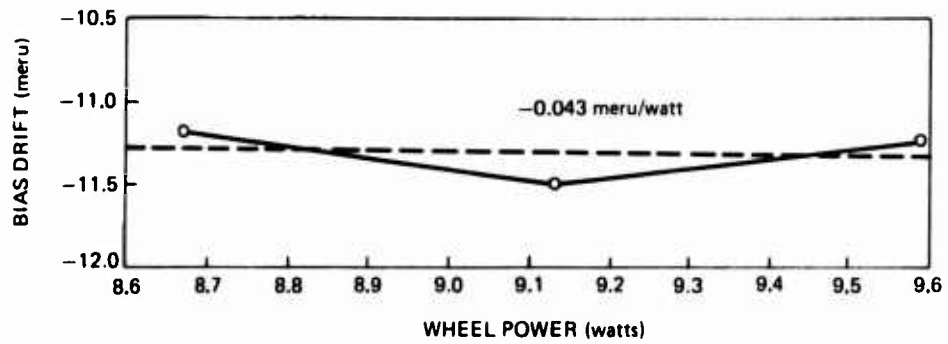


Figure 2-16. Gyro bias drift wheel power sensitivity.

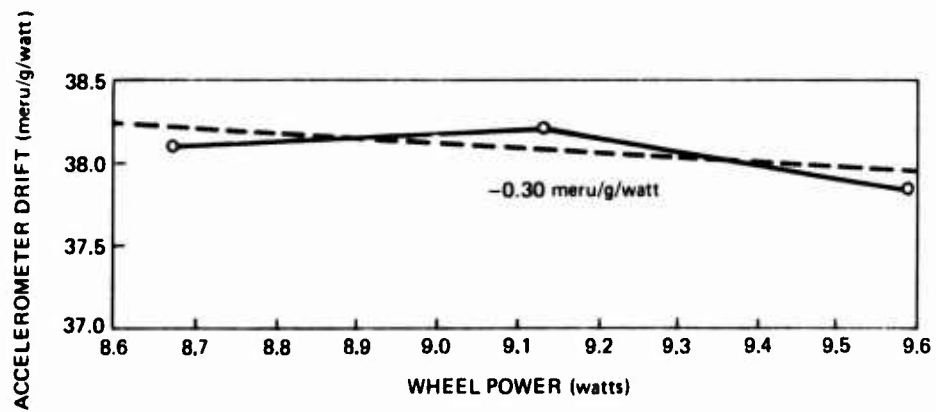


Figure 2-17. Gyro acceleration drift wheel power sensitivity.

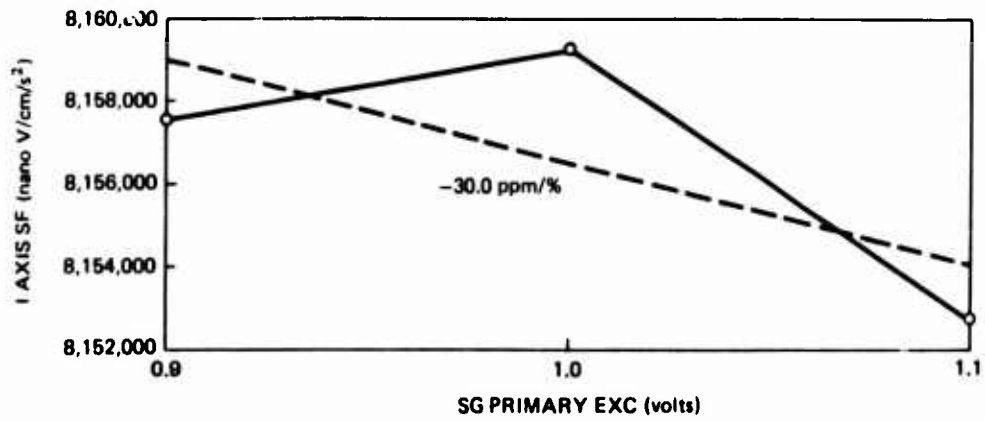


Figure 2-18. I-Axis acceleration scale factor sensitivity to SG primary excitation (9.6 kHz).

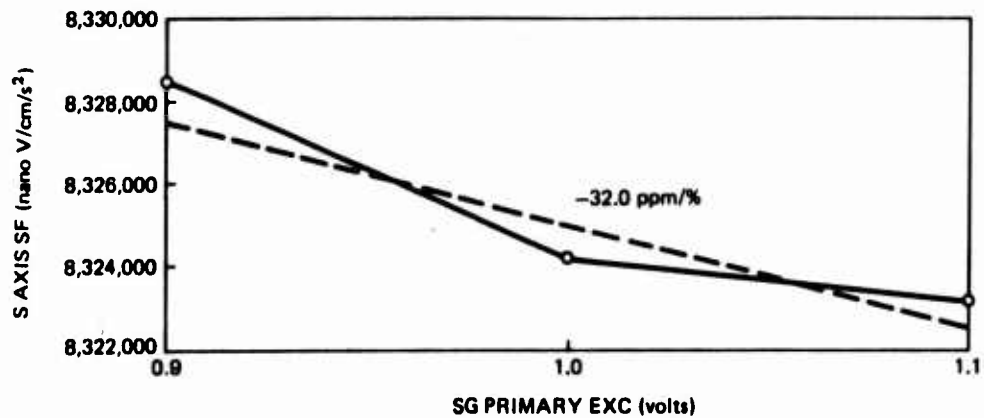


Figure 2-19. S-Axis acceleration scale factor sensitivity to SG primary excitation (9.6 kHz).

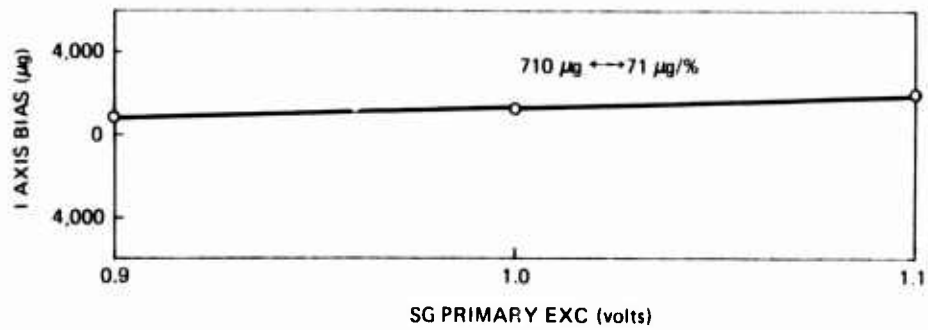


Figure 2-20. I-Axis acceleration bias sensitivity to SG primary excitation (9.6 kHz).

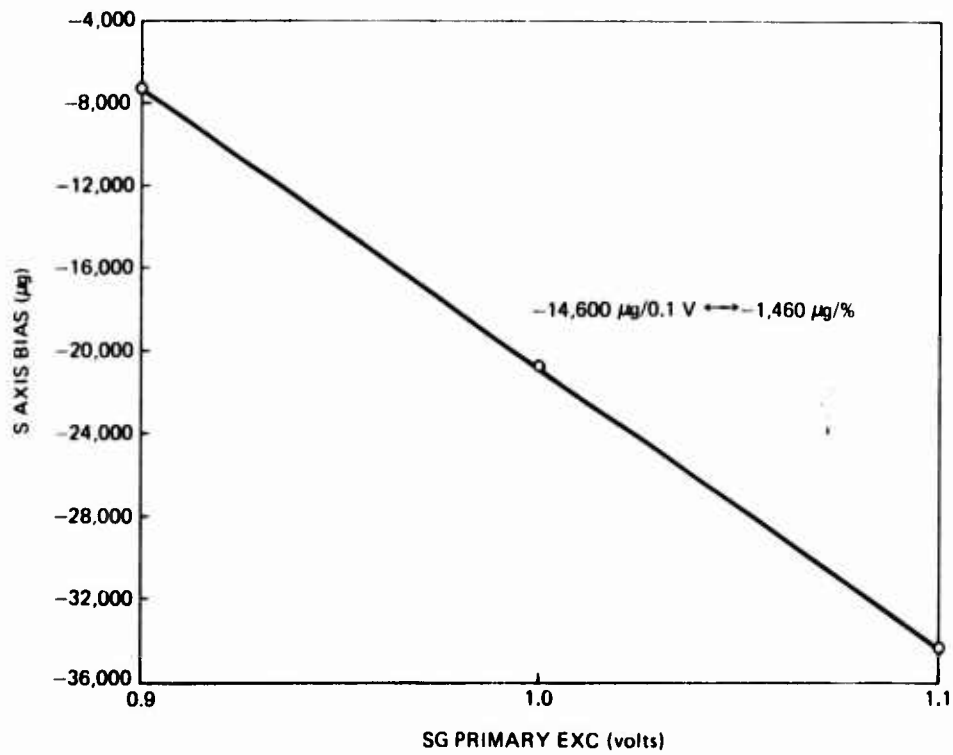


Figure 2-21. S-Axis acceleration bias sensitivity to SG primary excitation (9.6 kHz).

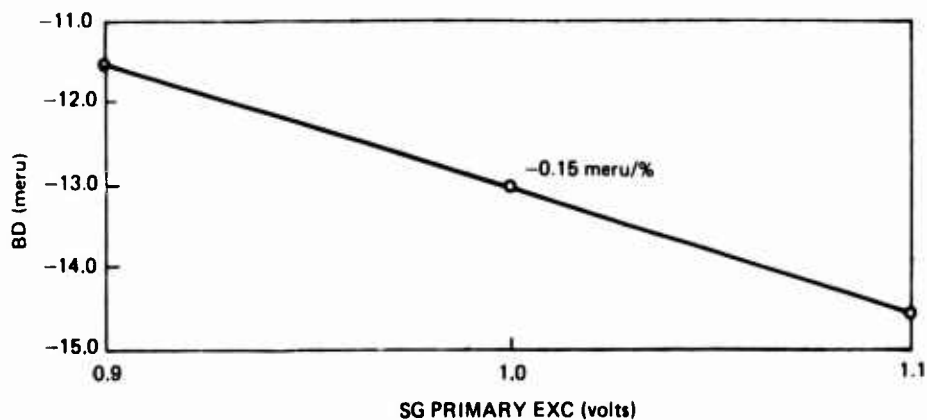


Figure 2-22. Gyro bias sensitivity to SG primary excitation (9.6 kHz).

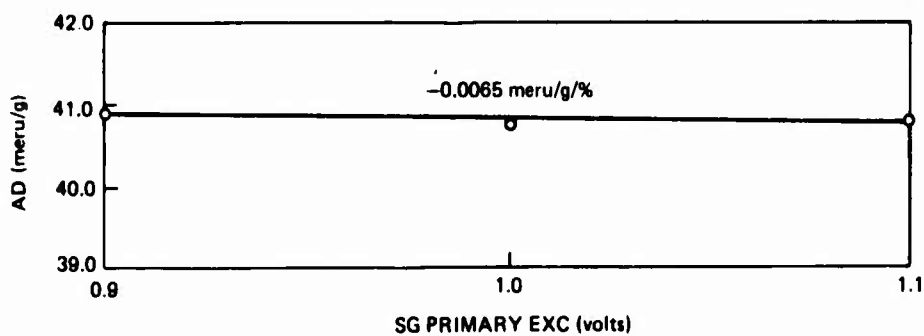


Figure 2-23. Gyro acceleration drift sensitivity to SG primary excitation (9.6 kHz).

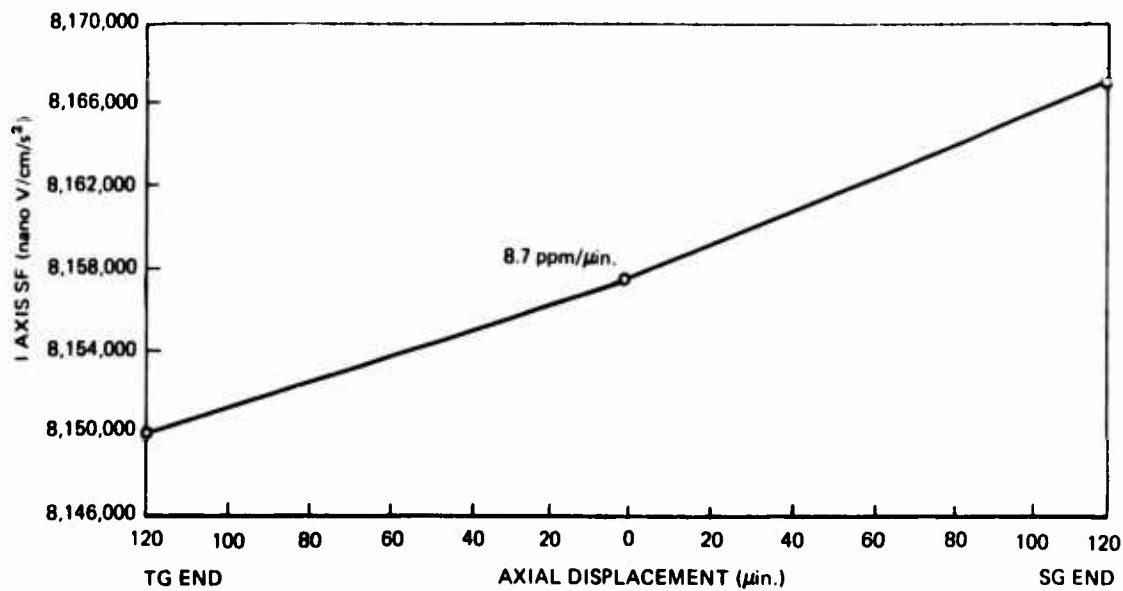


Figure 2-24. I-Axis scale factor sensitivity to axial position.

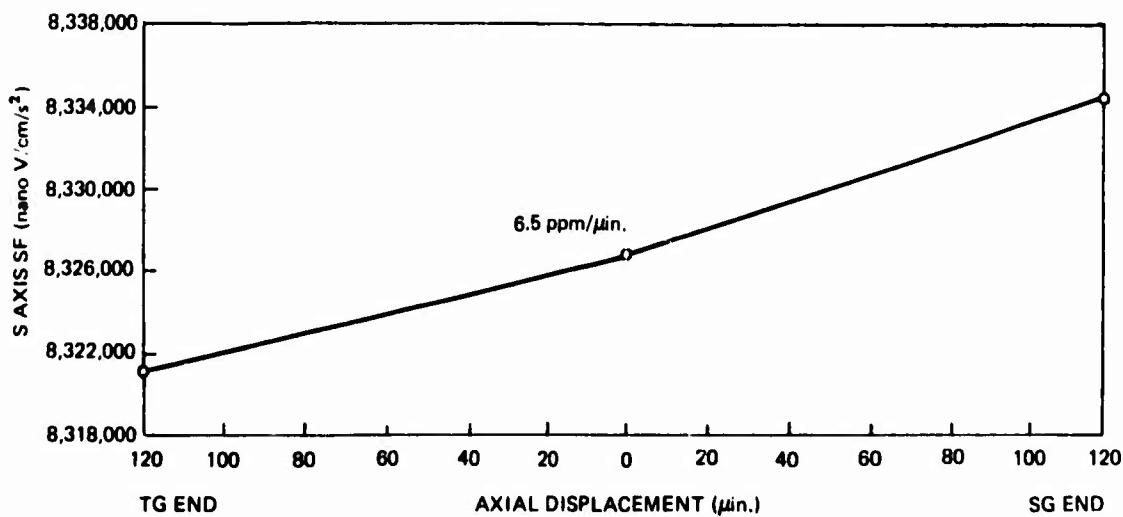


Figure 2-25. S-Axis scale factor sensitivity to axial position.

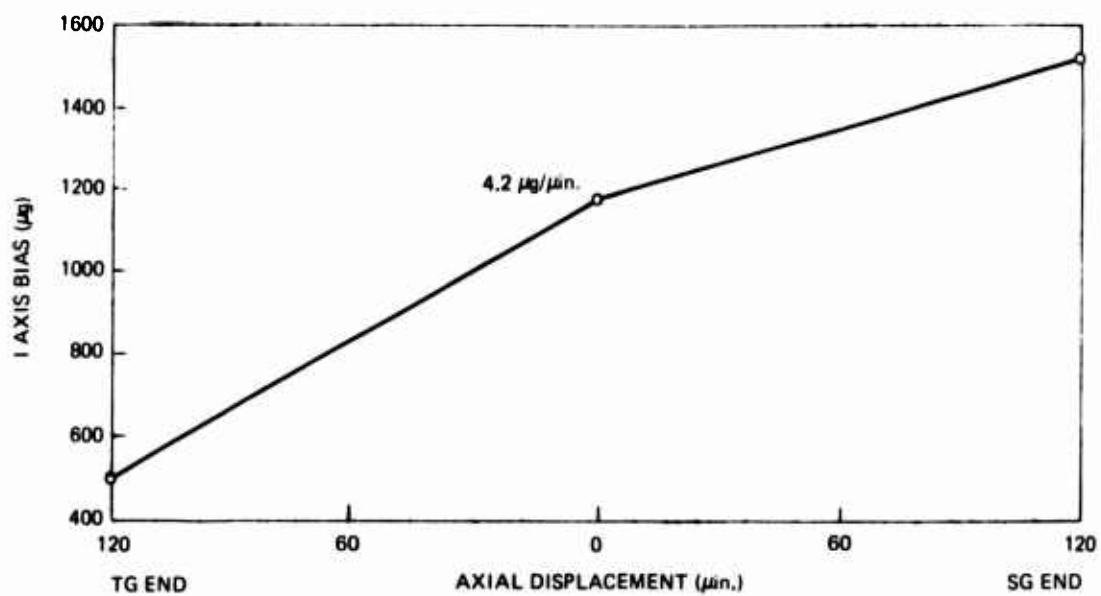


Figure 2-26. I-Axis acceleration bias sensitivity to axial position.

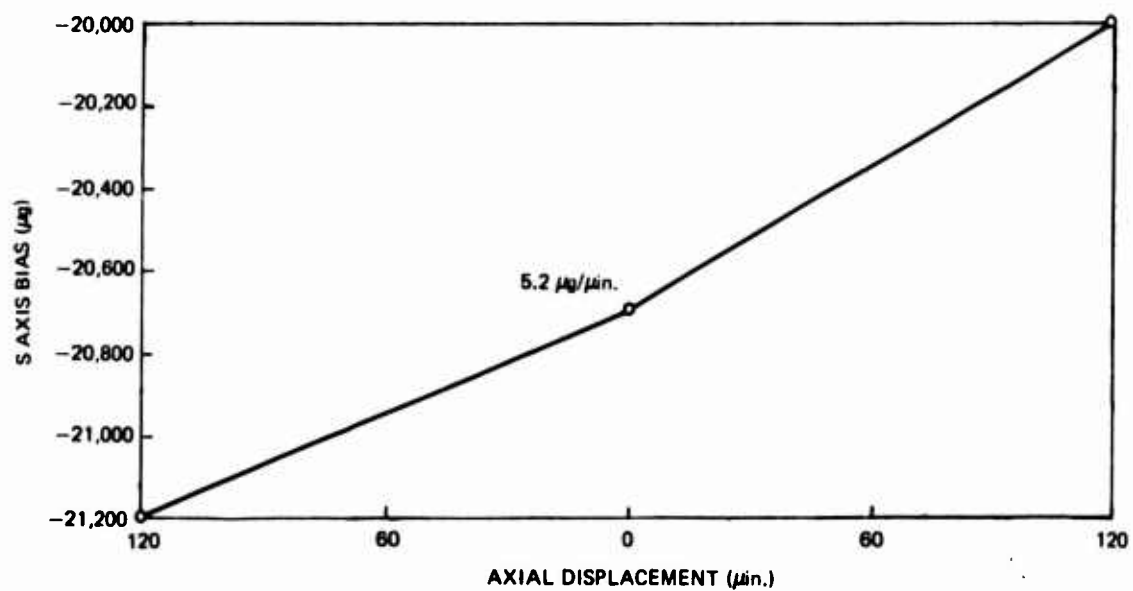


Figure 2-27. S-Axis acceleration bias sensitivity to axial position.

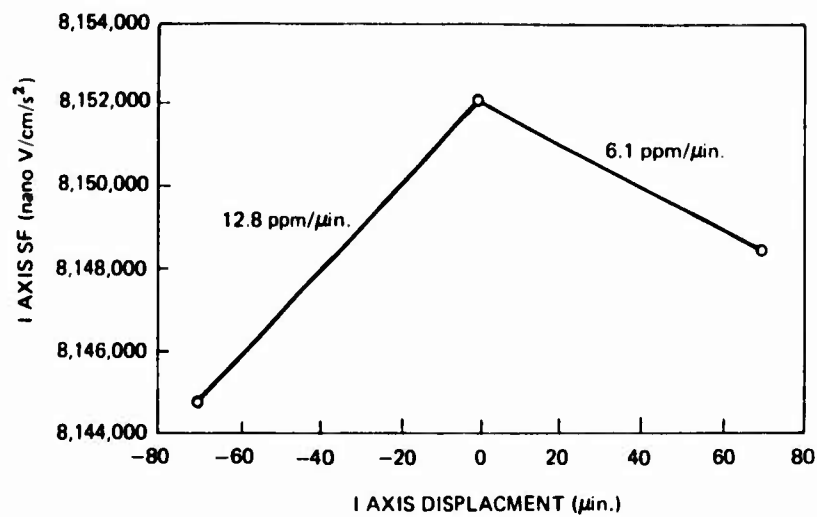


Figure 2-28. I-Axis acceleration scale factor sensitivity to I-Axis displacement.

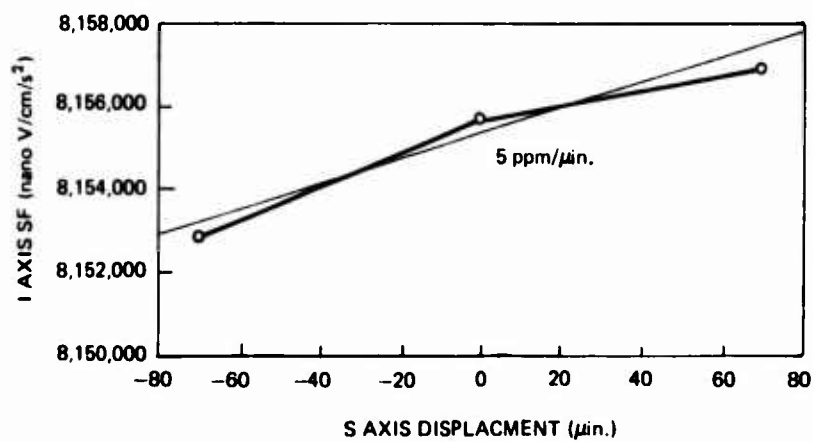


Figure 2-29. I-Axis scale factor sensitivity to S-Axis displacement.

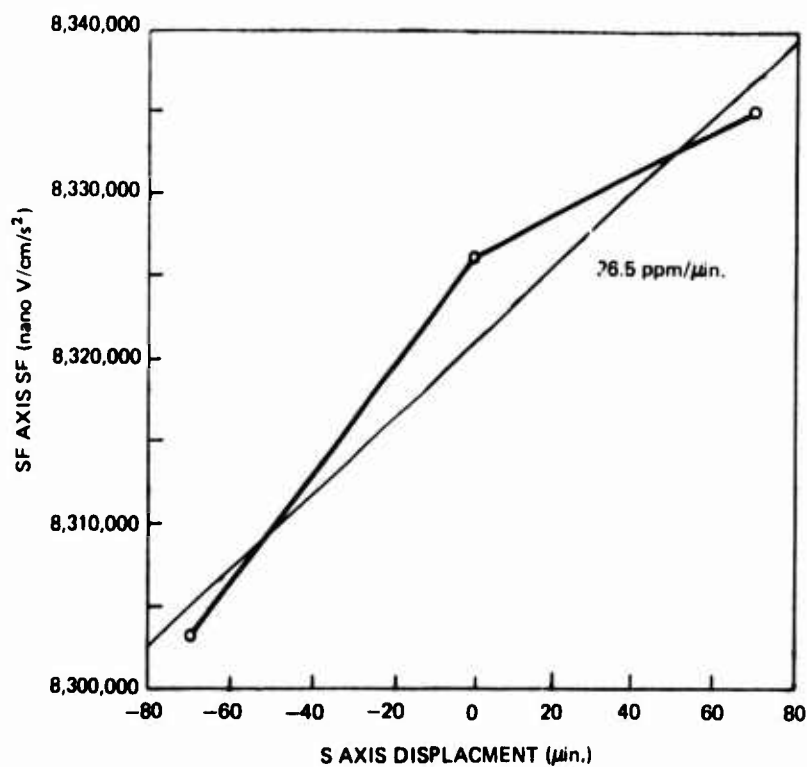


Figure 2-30. S-Axis acceleration scale factor sensitivity to S-Axis displacement.

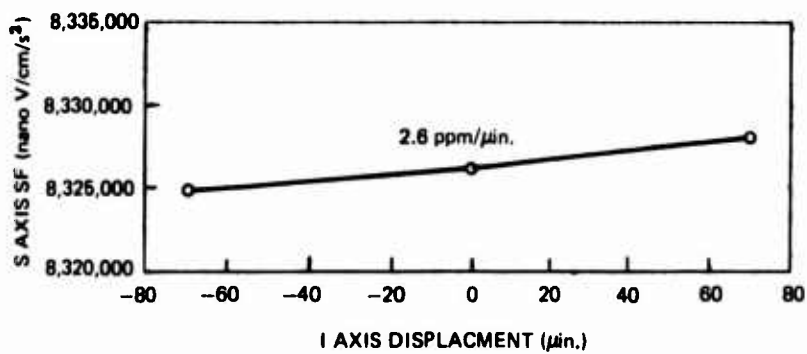


Figure 2-31. S-Axis scale factor sensitivity to I-Axis displacement.

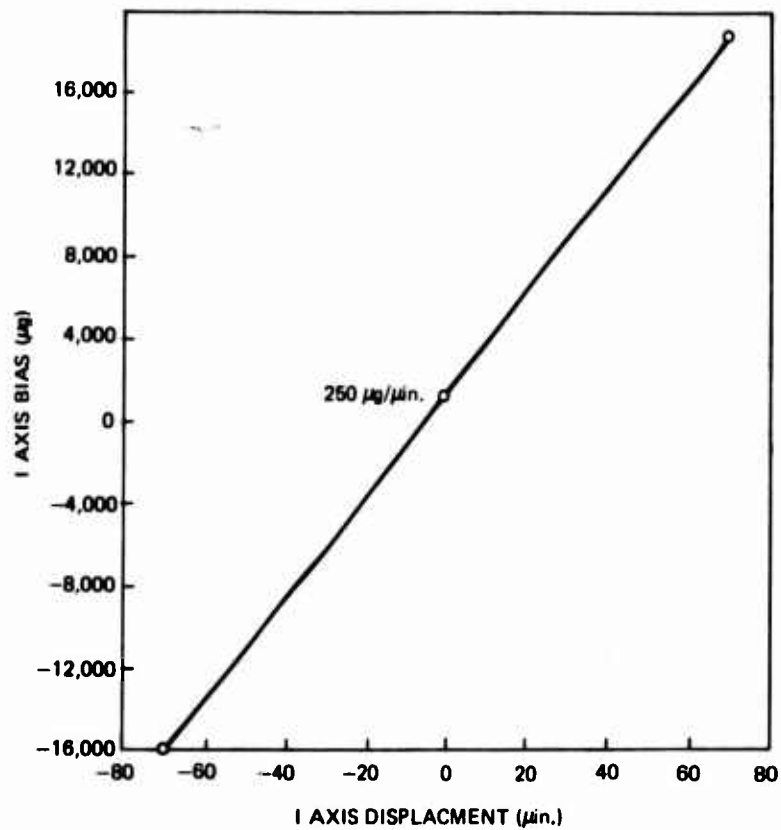


Figure 2-32. I-Axis acceleration bias sensitivity to I-Axis displacement.

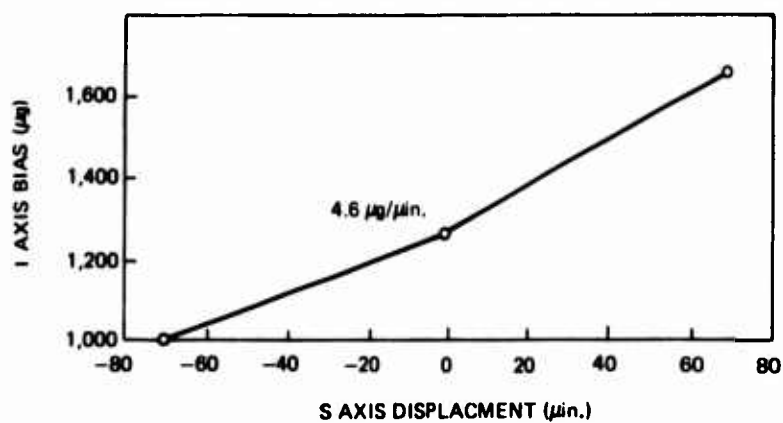


Figure 2-33. I-Axis acceleration bias sensitivity to S-Axis displacement.

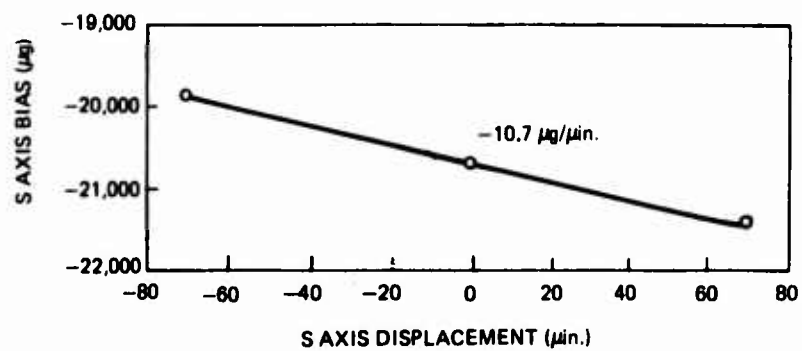


Figure 2-34. S-Axis acceleration bias sensitivity to S-Axis displacement.

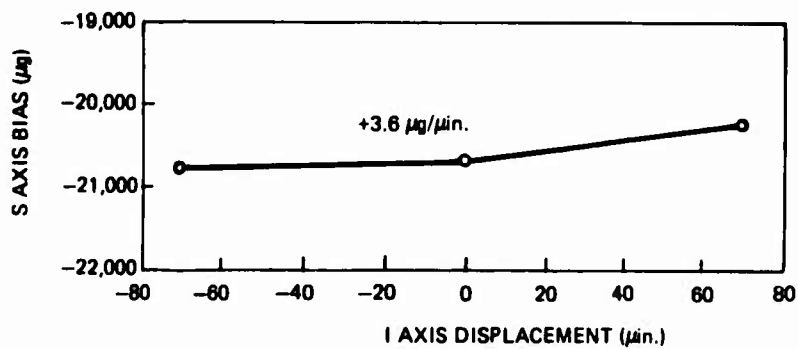


Figure 2-35. S-Axis acceleration bias sensitivity to I-Axis displacement.

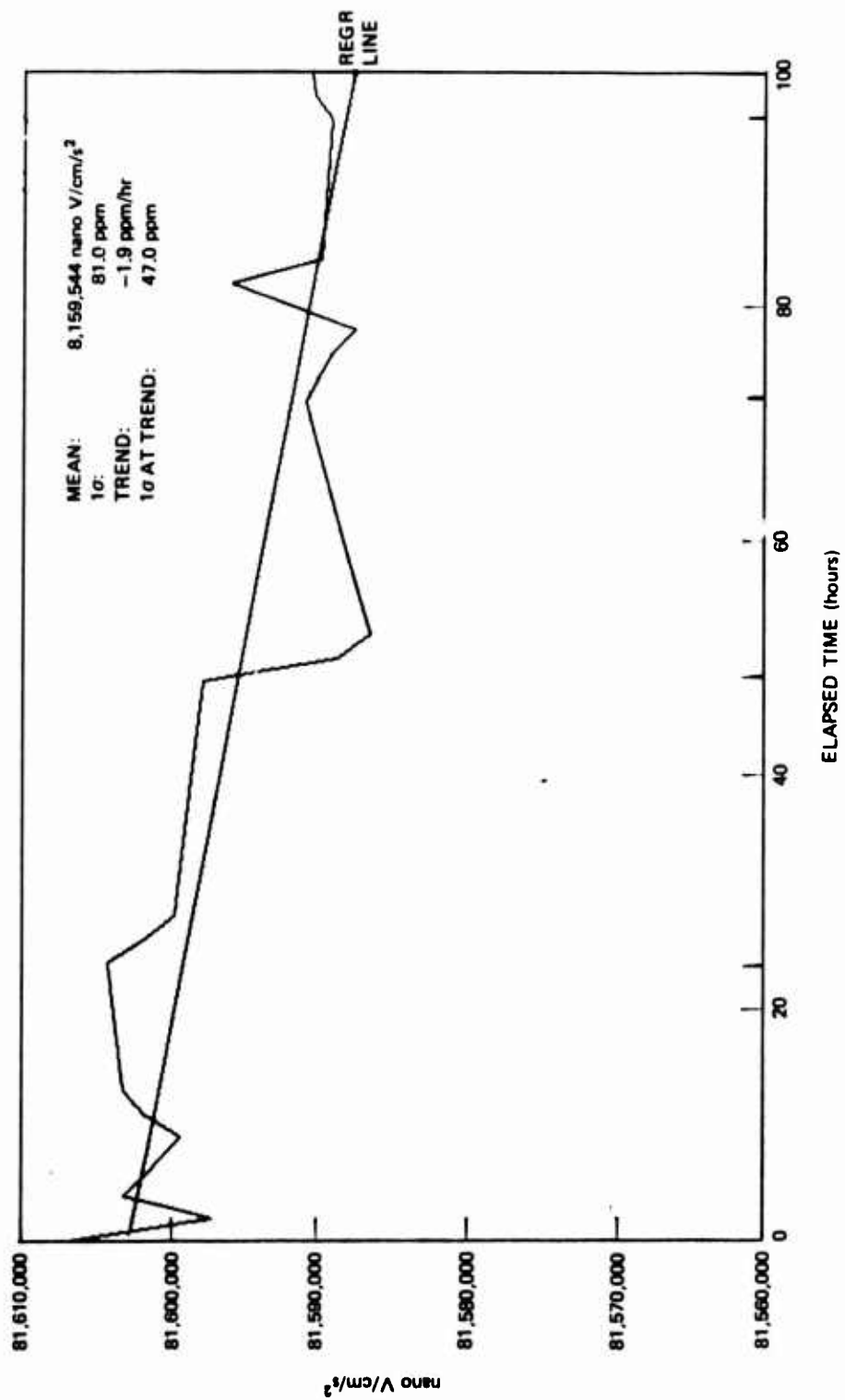


Figure 2-36. I-Axis acceleration scale factor stability.

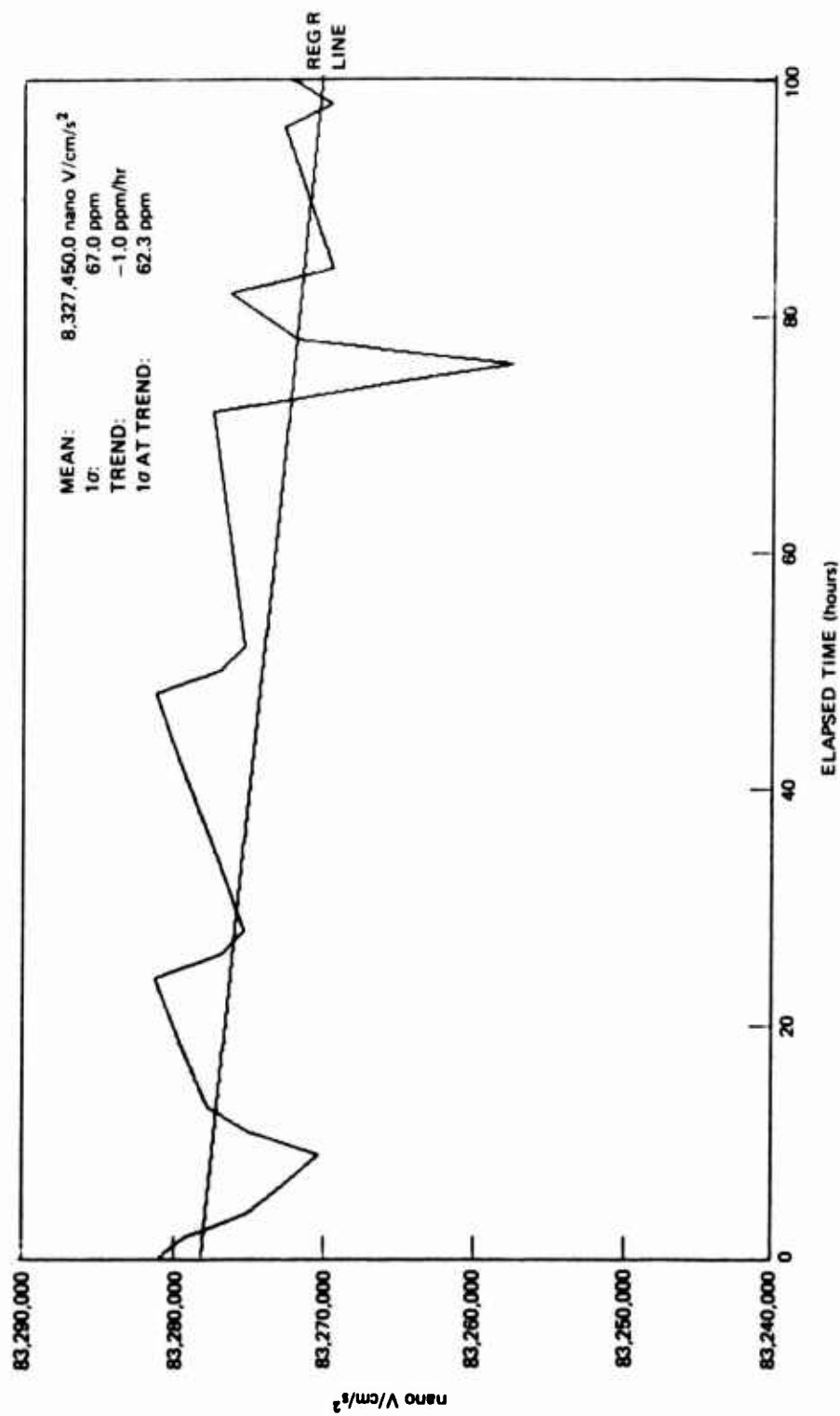


Figure 2-37. S-Axis acceleration scale factor stability.

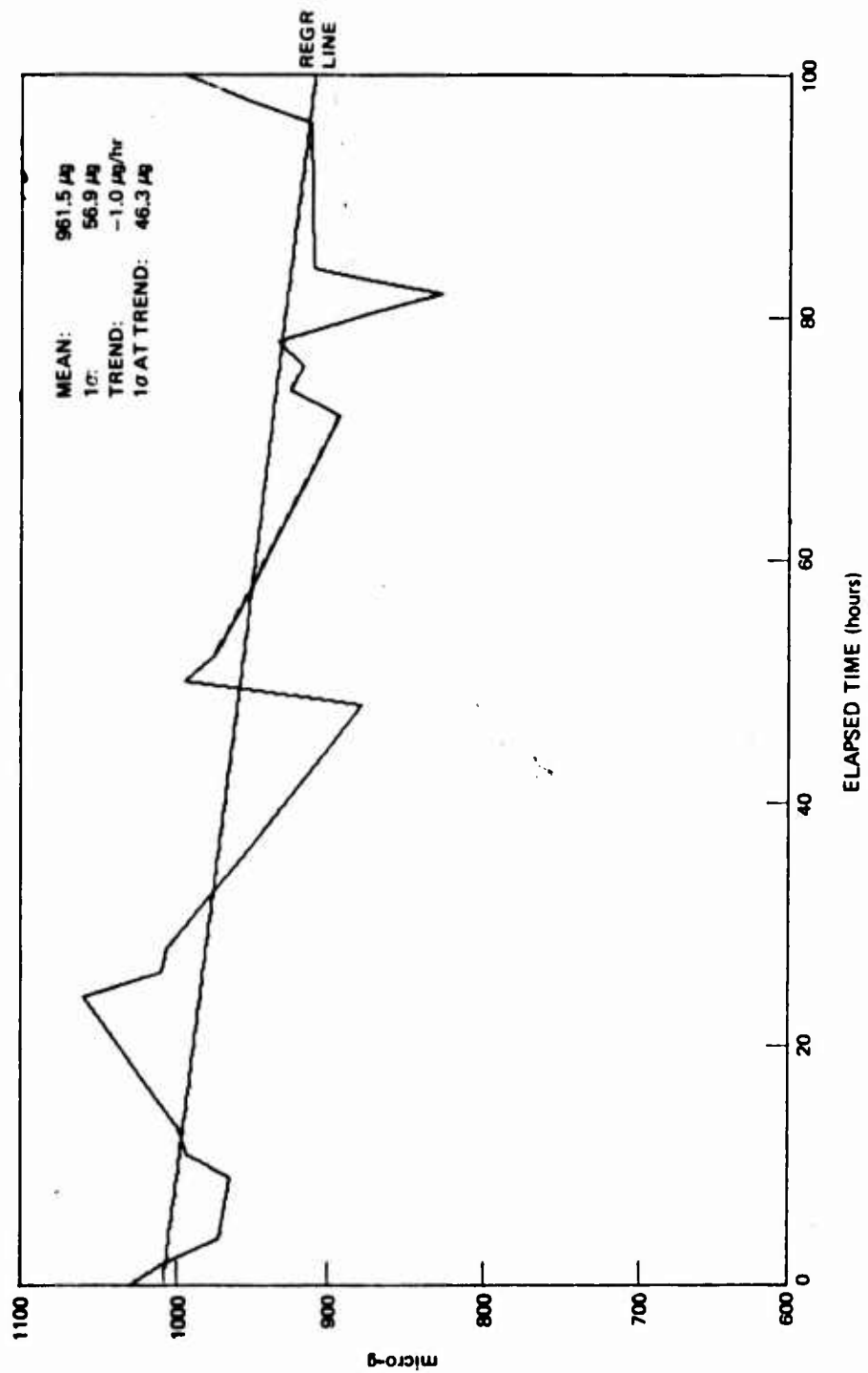


Figure 2-38. I-Axis acceleration bias stability 10/22 - 10/26/78.

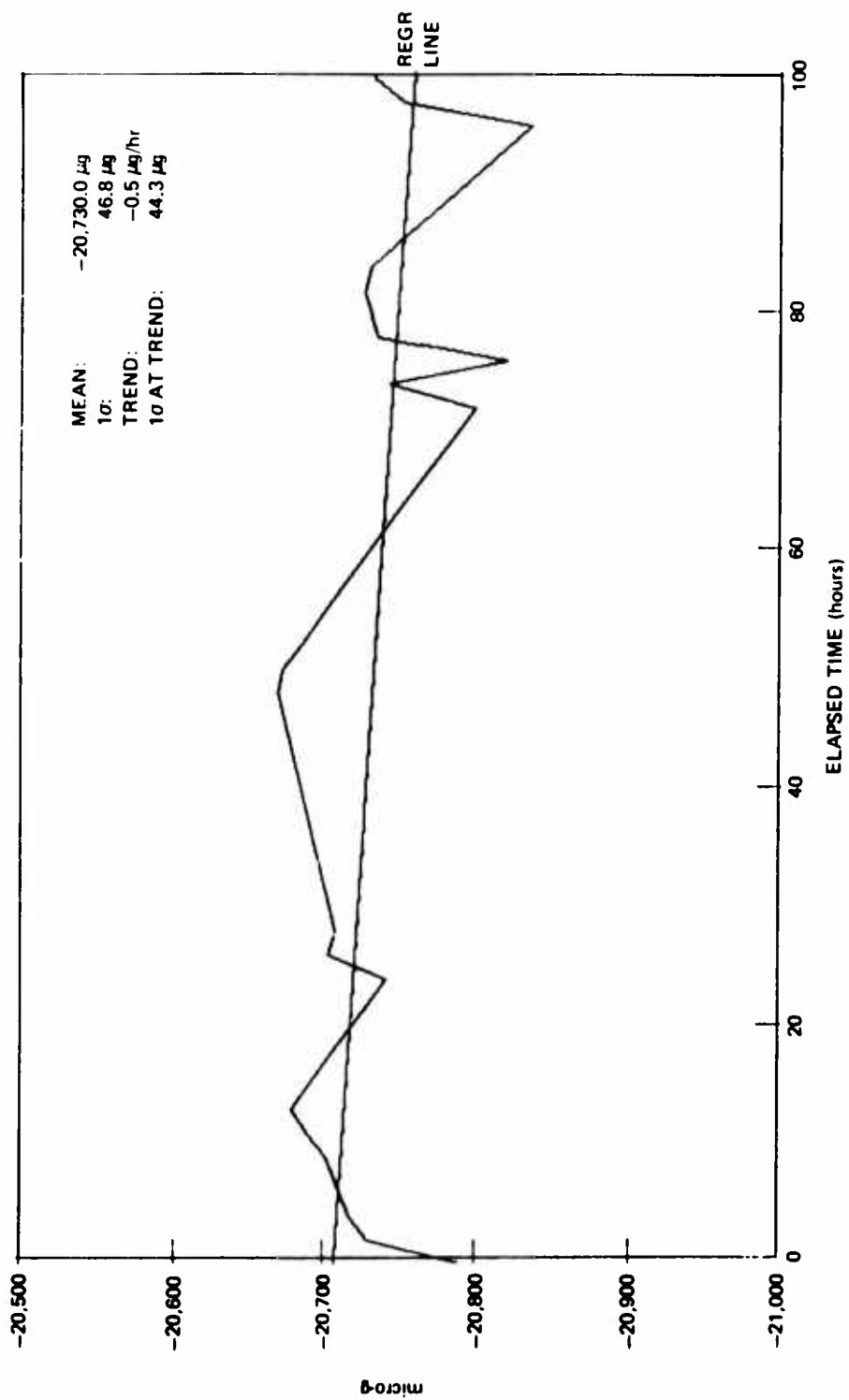


Figure 2-39. S-Axis acceleration bias stability 10/22 - 10/26/76.

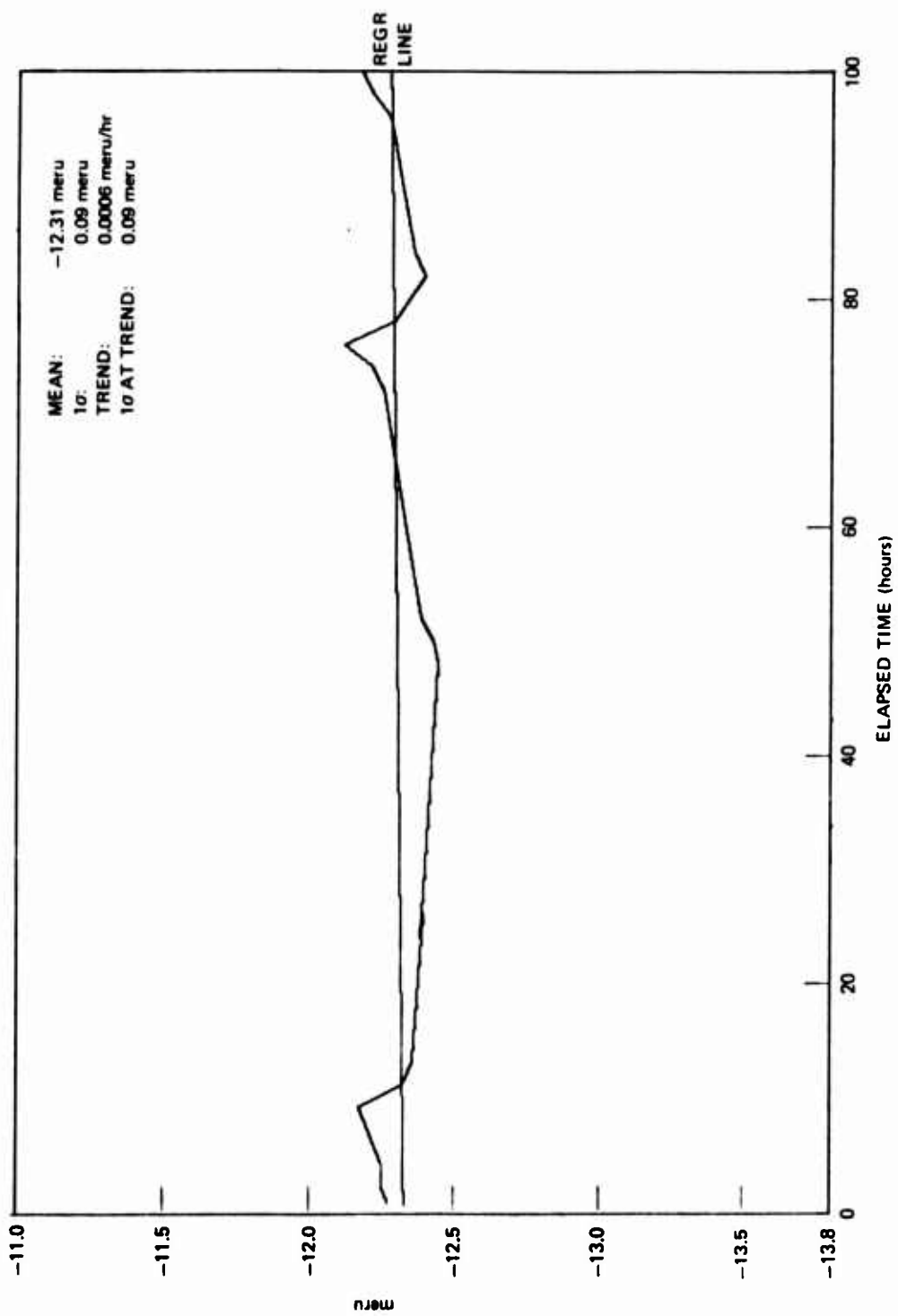


Figure 2-40. Gyro BD stability 10/22 - 10/26/76.

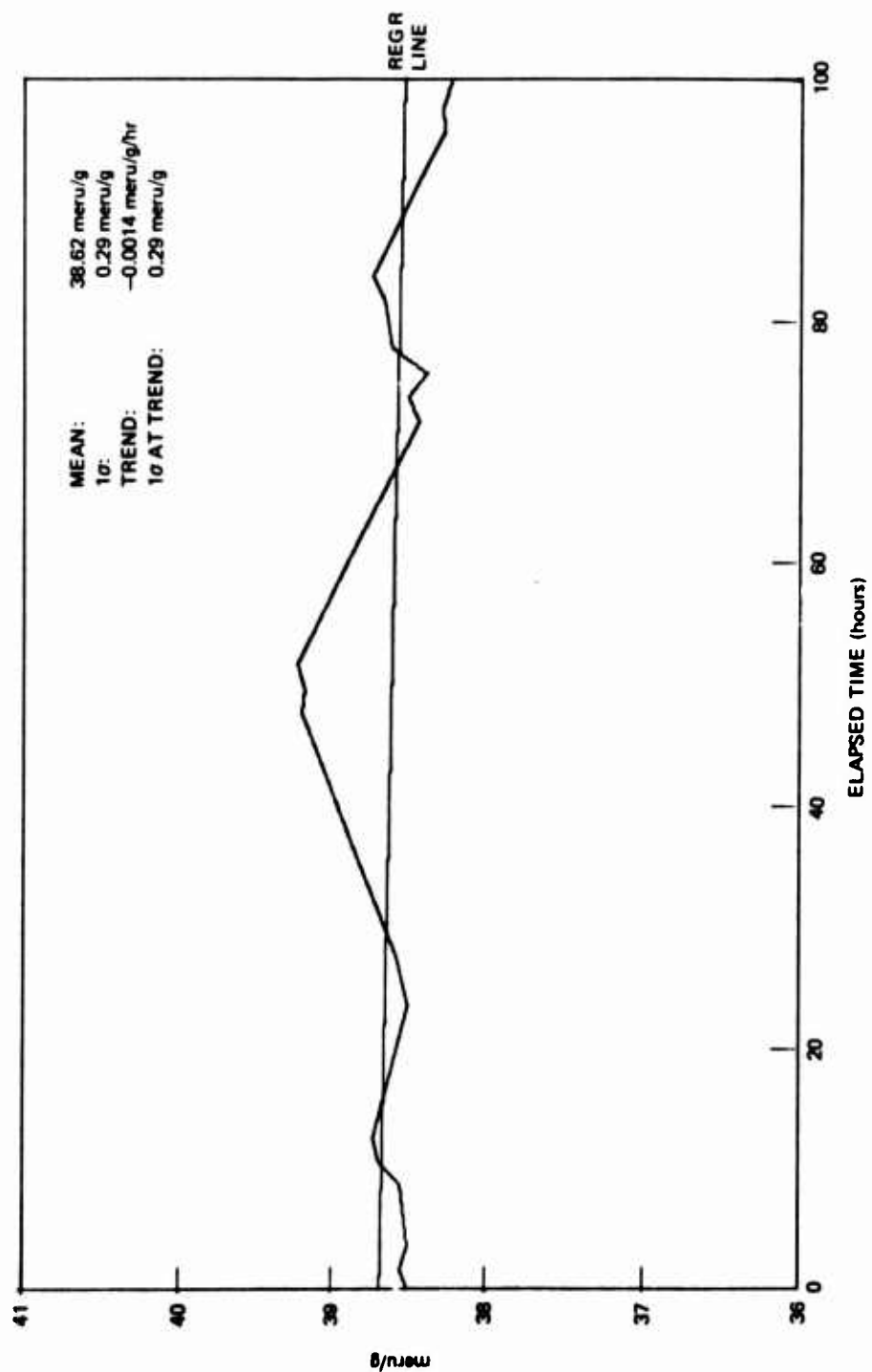


Figure 2-41. Gyro AD stability 10/22 - 10/26/76.

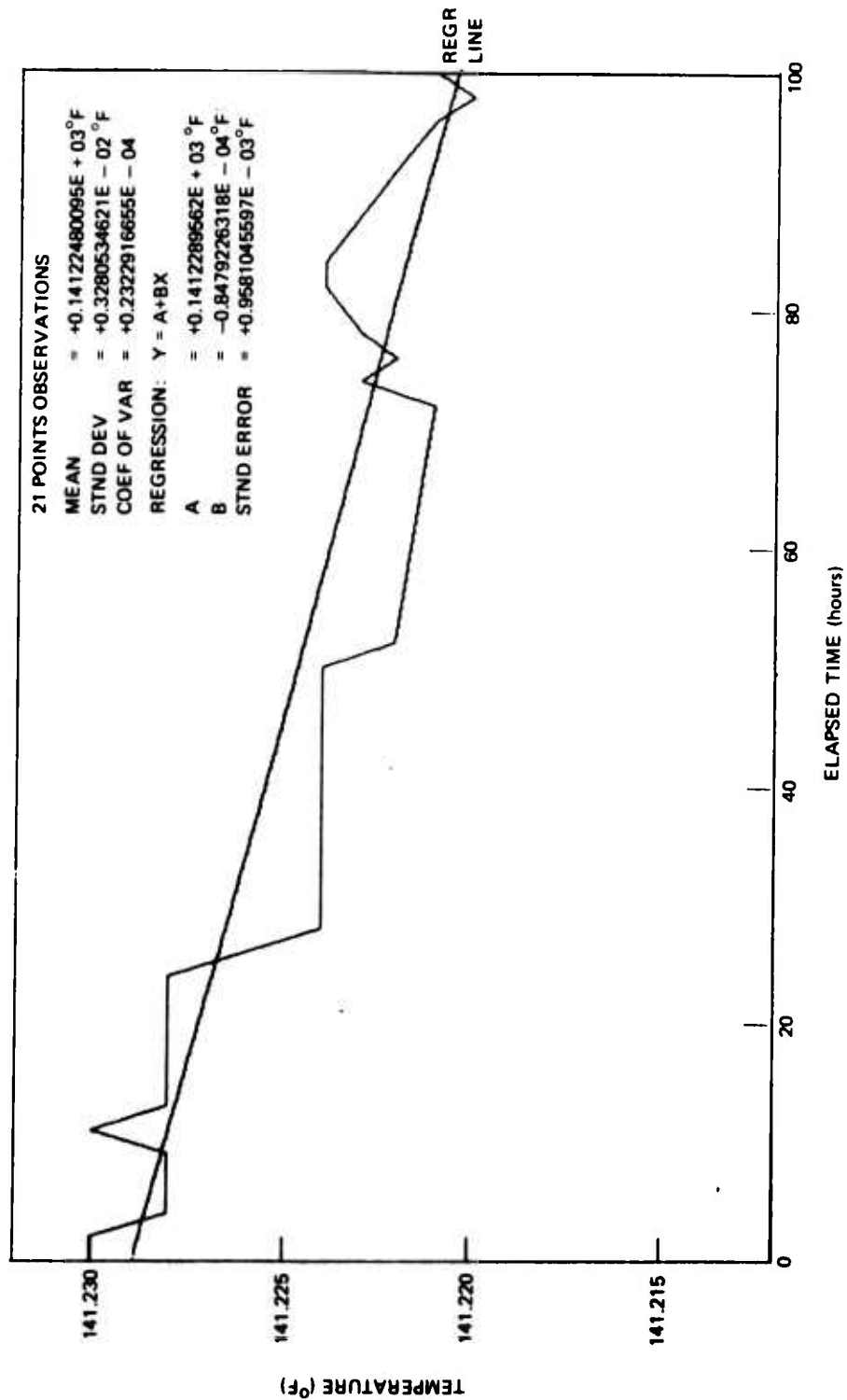


Figure 2-42. SG end housing temperature 10/22 - 10/26/76.

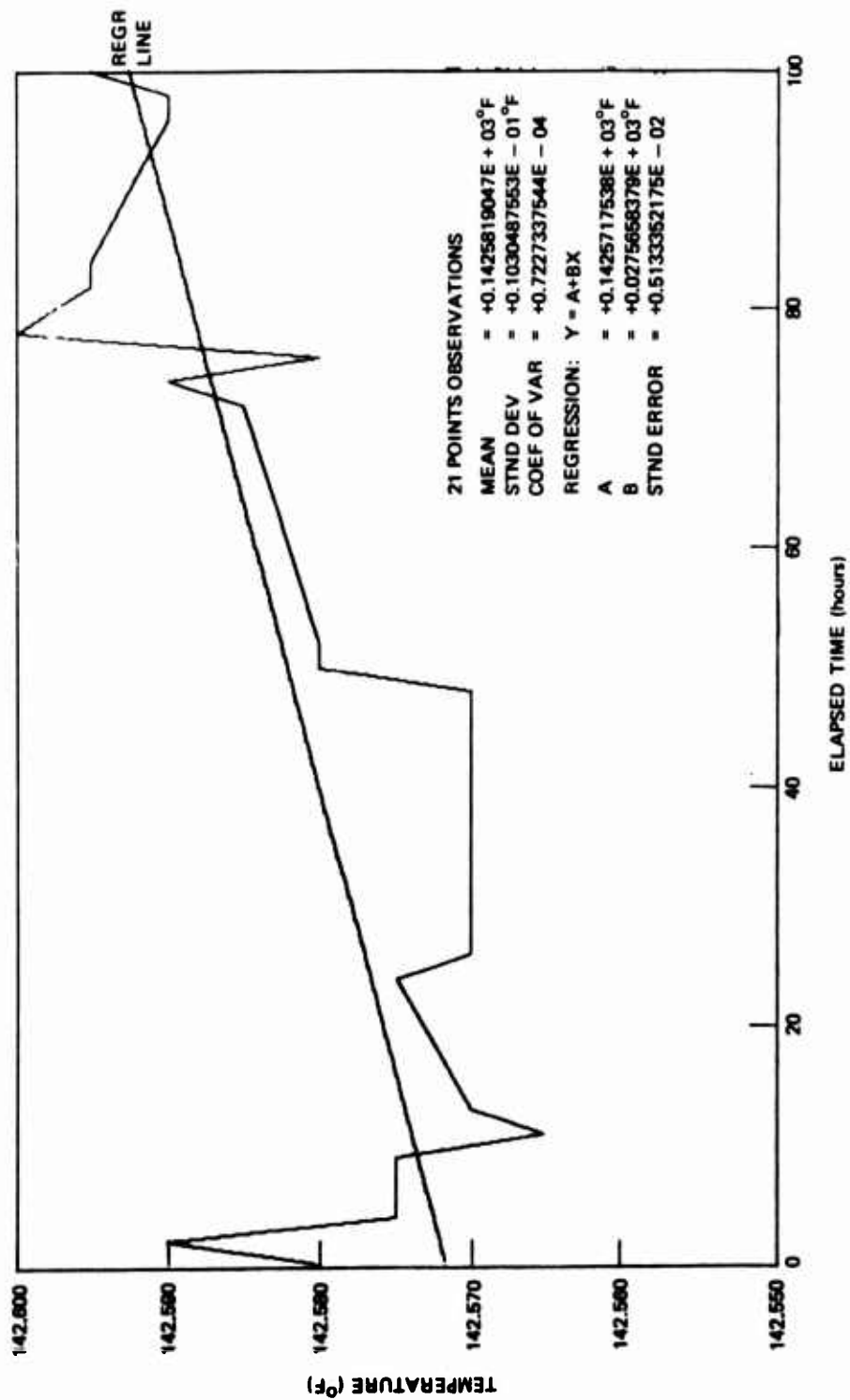


Figure 2-43. Case temperature 10/22 - 1/-26/76.

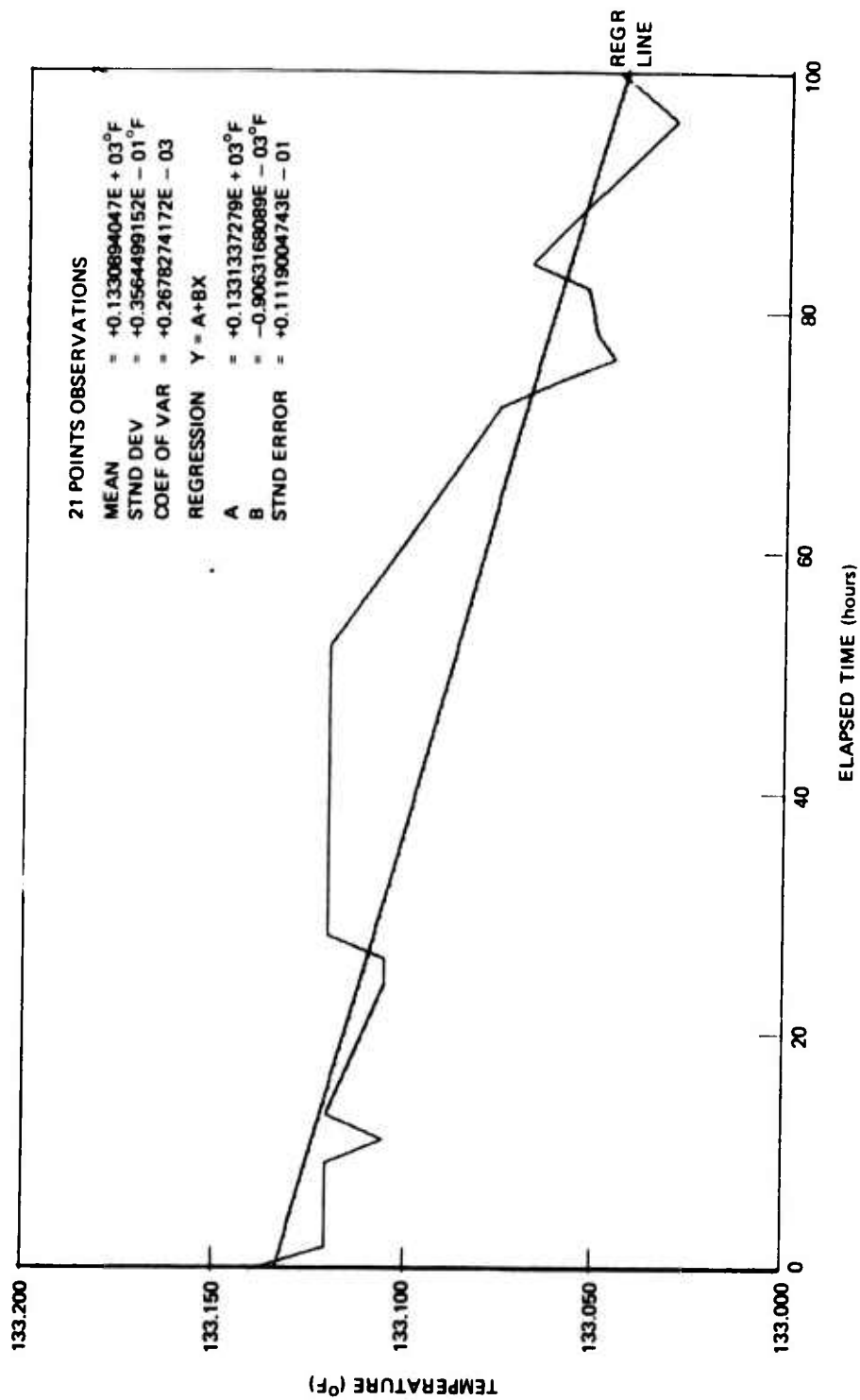


Figure 2-44. Base temperature 10/22 - 10/26/76.

I AXIS STABILITY 11/12 - 11/15/76

| 421 POINTS OBSERVATIONS | | REGRESSION: | | Y=A+BX | |
|-------------------------|---|-------------------|------------|--------|-------------------|
| MEAN | = | +0.5953262296E+01 | A | = | +0.5953752451E+01 |
| STND DEV | = | +0.3003836690E-03 | B | = | -0.1400440424E-04 |
| COEFF OF VAR | = | +0.5045698544E-04 | STND ERROR | = | +0.9796042158E-04 |

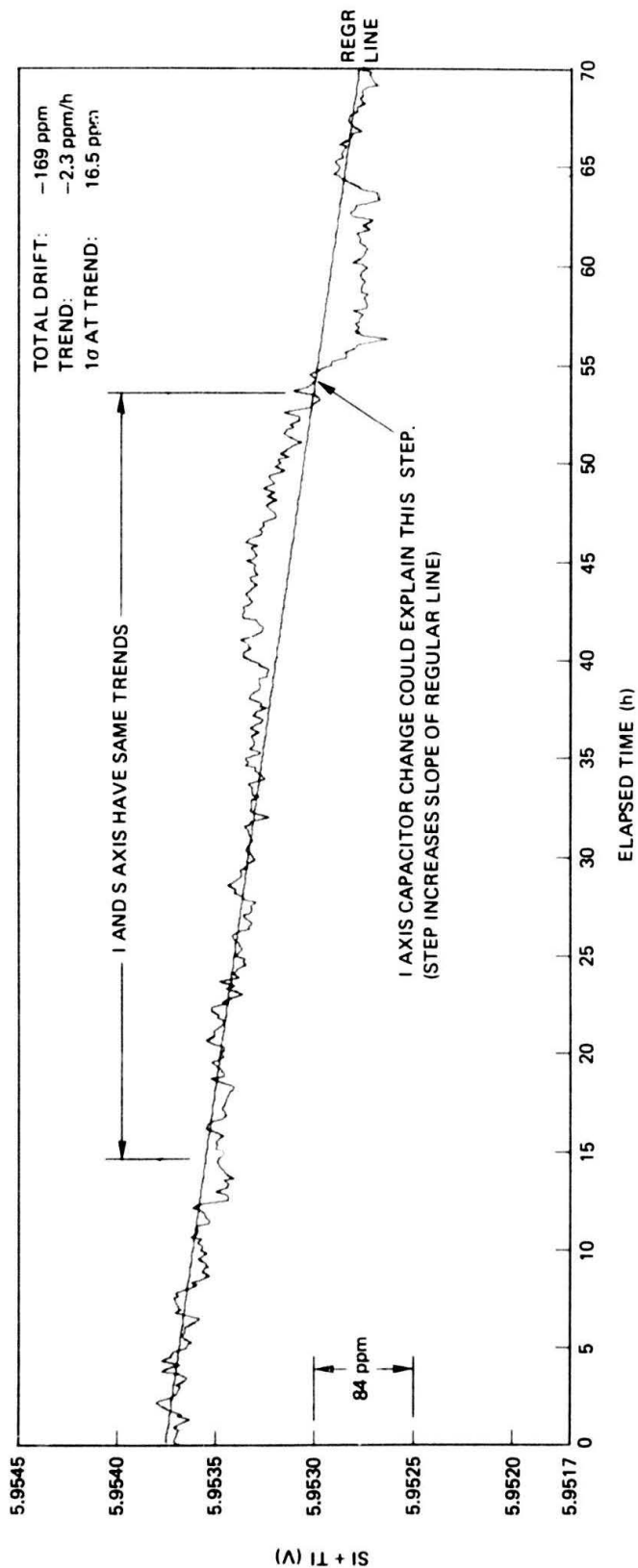


Figure 2-45. 72-Hour, I-Axis acceleration drift (IA - EA).

S AXIS STABILITY 11/12 - 11/15/76

421 POINTS OBSERVATIONS

MEAN = +0.5281745211E+01
 STND DEV = +0.1467455175E-03
 COEFF OF VAR = +0.2778352828E-04

REGRESSION: Y=A+BX

A = +0.5281830277E+01
 B = -0.2430436639E-05
 STND ERROR = +0.1383854887E-03

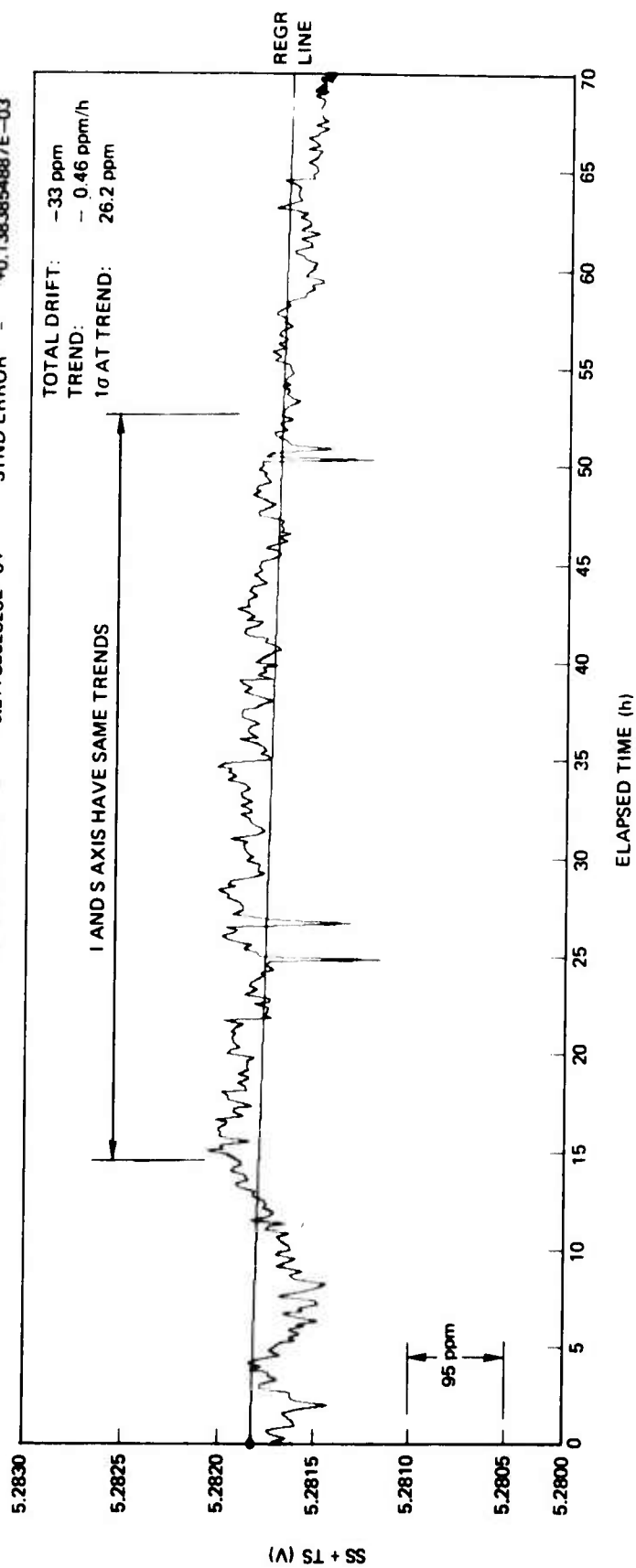


Figure 2-46. 72-Hour, S-Axis acceleration drift (SA || EA).

GYRO 11/12 - 11/15/76

421 POINTS OBSERVATIONS

| | | | | |
|--------------|---|-------------------|-------------|---------------------|
| MEAN | = | -0.4157649962E+02 | REGRESSION: | Y=A+BX |
| STND DEV | = | +0.6763686019E-01 | A | = -0.4159159079E+02 |
| COEFF OF VAR | = | -0.1626805066E-02 | B | = +0.4311755402E-03 |
| | | | STND ERROR | = +0.671492517E-01 |

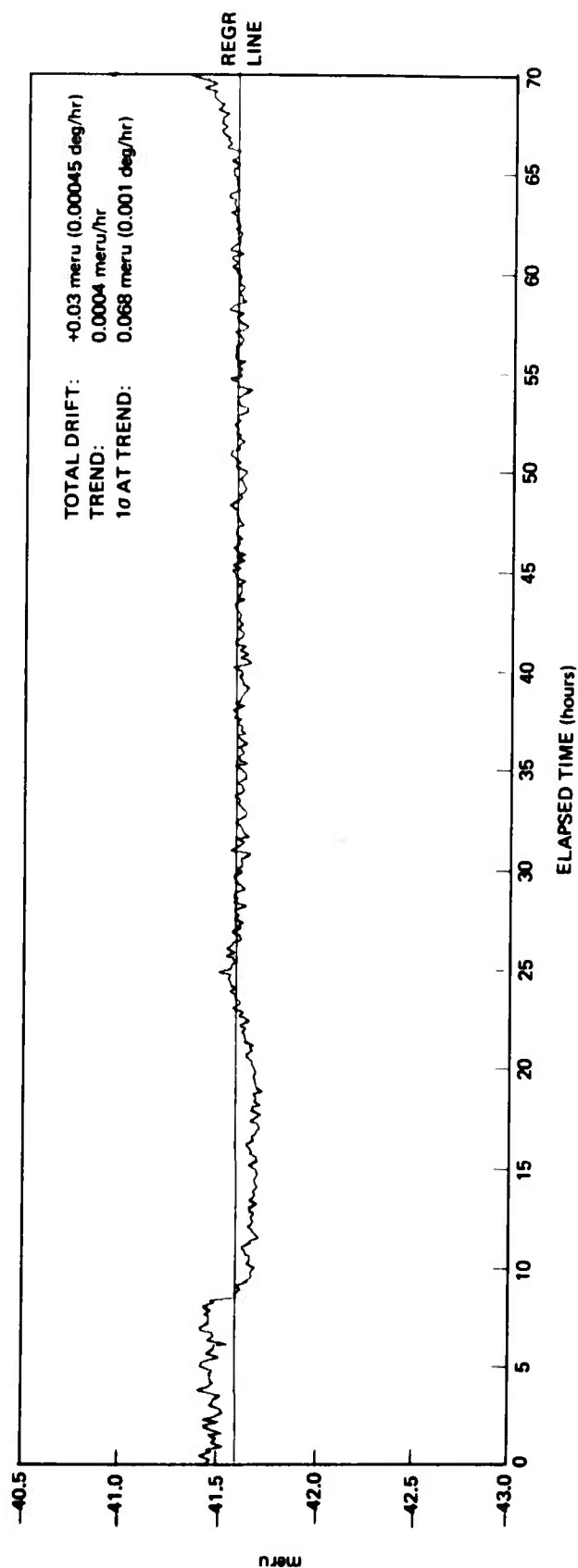


Figure 2-47. 72-Hour gyro drift (IA ⊥ EA).

SG + 1A THERMISTOR 11/12 - 11/15/76

| | | | |
|------------------------|--------------------|-------------|---------------------|
| 421 POINTS OBSERVATION | | REGRESSION: | Y = A + BX |
| MEAN | = 0.1410742263E+03 | A | = +0.1410753569E+03 |
| STND DEV | = 0.1221229012E-02 | B | = -0.3230283625E-04 |
| COEFF OF VAR | = 0.8656641574E-05 | STND ERROR | = +0.1031892523E-02 |

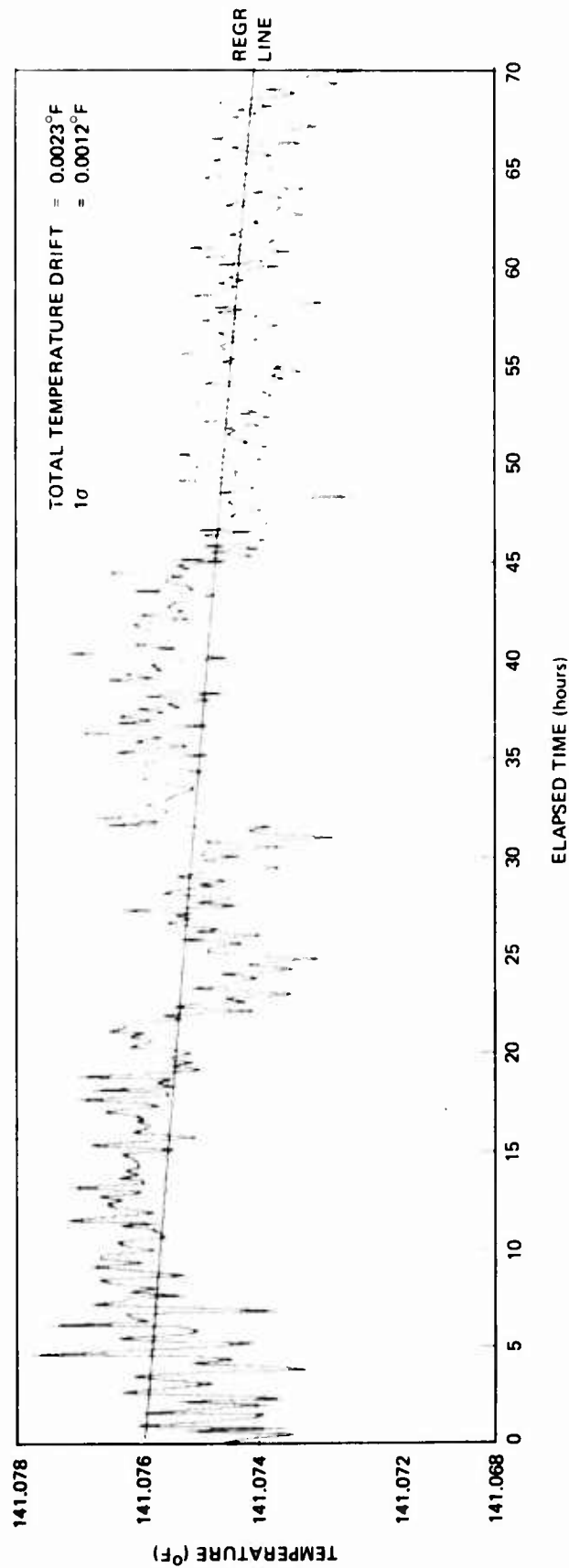


Figure 2-48. 72-Hour, SG end housing temperature.

NORTH-SOUTH TILT 11/12 - 11/15/76

421 POINTS OBSERVATIONS

MEAN = +0.2055328048E+01
 STND DEV = +0.6371027281E+00
 COEFF OF VAR = +0.3098761759E+00

REGRESSION: Y=A+BX

A = +0.1796545410E+01
 B = +0.7393774850E-02
 STND ERROR = +0.6199455170E+00

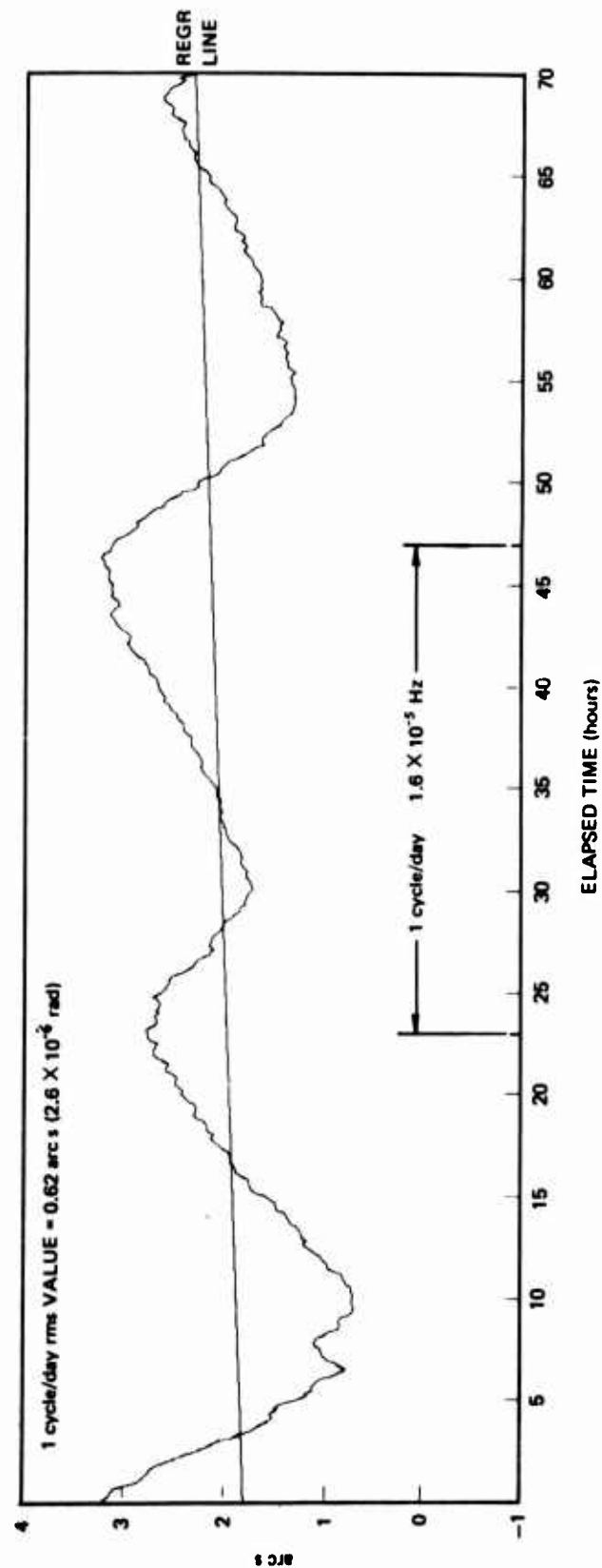


Figure 2-49. 72-Hour, table tilt, north-south plane.

EAST-WEST TILT 11/12 - 11/15/76

421 POINTS OBSERVATIONS

MEAN = +0.2075551815E+01
 STND DEV = +0.8128659343E+00
 COEFF OF VAR = +0.3916384685E+00

REGRESSION: $Y = A + BX$

A = +0.2094051487E+01
 B = -0.5285610074E-03
 STND ERROR = +0.8137646029E+00

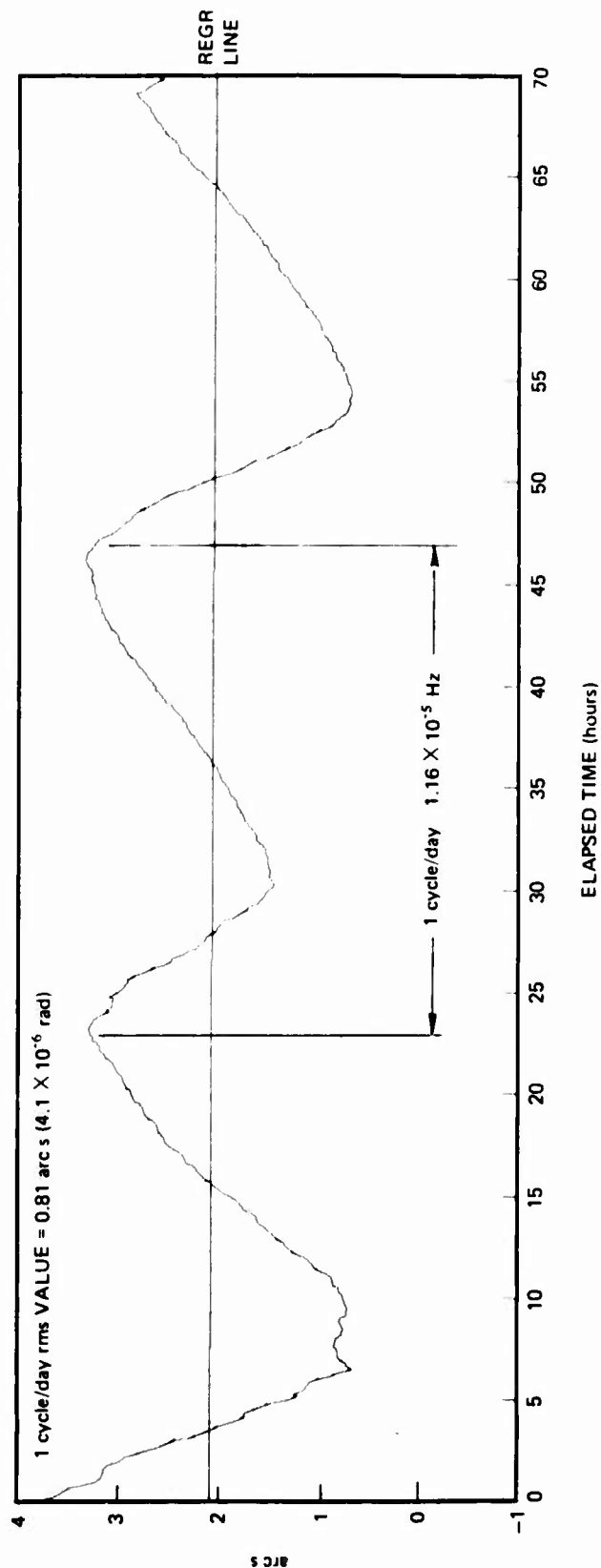


Figure 2-50. 72-Hour, table tilt, east-west plane.

DELTA WHEEL POWER 11/12 - 11/15/76

421 POINTS OBSERVATIONS

MEAN = -0.7487732943E-02
 STND DEV = +0.1357129389E-02
 COEFF OF VAR = -0.1812470342E+00

REGRESSION: Y=A+BX

A = -0.6397906255E-02
 B = -0.3113784325E-04
 STND ERROR = +0.1202707127E-02

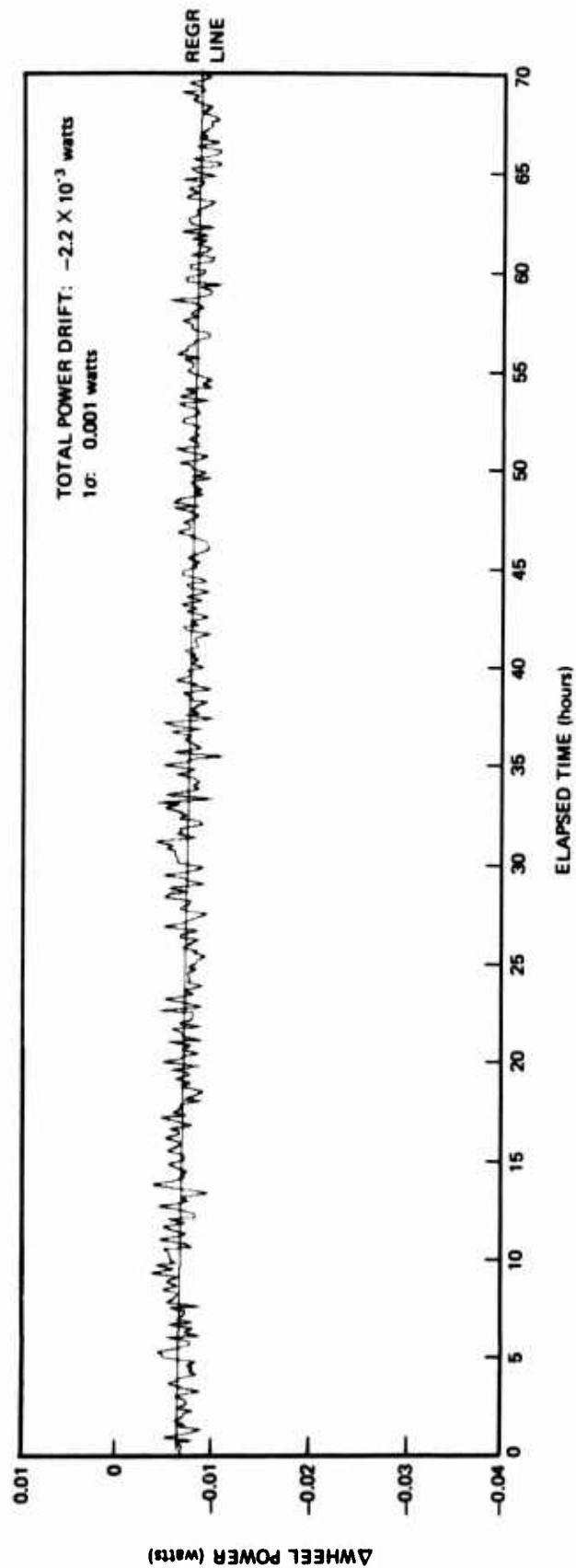


Figure 2-51. 72-Hour normalized wheel power.

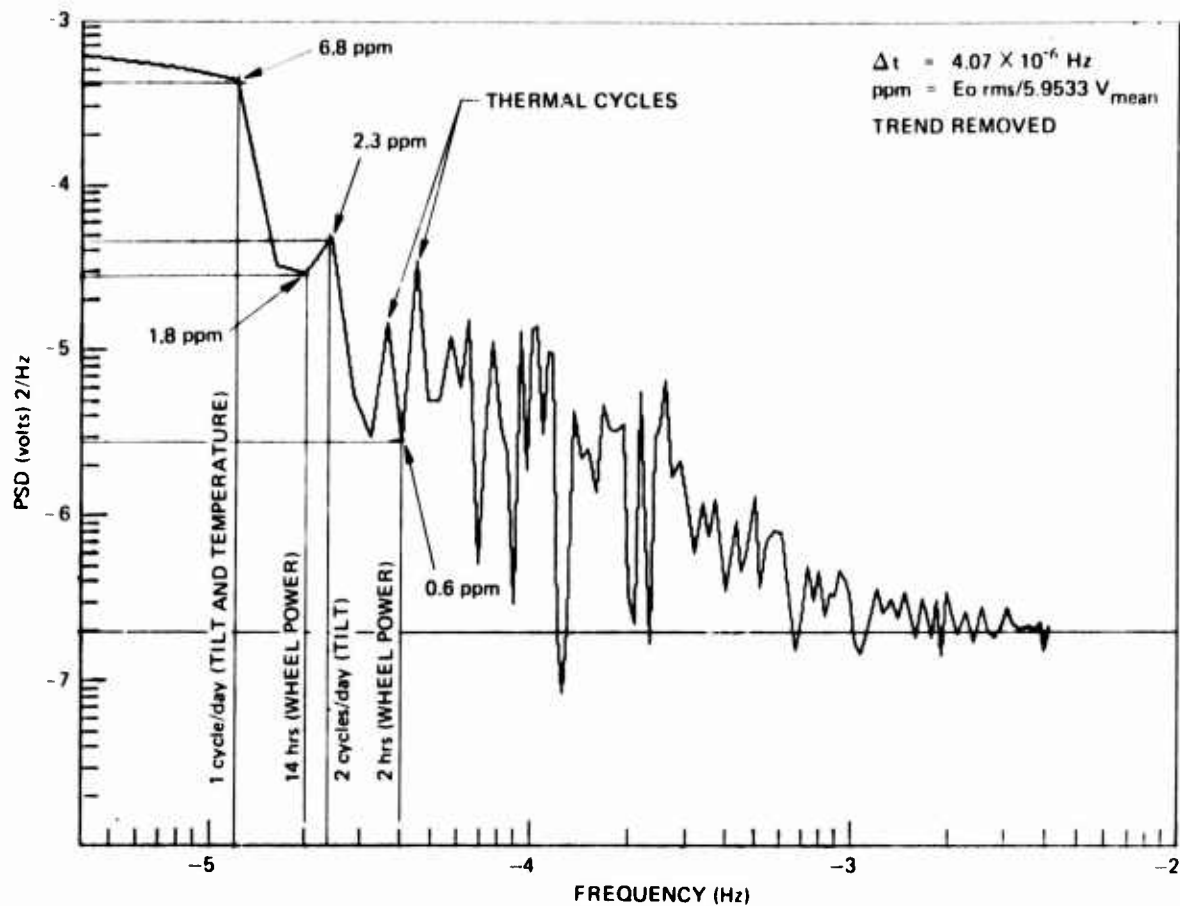


Figure 2-52. I-Axis accelerometer power spectrum (trend removed).

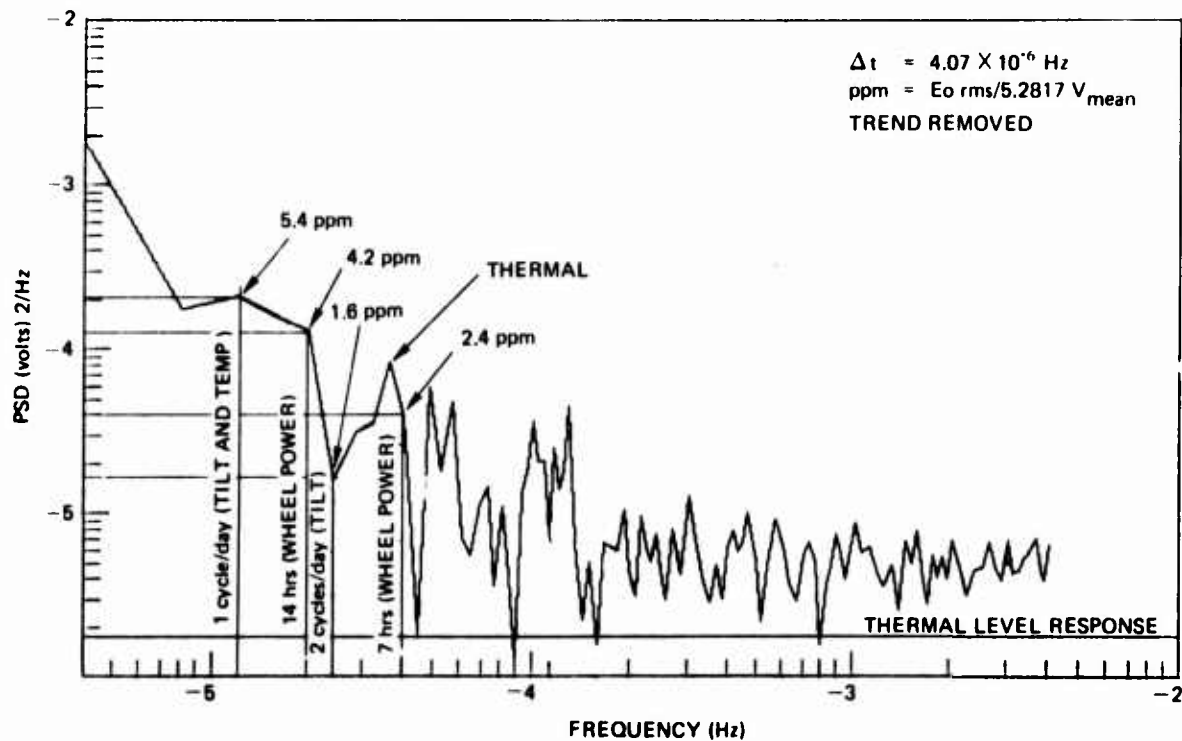


Figure 2-53. S-Axis accelerometer power spectrum (trend removed).

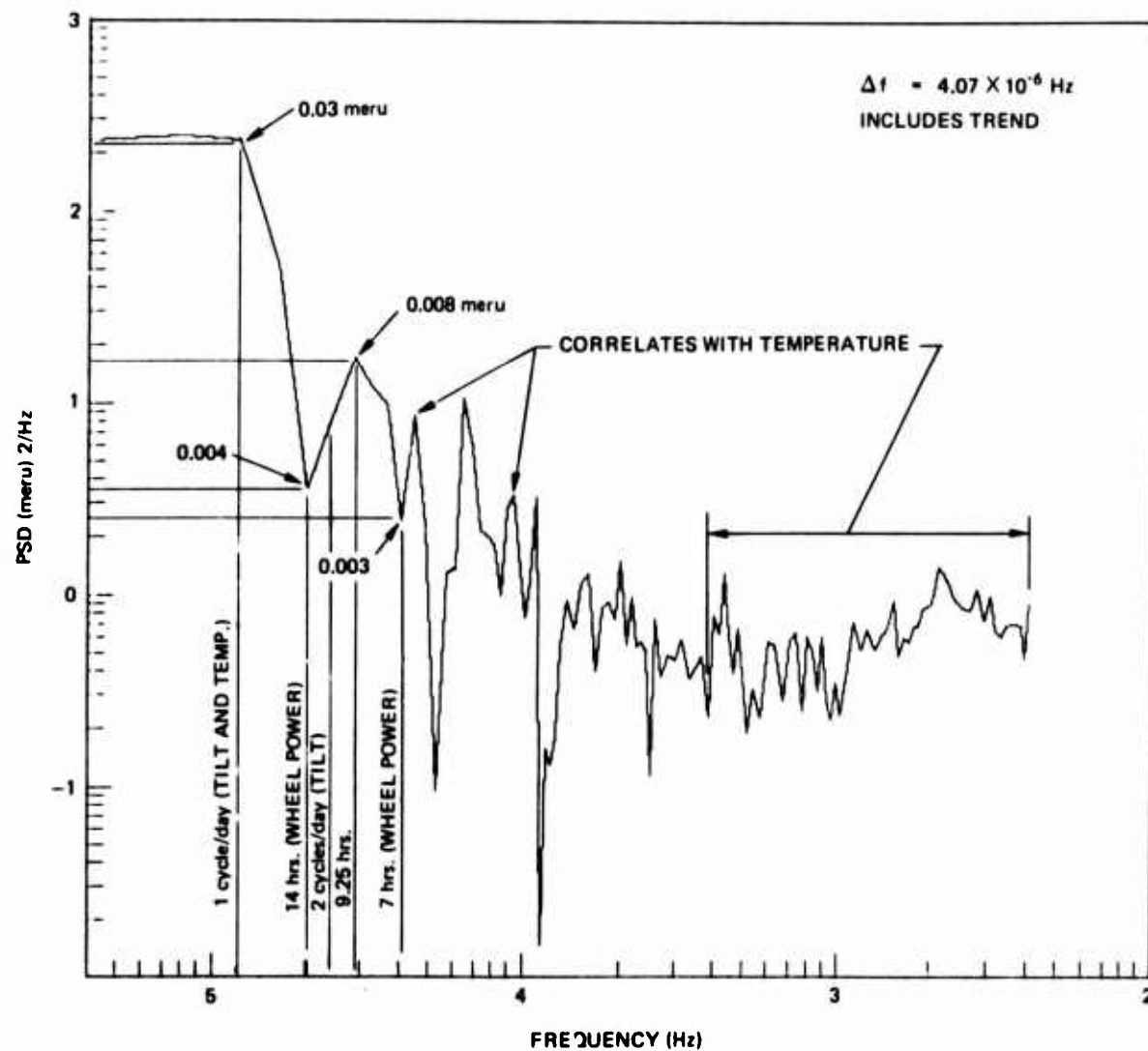


Figure 2-54. Power spectrum of gyro torque (includes trend).

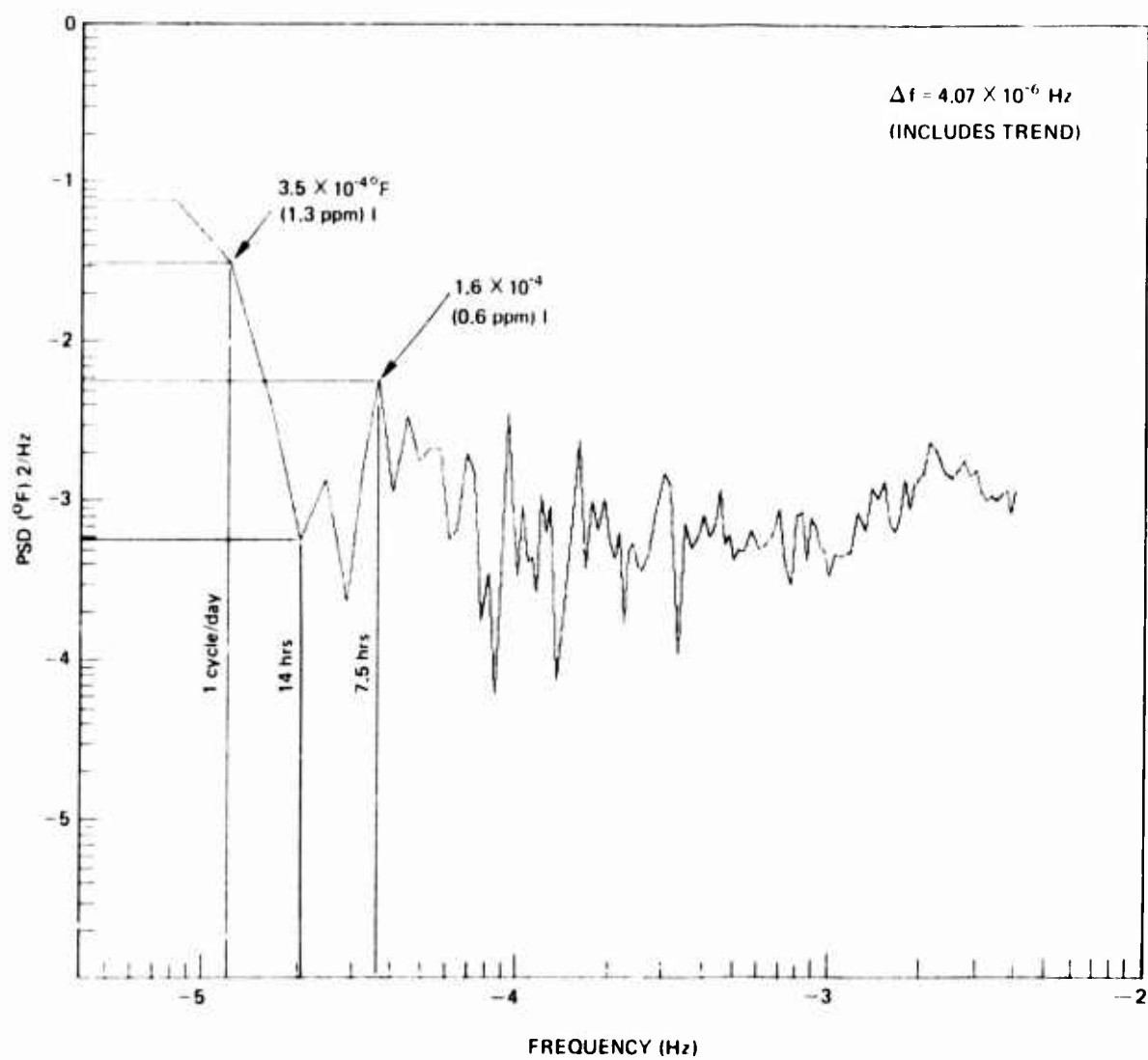


Figure 2-55. Power spectrum of temperature (includes trend).

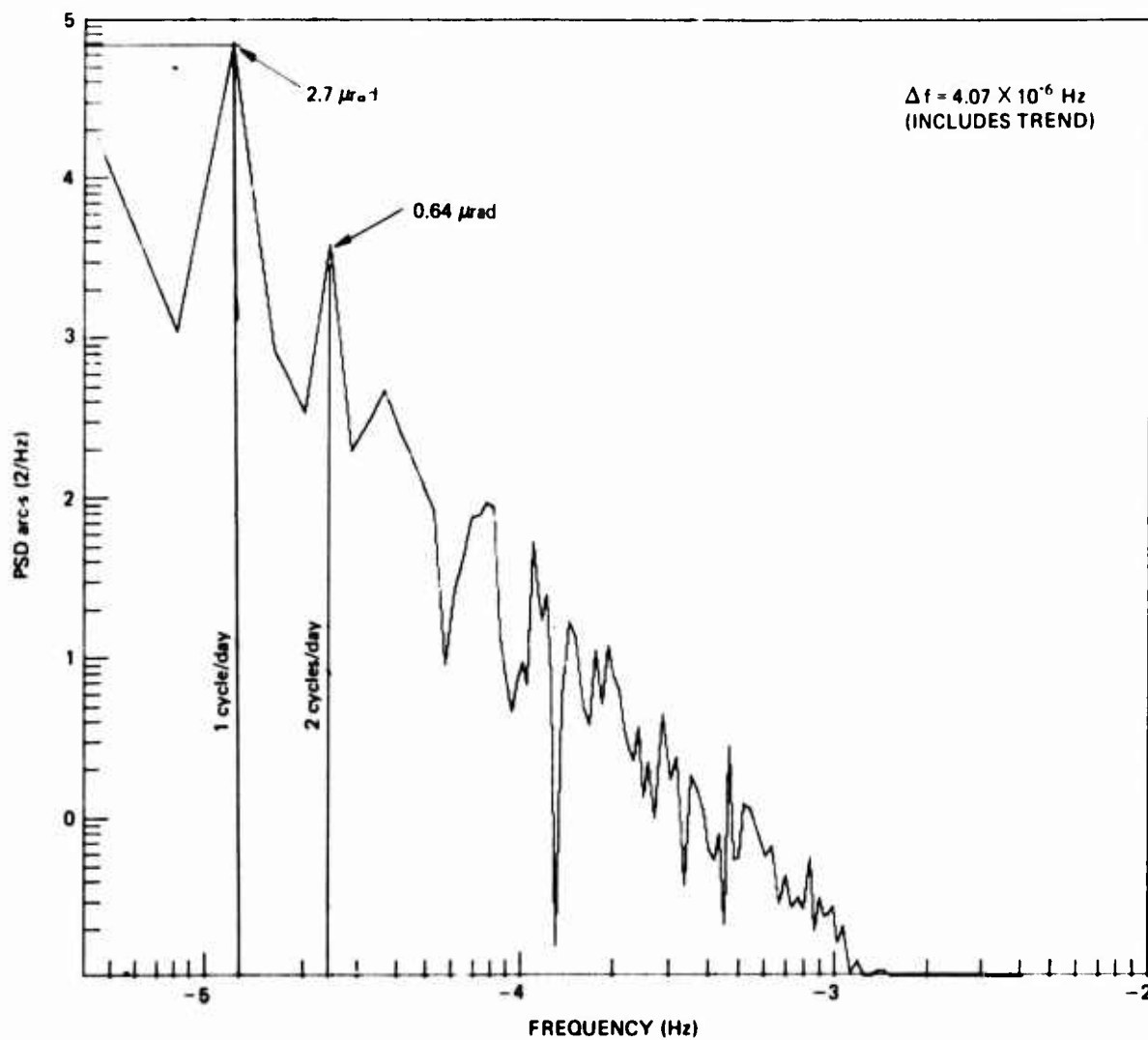


Figure 2-56. Power spectrum of north-south table tilt (includes trend).

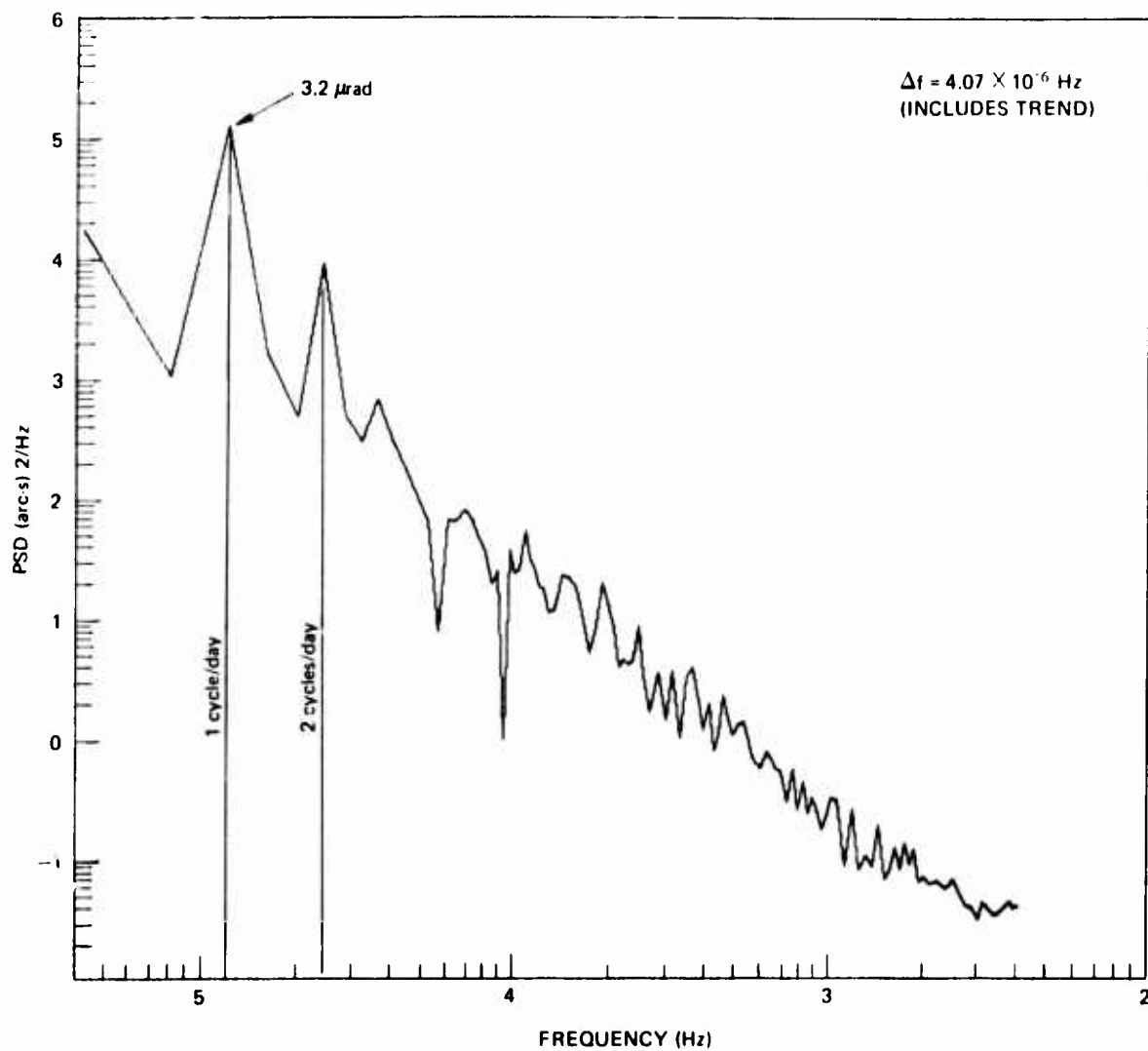


Figure 2-57. Power spectrum of east-west table tilt (includes trend).

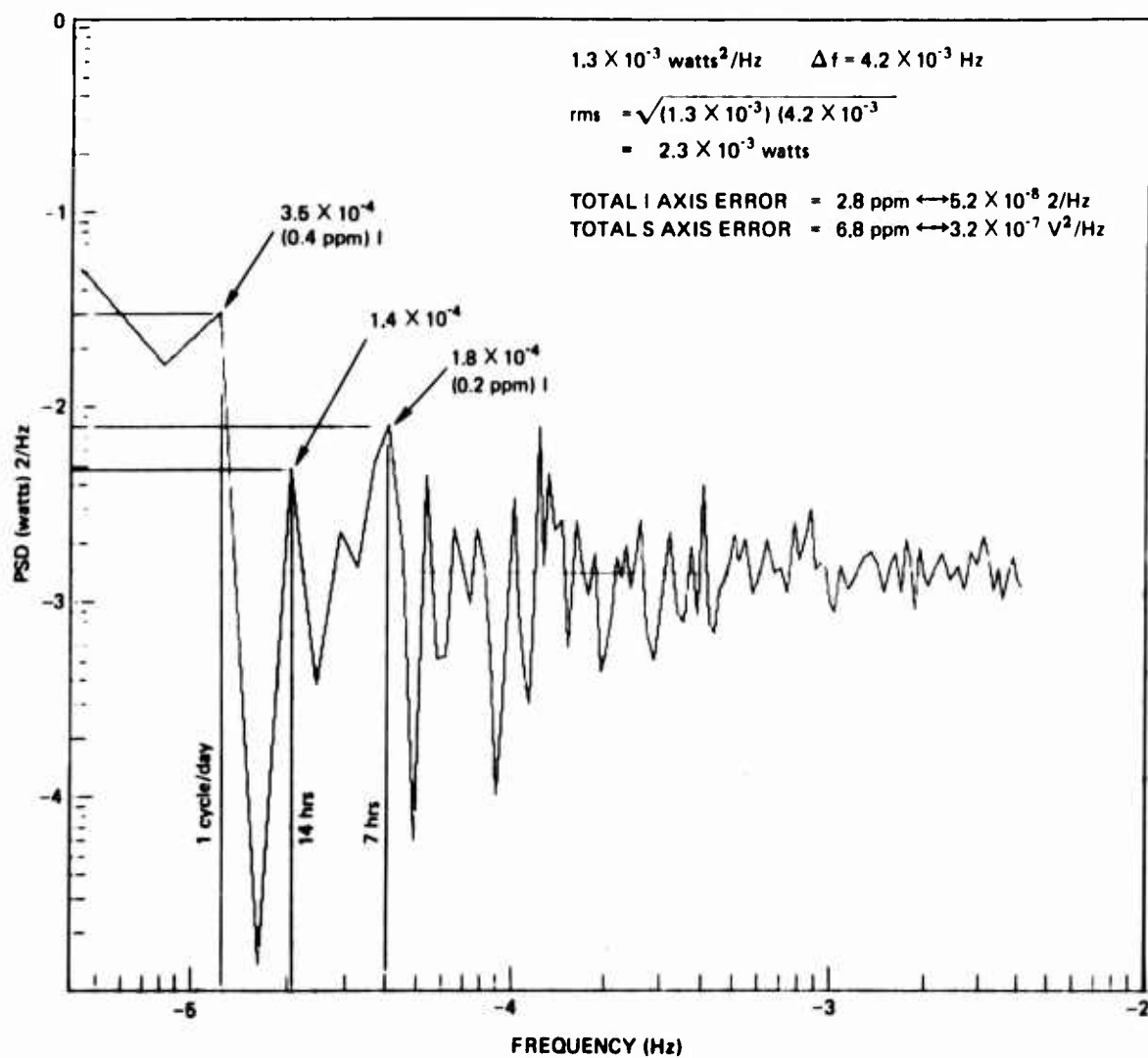


Figure 2-58. Power spectrum of wheel power.

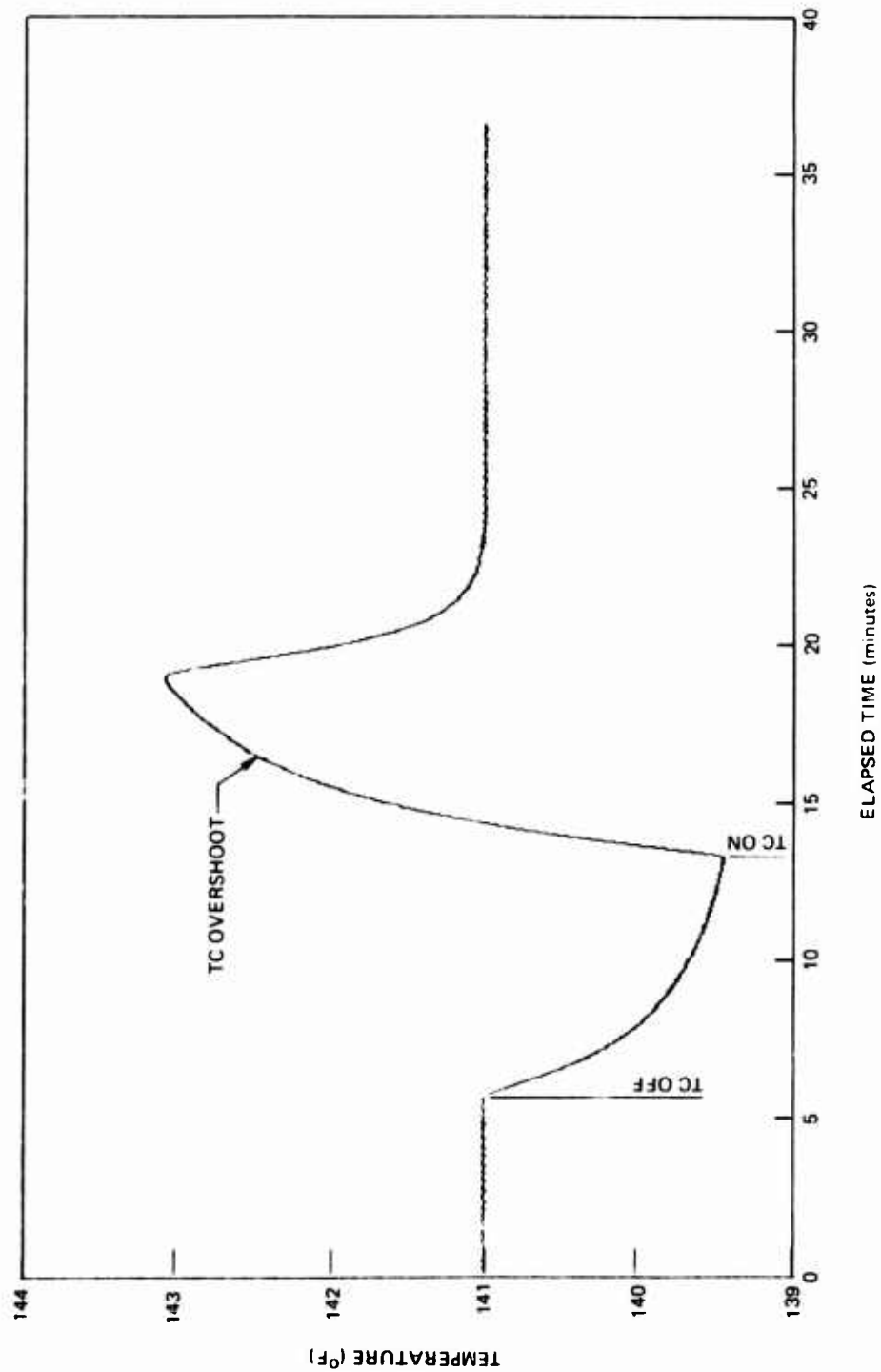


Figure 2-59. SG end housing temperature (12/13/76).

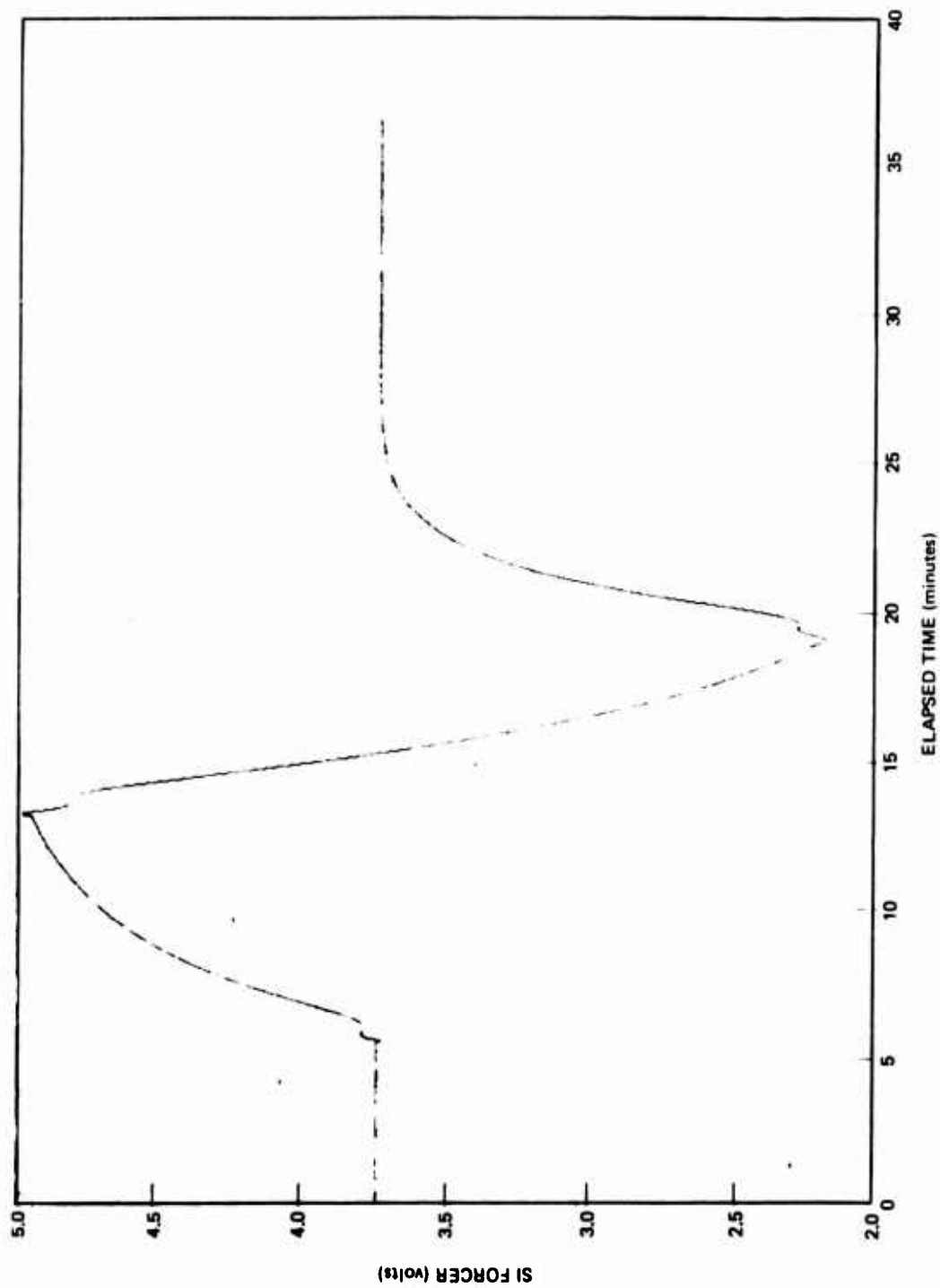


Figure 2-60. SI forcer temperature reaction.

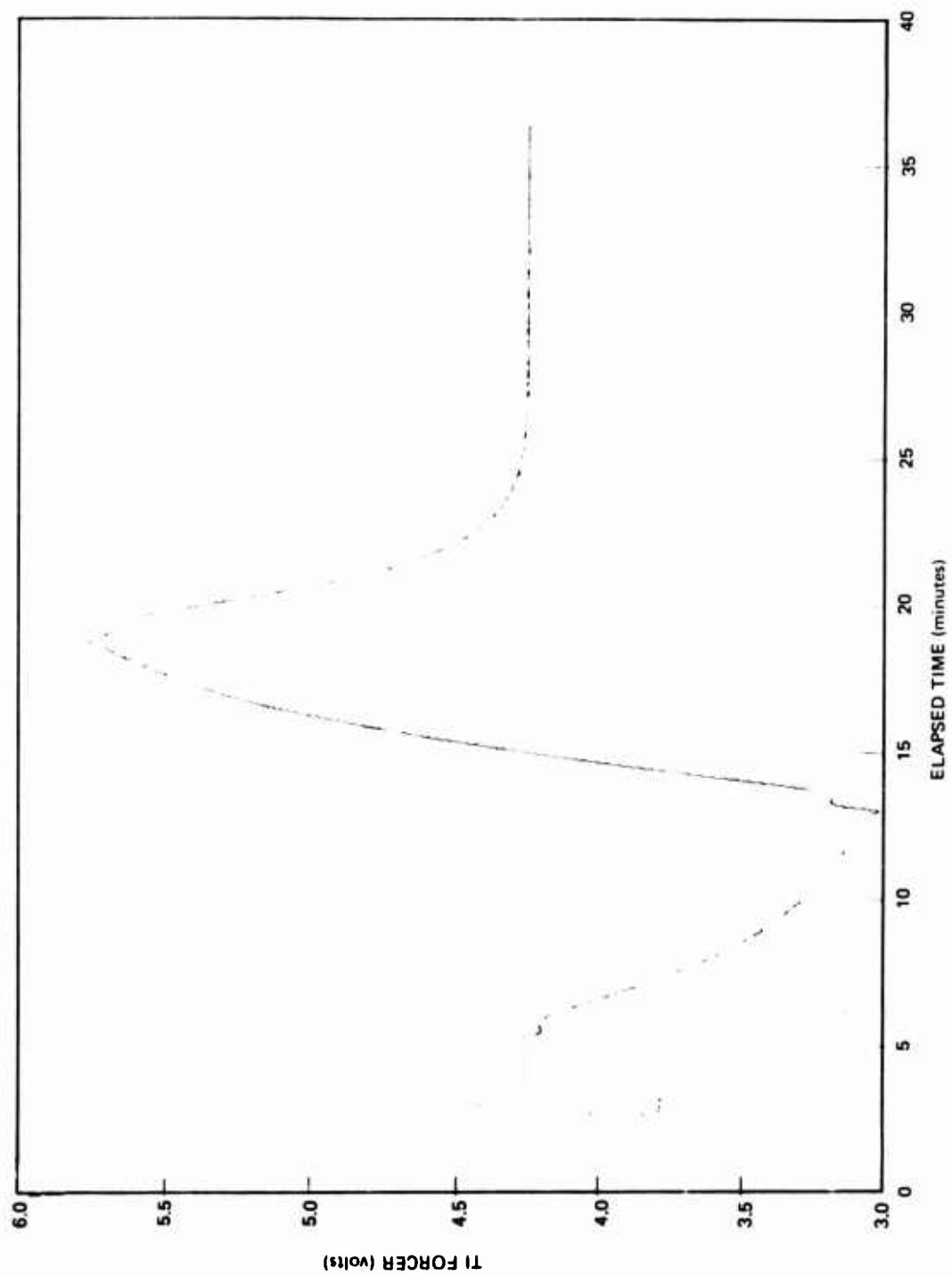


Figure 2-61. TI forcer temperature reaction.

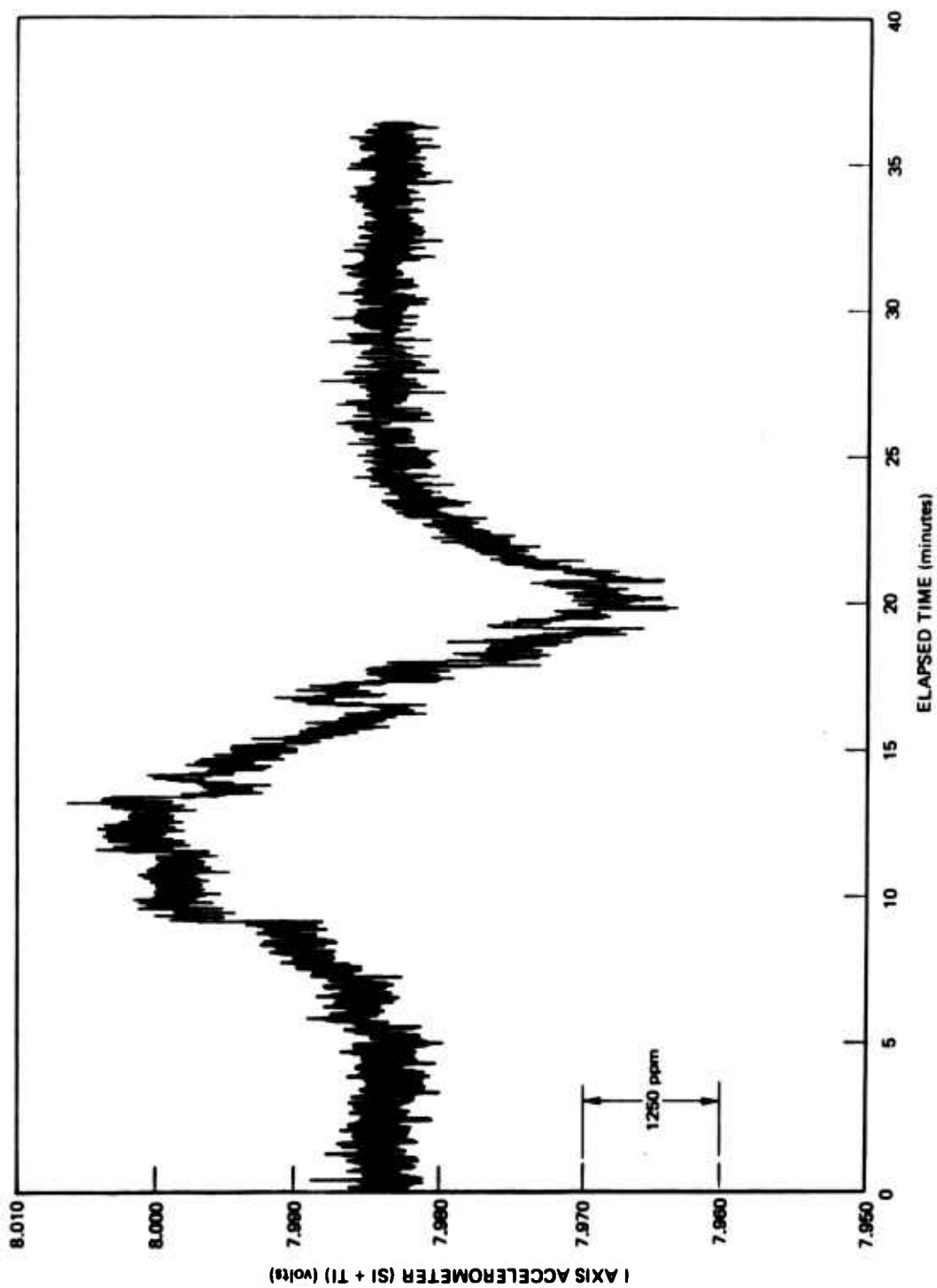


Figure 2-62. I-Axis acceleration temperature reaction (IA vertical) (12/13/76).

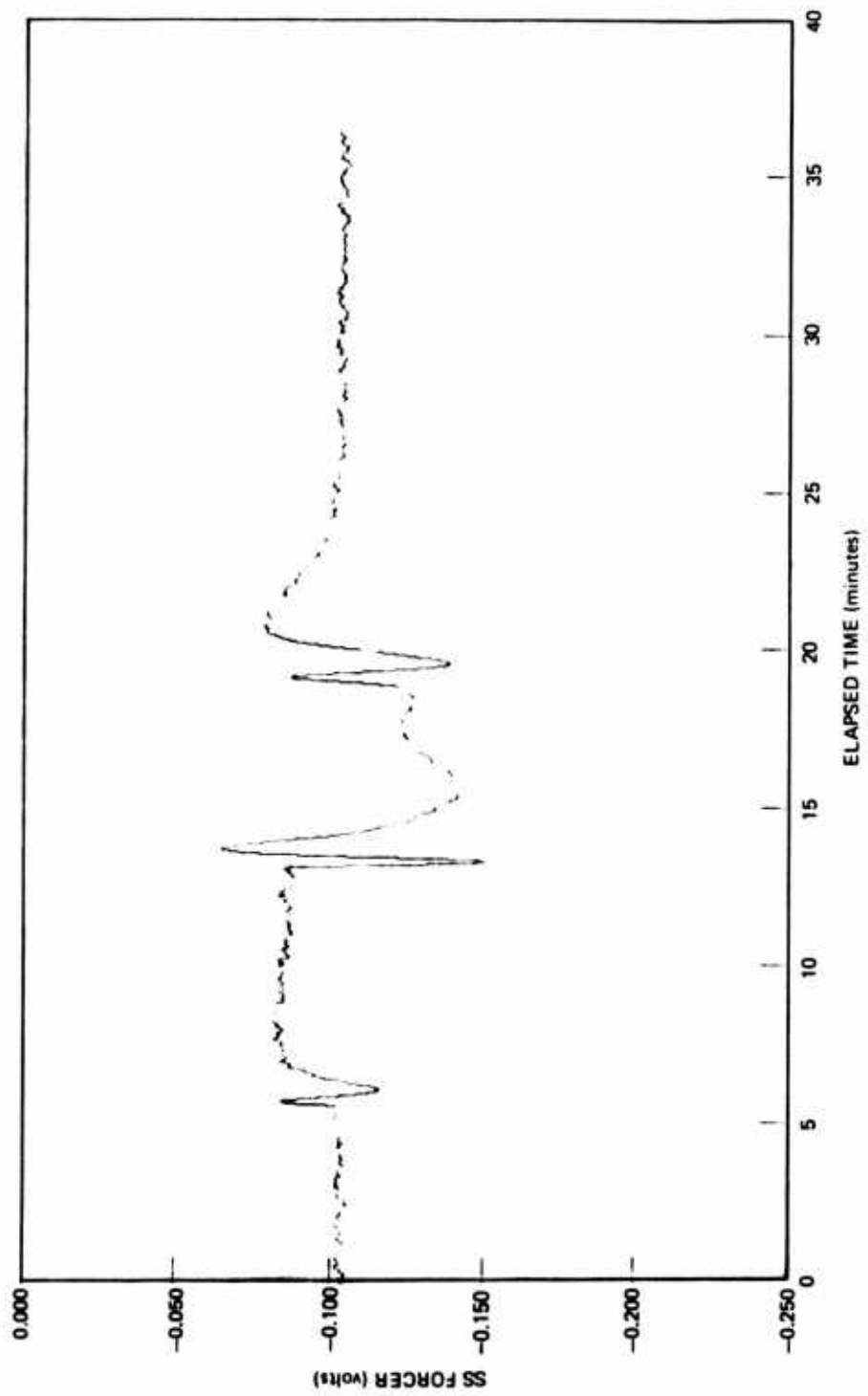


Figure 2-63. SS forcer temperature reaction (SA horizontal) (12/13/76).

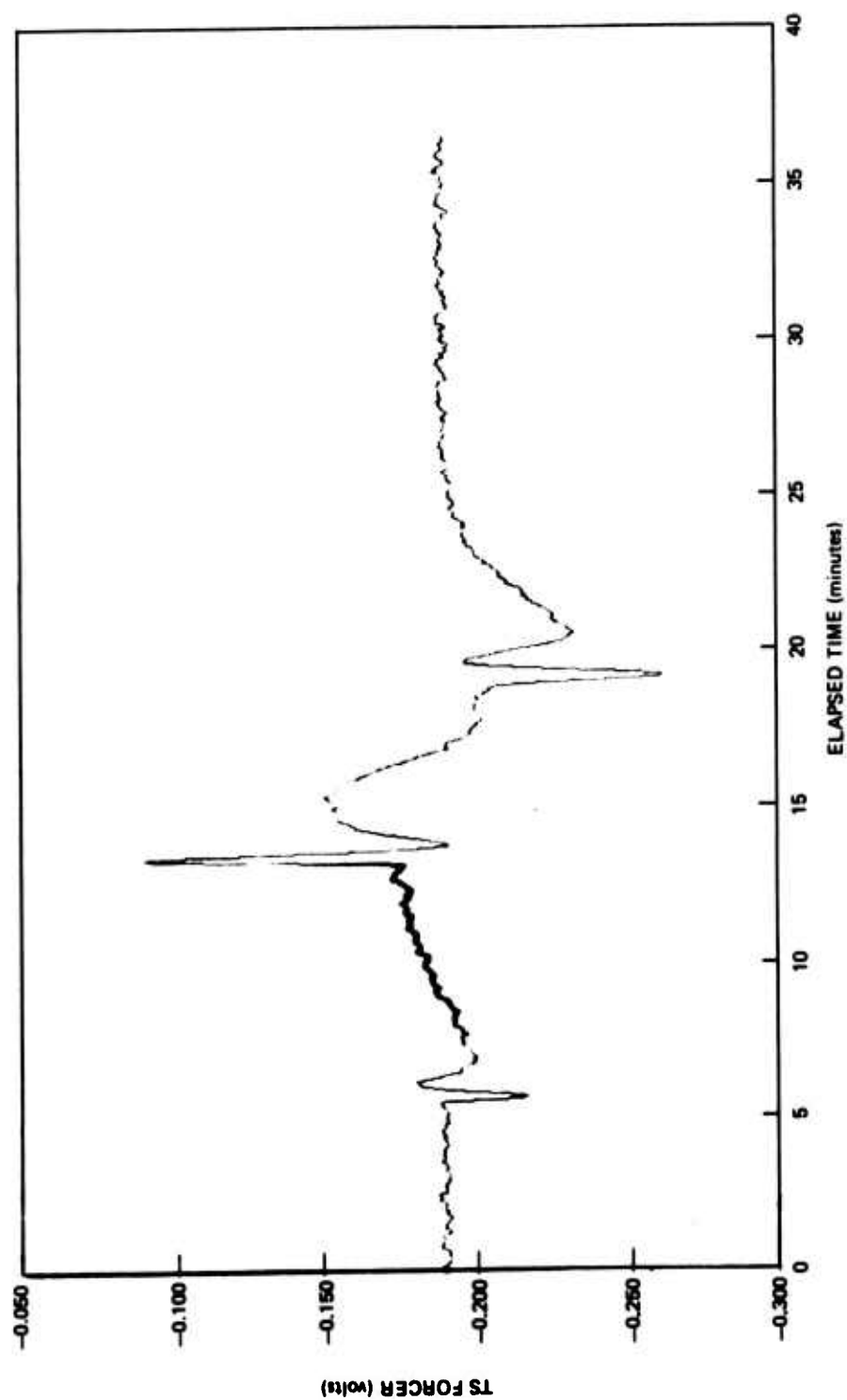


Figure 2-64. TS forcer temperature reaction (SA horizontal) (12/13/76).

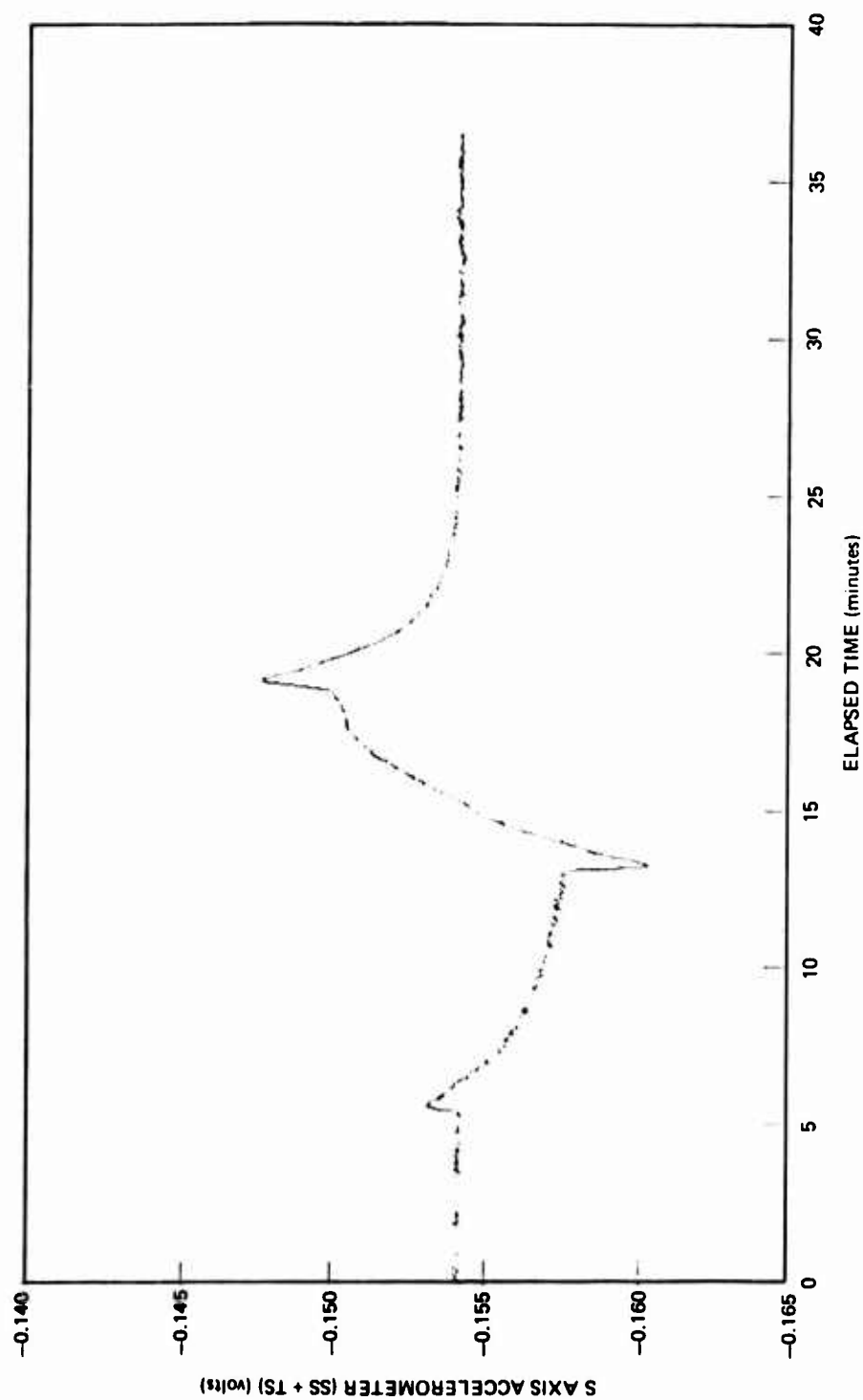


Figure 2-65. S-Axis acceleration temperature reaction (SA horizontal) (12/13/76).

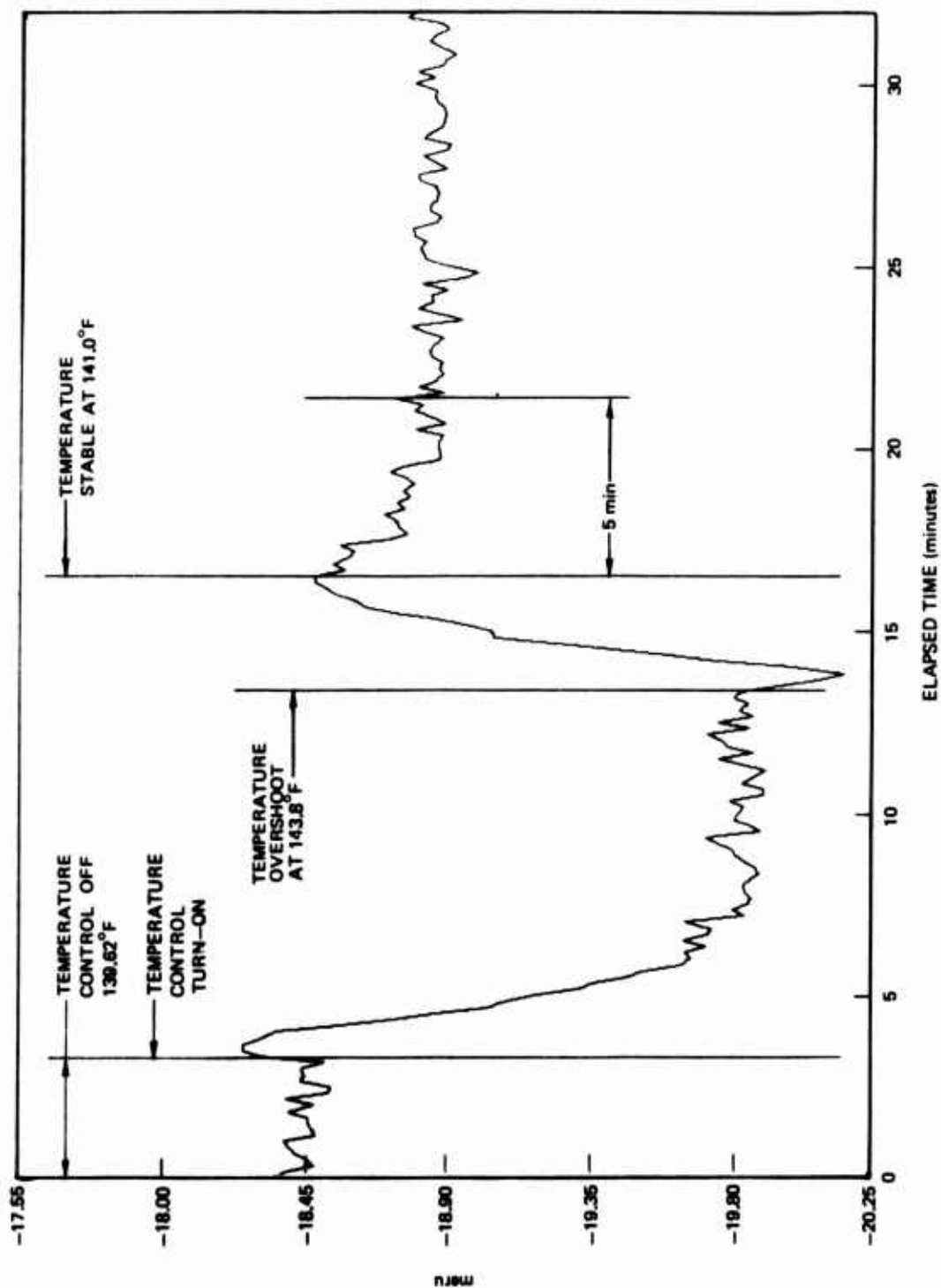


Figure 2-66. Gyro torque during temperature warm-up (IA down | EA) (11/4/76).

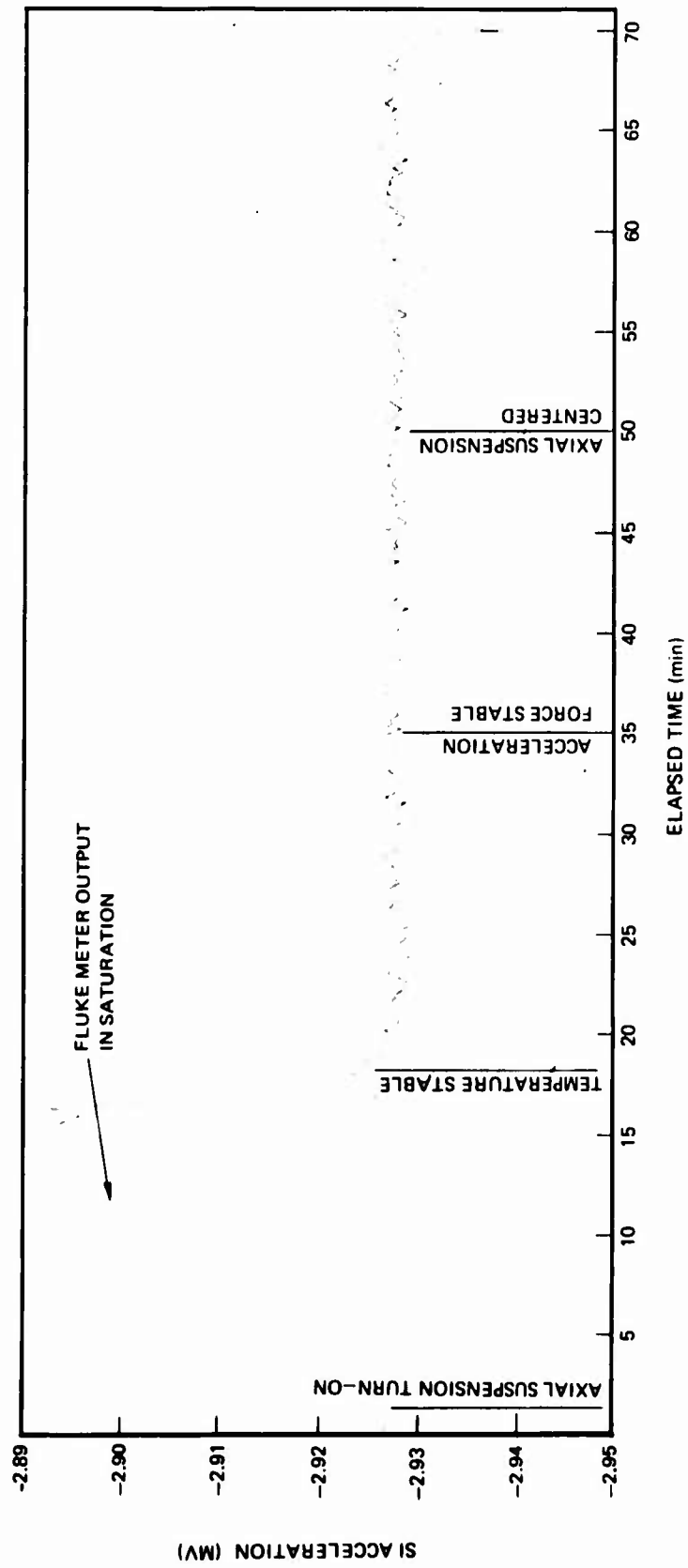


Figure 2-67. I-Axis acceleration, SG end forcer (SI) output during axial position.

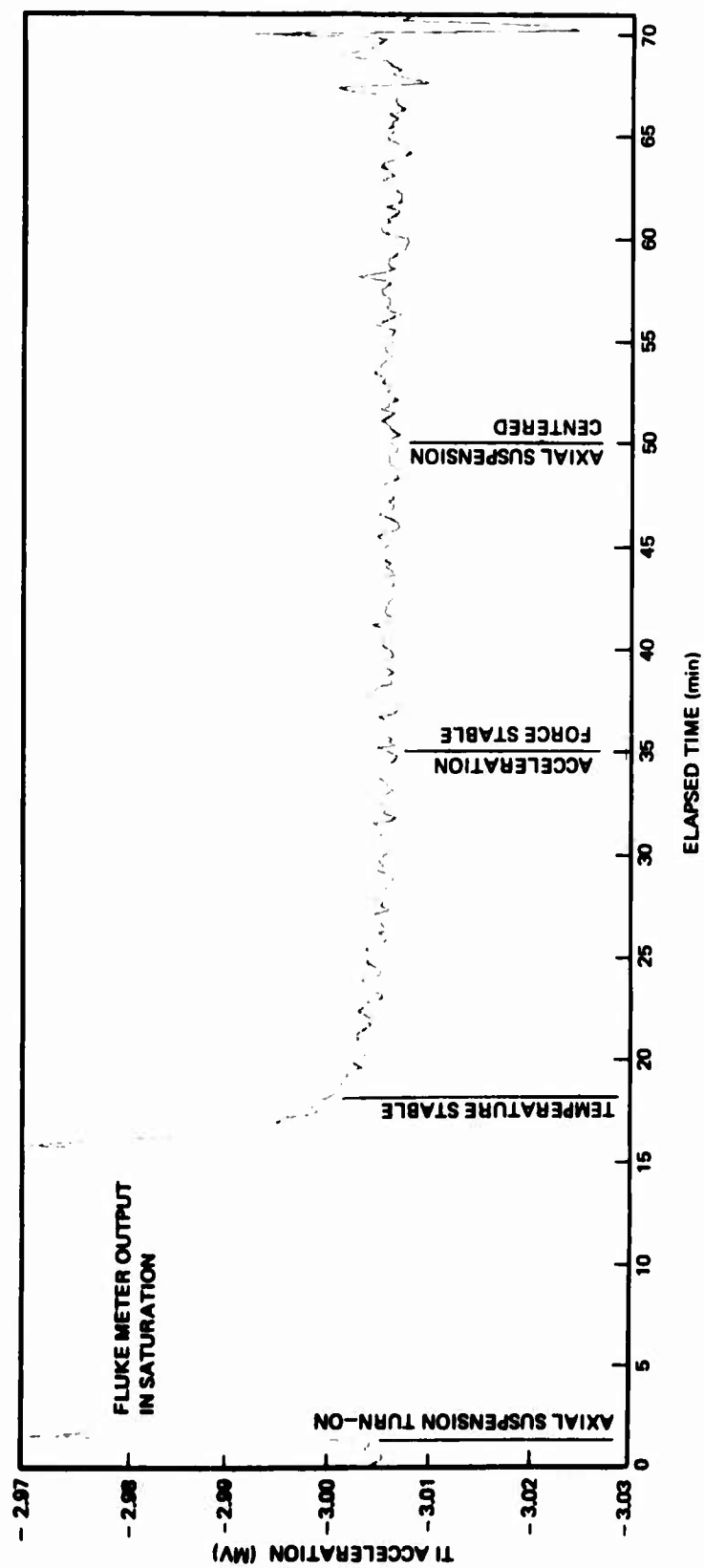


Figure 2-68. I-Axis acceleration, TG end forcer (TI) output during axial pull-in.

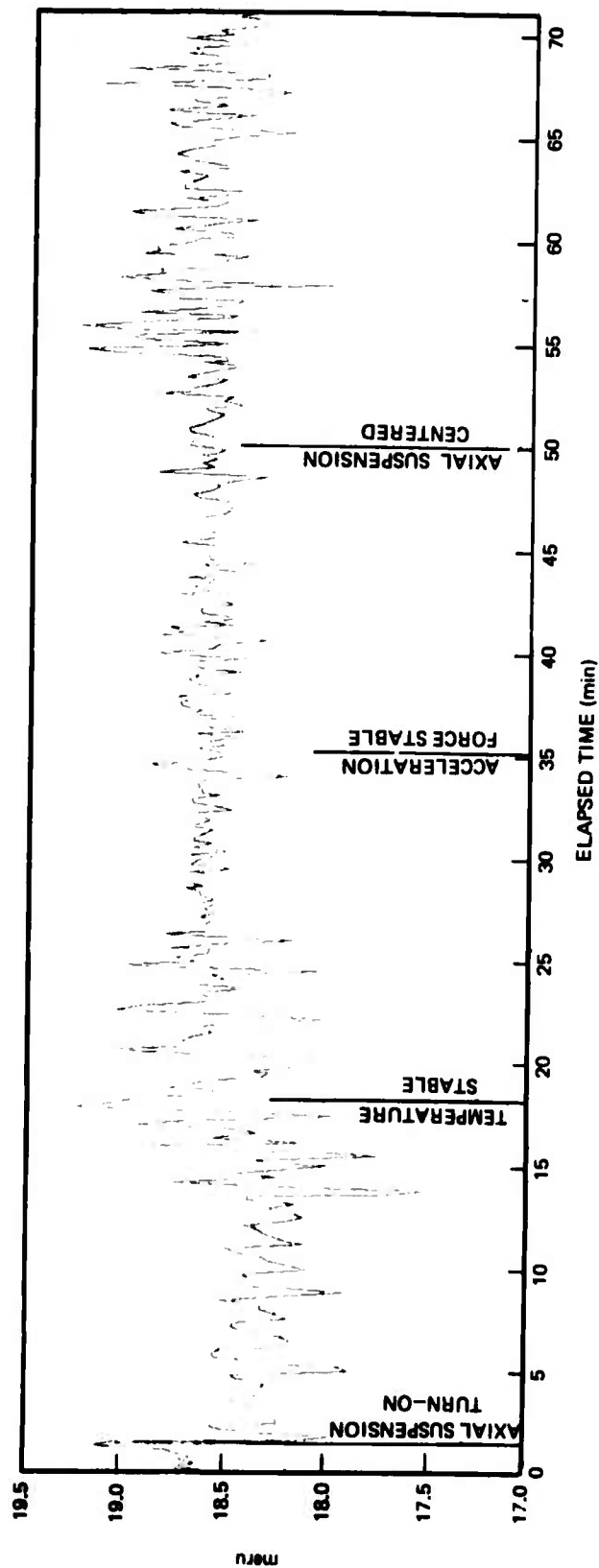


Figure 2-69. Gyro torque during axial pull-in.

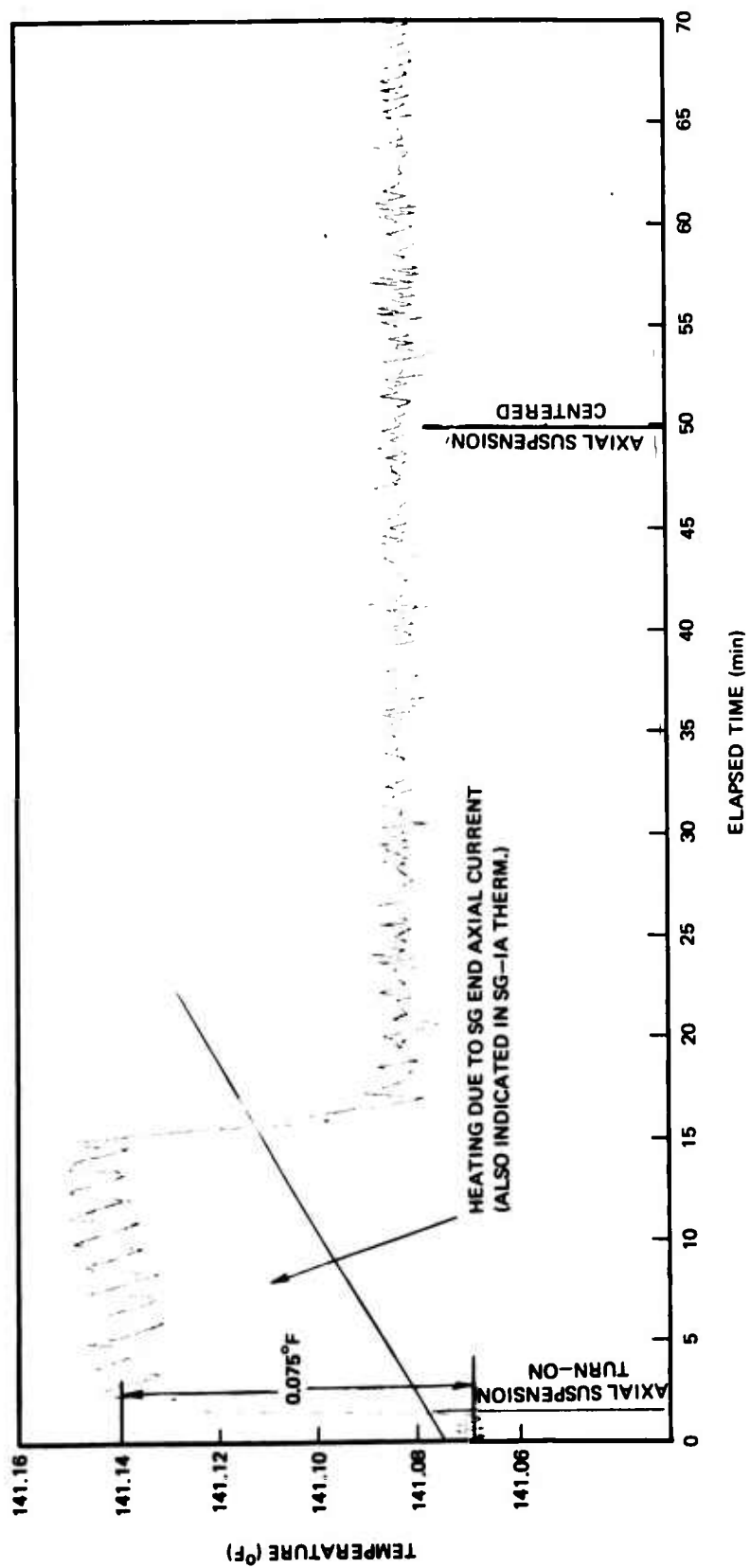


Figure 2-70. SG end housing temperature during axial pull-in.

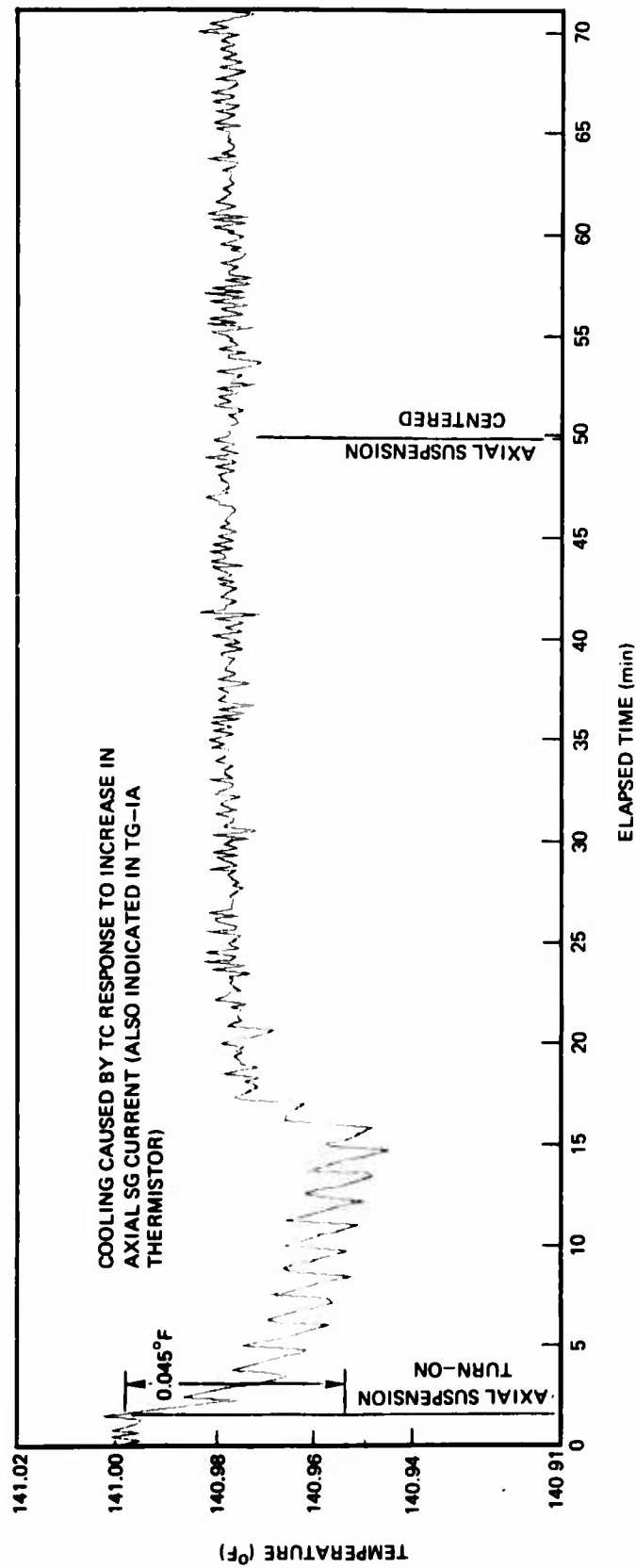


Figure 2-71. TG end housing temperature during axial pull-in.

SECTION 3

DESIGN CONSIDERATIONS

3.1 GENERAL

To complement the description of the test program, design considerations unique to the multisensor are introduced. These observations dictate the design of Section 4 from test and analysis. The following areas have been identified as design topics which are particularly pertinent to the multisensor or other multifunction devices:

- (1) Equations of motion. The motion equations are introduced in a form suitable for multisensor application. The equations introduce topics which are discussed in additional detail throughout this chapter.
- (2) Magnetic interactions between axes and location of axes.
- (3) Thermally induced error.
- (4) Accelerometer errors introduced by wheel anisoelasticity and hunt.
- (5) Accelerometer resolution considering forcer elastic restraint and signal generator noise and null shift.
- (6) Reaction torques caused by axial suspension.
- (7) Adjustment of damping constants - the interaction between input- and output-axis loops coupled through wheel angular momentum.
- (8) Control of rotational and translational modes.
- (9) Case rates of 300 deg/s.

3.2 EQUATIONS OF MOTION

The equations of motion with underlying assumptions are derived in Appendix A and are repeated here for convenience. The motion equations for translational motion are:

$$m\ddot{x}_S + C_T\dot{x}_S = (B-M)a_S + F_{sus}(S) + F_{add}(S) \quad (3-1)$$

$$m\ddot{x}_I + C_T\dot{x}_I = (B-M)a_I + F_{sus}(I) + F_{add}(I) \quad (3-2)$$

$$m\ddot{x}_O + C_{AX}\dot{x}_O = (B-M)a_O + F_{sus}(O) + F_{add}(O) \quad (3-3)$$

For rotation, the equations of motion are:

$$I_S\ddot{\theta}_S + C_R\dot{\theta}_S = a_I^P - a_O U_I + M_{sus}(S) + M_{g^2}(S) + M_{add}(S) \\ + M_{buoy}(S) - H - I_S\dot{\omega}_S + (I_I - I_O)(\omega_I + \dot{\theta}_I)(\omega_O + \dot{\theta}_O) \quad (3-4)$$

$$I_I\ddot{\theta}_I + C_R\dot{\theta}_I + H\dot{\theta}_O = -a_S^P + a_O U_S + M_{sus}(I) + M_{g^2}(I) + M_{add}(I) \\ + M_{buoy}(I) - H\omega_O - I_I\dot{\omega}_I + (I_S - I_O)(\omega_S + \dot{\theta}_S)(\omega_O + \dot{\theta}_O) \quad (3-5)$$

$$I_O\ddot{\theta}_O + C_O\dot{\theta}_O - H\dot{\theta}_I = a_S U_I - a_I U_S + M_{sus}(O) - M_{g^2}(O) + M_{add}(O) \\ + M_{buoy}(O) + H\dot{\omega}_I - I_O\dot{\omega}_O + (I_S - I_I)(\omega_S + \dot{\theta}_S)(\omega_I + \dot{\theta}_I) \quad (3-6)$$

where the subscripts S, I, and O refer to the spin, input and output axes respectively and the superscript dot (·) implies differentiation with respect to time.

- θ = float angular position measured with respect to use
- ω = angular rate inputs applied to instrument case
- a = acceleration input applied to instrument case
- B = float volume times fluid density which is temperature dependent
- C_{AX} = damping constant along output axis
- C_O = damping constant about output axis
- C_R = damping constant about radial axis
- C_T = damping constant along radial axis

| | | |
|------------|---|--|
| F_{add} | = | translational forces which are not accounted in other terms |
| F_{sus} | = | forces exerted by magnetic suspensions |
| H | = | wheel angular momentum where the spin velocity is measured with respect to the float |
| I | = | float moments of inertia including wheel |
| m | = | mass of float including wheel |
| M_{add} | = | torques which are not included in other terms |
| M_{buoy} | = | convection torques which are function of temperature distribution. Since these torques are acceleration sensitive, they can be included in pendulosity and unbalance terms |
| M_{g^2} | = | torques sensitive to acceleration squared |
| P | = | pendulosity along output axis |
| M_{sus} | = | torques exerted by the magnetic suspensions and torquers |
| U | = | mass unbalance |
| X | = | translational position of the nominal float center with respect to the case |

Many terms in the above equations are discussed in other portions of this chapter and in the appendices; however several comments are offered. As in single-degree-of-freedom devices the output axis is primarily driven by $H \omega_I$ the product of the wheel momentum and the case rate about the input axis. Because of the symmetry of the motion equations, the torque about the input axis includes $H \omega_O$, the case rate about the output axis. The torques about the input and spin axes contain terms which multiply the pendulosity along the output axis by the accelerations along the spin and input axes respectively. The pendulosity which is the moment generated by the noncoincidence of the float's centers of gravity and buoyancy drives the accelerometers. Thus, before cross-couplings are included (paragraph 3.3), the following observations are offered.

- (1) The output axis maintains the gyro function;
- (2) The spin axis functions as an accelerometer;
- (3) The input axis contains both accelerometer and gyro information.

Although three information channels are available, the input-axis channel contains both accelerometer and gyro information so that information from another sensor is required to separate the information. The system designer has the option of using three multisensors to obtain the six measurements typically used in navigation and will then have three extra channels containing redundant information. With six variables and six channels of information, theoretically, two multisensors can mechanize an entire platform.

The rotational motion equation about the input and output axes are coupled through $H\omega$ terms. This coupling is discussed in Section 3.8 and in Appendix C and will be exploited in the designs of Section 4. The spin axis equation is essentially uncoupled from the other rotational axes. Implementation of the magnetic suspensions will couple the translational motion along the spin axes and the rotation about the input axis and for translational along input and rotation about spin, a phenomena which is discussed in Section 3.9 and Appendix B. Coupling introduced by misalignments and magnetic coupling are studied in Section 3.3. Terms which include angular rate products will be important for strapdown applications and are discussed in Section 3.10.

3.3 MAGNETIC INTERACTIONS AND LOCATION OF AXES

The previously derived equations of motion assumed that the reference axes were aligned with the physical spin, input, and output axes of the float. This section introduces the consequences of reference axes, misalignment, and cross-couplings of magnetic suspension and torques. These phenomena determine the actual axes' location with respect to the reference axes and determine the compensation required for navigation.

The reference axes are lines scribed on the instrument's case; float axes are defined as the physical axes of the float. Without arguing about the input and output axes, the float spin axis would be the line about which the wheel spins. As derived in Appendix F, the instrument's physical axes are defined by the position of the float physical axes and by magnetic misalignments and cross-couplings, mass unbalance, convection torques, and buoyant forces.

To successfully navigate, the actual, not ideal, content of a torque channel must be determined. Even with perfect components assumed the instrument axes would be misaligned with the navigation coordinates because of machining tolerance inherent in manufacture; thus, compensation

would be required. For the ensuing discussion the case axes are assumed aligned with the navigation axes.

In Appendix F, a static analysis of the multisensor is conducted where the float axes are assumed misaligned with respect to the case reference axes and linear magnetic misalignments and/or cross-couplings are modeled. The resulting signals which would be fed into the navigation computer are summarized in Equations (F-14) and (F-15). These results are used to model the axes location tests described in Section 2. For earth rate testing, the product or rate terms may be neglected.

Based on physical arguments leading to (F-14) and (F-15), the performance equation for the reference gyro output axes may be written as

$$\begin{aligned}
 W_{IND} = & W_I \omega_I + W_O \omega_O + W_S \omega_S + D_F + D_O a_O + D_I a_I + D_S a_S + D_{II} a_I^2 \\
 & + D_{OO} a_O^2 + D_{SS} a_S^2 + D_{IO} a_I a_O + D_{IS} a_I a_S + D_{OS} a_O a_S
 \end{aligned}
 \tag{3-7}$$

where:

D_F is a term insensitive to acceleration or rate (bias)

D_I, D_S, D_O are coefficients of acceleration sensitive terms

$D_{OO}, D_{II}, D_{SS}, D_{IO}, D_{IS}, D_{OS}$ are coefficients of terms sensitive to acceleration squared

W_I, W_O, W_S are terms proportional to case rates

a indicates acceleration

W_{IND} indicates angular rate

ω indicates rate along reference axes

The subscripts S, I, and O indicate vectors along the spin, input, and output case reference axes.

The acceleration terms are called cross-coupling. Ideally, only the coefficient W_I should be nonzero; however, the coefficients W_S and W_O can be called misalignment or cross-coupling. Assuming the W_S/W_I and W_O/W_I are much less than one, rotate the reference axes $-W_O/W_I$ about the spin axis and $-W_S/W_I$ about the input axis; thus, the input axis will be defined in the new coordinates so that only rates about the new input axis are sensed.

Similar expressions result for the other channels where an accelerometer can be defined as aligned when the linear cross-acceleration terms are zero. Since the reference axes can only be rotated about three axes, and alignment of each of the three axes requires two rotations, all the axes cannot be aligned and a residual cross-coupling will result. The problem is completely analogous to aligning individual components to navigation axes.

Since traditional components are usually misaligned with respect to the navigation axes, the compensation requirements of a system comprised of multisensors is not significantly different from that of a system built of other components.

Magnetic interactions such as those occurring in the feasibility multisensor cannot be distinguished from a magnetic misalignment. Because the gyro torquer is mounted on the magnetic structure shared with the radial transducer, case rates about the input axis cause a shift in the radial null. Because of elastic restraint a force will be read on the accelerometer channels. Thus the relation between case rate and radial torque appears as a cross-coupling coefficient.

3.4 THERMALLY INDUCED ERRORS

The acceleration measurement of the multisensor is the torque required to balance the couple established by the float's centers of gravity and buoyancy, a fact which is developed in Appendix A and in Appendix F. If the magnitude or position of the equivalent buoyant force changes, erroneous acceleration readings ensue.

As detailed in Appendix E, a temperature gradient along the output axis can cause the location of the buoyant force to change while the magnitude remains constant. Because fluid motion and shear torques accompany this effect, the term convection torque is also used. The analysis of Appendix E predicts a torque sensitivity of 4 dyn-cm/g⁰F (change from end to end along the output axis). With pendulosity of 0.8 gm-cm, the scale factor sensitivity is 5000 ppm/⁰F.

If the temperature level changes uniformly, the magnitude of the buoyancy coefficient will change because of the flotation fluid's sensitivity to temperature. The change in flotation force is balanced by the radial suspensions which are aligned with the gravity vector. If torques are summed about the point through which the buoyant force acts, no change is read in the torque. This cancellation is equivalent

to selecting the weighting between current readings from the two suspensions so that

$$k = q_{34}/q_{44}$$

in (F-14). Because the buoyancy is typically very sensitive to temperature (400 ppm/ $^{\circ}$ F for the feasibility instrument), removal of the buoyancy level change from the torque summation is desired.

The multisensor feasibility instrument was designed symmetrically from end to end so that temperature gradients would be minimized. A temperature control stabilized level changes and the current readings from the suspensions at either end of an axis were tuned to eliminate the buoyancy level effects on the torque.

Assuming temperature gradient controlled to 0.01 $^{\circ}$ F, a scale factor change of 50-100 ppm is expected. With a float mass of 140 gm, a fluid density sensitivity of 400 ppm/ $^{\circ}$ F, 0.8 gm-cm pendulosity, 5.6 cm between suspensions, temperature level change of 0.01 $^{\circ}$ F, and the scaling between ends correct to 3 percent, the scale factor changes 57 ppm. These values are approximately consistent with those seen in the testing. However, uncertainties in null position could contribute to scale factor error as discussed in paragraph 3.6. Because of the large torque capability required for 300 $^{\circ}$ /s slewing and because of the excellent gyro performance obtained, better scale factor performance can be obtained by increasing the pendulosity.

3.5 ACCELEROMETER ERRORS INTRODUCED BY WHEEL ANISOELASTICITY AND WHEEL HUNT

The rotational equations of motion (3-4) through (3-6) contain torques which are sensitive to acceleration products. These terms reflect compliance of the float structure and the wheel bearings. The acceleration products are presently compensated in single-degree-of-freedom gyros, in pendulous accelerometers and in specific force integrating receivers; thus, these terms were only considered in the axes location tests. With proper compensation, the acceleration products should have only small effect on multisensor performance.

The motion about the spin axis depends on the wheel's hunting, the \dot{H} term in (3-4). The magnitude of \dot{H} may be estimated by observing the ripple on the wheel power. Typical numbers for multisensor feasibility size instruments with hysteresis motors are 10 milliwatts ripple, peak-to-peak at a frequency of 10 Hz. With a wheel speed of 48,000 r/min (the feasibility instrument's speed), the rms torque ripple is 7 dyn-cm rms at 10 Hz. With 800 gm-cm pendulosity, the rms velocity

error, 0.14 cm/s, is less than the velocity accuracy of 0.7 cm/s required for a 50 ppm system as estimated in Appendix D.

3.6 ACCELEROMETER RESOLUTION CONSIDERING FORCER ELASTIC RESTRAINT AND SIGNAL GENERATOR NOISE AND NULL SHIFT

Based on experimental observations and the analysis discussed in Appendix D, the effects of the accelerometer's elastic restraint and the accelerometer signal generator's noise upon the rebalance force is discussed.

Elastic restraint is defined as the partial deviation of the suspension's force with respect to displacement. An ideal radial suspension forcer would exert a force which depends only on current; however, normal forcers also depend on radial position. Elastic restraint must be considered in multisensor design for the following reasons:

- (1) Destabilizing influence on control loops;
- (2) Velocity error for acceleration step change; and
- (3) Erroneous force reading with accelerometer signal generator null shift.

The feasibility instrument forcer primary currents are fixed amplitude square waves whose measured elastic restraint was 3×10^4 dyn-cm per end. With proper tuning of the signal generator as a passive suspension, the elastic restraint can be reduced to 1 percent of the value obtained from the forcer alone. The 1 percent figure is conservatively based on 0.001 cm displacement during calibration and ability to discern torques of 0.08 dyn-cm.

For typical damping constants and loop gains the controller gains are sufficiently greater than the elastic restraint so that stability and pole placement are not affected even if the SG is not compensated. The elastic restraint affects numerator dynamics and is discussed under velocity error and signal generator null shift.

For a step change in acceleration, the steady-state velocity error is proportional to the effective elastic restraint. With compensation, the steady velocity error for a one gravity step change is 0.006 cm/s compared to the 0.7 cm/s commensurate to 50 ppm navigation (see Appendix D). Thus, with compensation, elastic restraint is insignificant and without compensation, borderline.

If the signal generator's null shifts, the float's will be positioned so that the SG output is zero. With elastic restraint, the position change will cause the current to change so that the force on the float remains unchanged. This current change will be interpreted as a bias error. If the null shift occurs during calibration, it can also affect the scale factor determination.

With series parallel connection used in the feasibility device's signal generator, the null is directly proportional to the difference in the capacitance of the parallel legs. As calculated in Appendix D, capacitance stability of the order of 25 ppm or one picofarad is required for the bias stability of 100 μ g in the feasibility instrument which was not accurately tuned. If the capacitors shift equally, the null and the force reading are unaffected.

The capacitors used in the feasibility device had a temperature sensitivity of approximately 200 ppm/ $^{\circ}$ F and the wires from float to capacitors were strapped to minimize capacitance changes. Despite the multisensor's satisfying the bias stability requirement, the rotation during the tests could affect the capacitance temperatures and appear in the scale factor stability since one assumes that scale factor and bias do not change during the two point test.

The null's sensitivity to capacitance can be almost eliminated by connecting the signal generator windings in a bridge with capacitor across the bridge for tuning. Since null is determined by the voltage across the capacitor, capacitance shifts affect null position only slightly (depending on the asymmetry of the windings). Signal generator tuning to eliminate elastic restraint and better suspension capacitors (20 ppm/ $^{\circ}$ F can be obtained) should be evaluated before additional end housing taps required for bridging are inserted into the multisensor design.

In the previous single-degree-of-freedom devices, measurements were taken about the output or symmetric axis where the damping constant is typically 2×10^5 dyn-cm-s. Damping constants about transverse axes are three to four orders of magnitude higher because of film squeeze. For a given bandwidth, the electronic gain is proportional to the damping as detailed in Appendix D; thus, small amounts of pure signal generator noise result in significant rebalance torque errors. Pure signal generator noise is defined as not originating in actual motion of the float. Possible sources of pure signal generator noise are Barkhausen noise in the magnetic materials and preamplifier noise at the carrier frequency.

If the signal generator's null shifts, the float's will be positioned so that the SG output is zero. With elastic restraint, the position change will cause the current to change so that the force on the float remains unchanged. This current change will be interpreted as a bias error. If the null shift occurs during calibration, it can also affect the scale factor determination.

With series parallel connection used in the feasibility device's signal generator, the null is directly proportional to the difference in the capacitance of the parallel legs. As calculated in Appendix D, capacitance stability of the order of 25 ppm or one picofarad is required for the bias stability of 100 μ g in the feasibility instrument which was not accurately tuned. If the capacitors shift equally, the null and the force reading are unaffected.

The capacitors used in the feasibility device had a temperature sensitivity of approximately 200 ppm/ $^{\circ}$ F and the wires from float to capacitors were strapped to minimize capacitance changes. Despite the multisensor's satisfying the bias stability requirement, the rotation during the tests could affect the capacitance temperatures and appear in the scale factor stability since one assumes that scale factor and bias do not change during the two point test.

The null's sensitivity to capacitance can be almost eliminated by connecting the signal generator windings in a bridge with capacitor across the bridge for tuning. Since null is determined by the voltage across the capacitor, capacitance shifts affect null position only slightly (depending on the asymmetry of the windings). Signal generator tuning to eliminate elastic restraint and better suspension capacitors (20 ppm/ $^{\circ}$ F can be obtained) should be evaluated before additional end housing taps required for bridging are inserted into the multisensor design.

In the previous single-degree-of-freedom devices, measurements were taken about the output or symmetric axis where the damping constant is typically 2×10^5 dyn-cm-s. Damping constants about transverse axes are three to four orders of magnitude higher because of film squeeze. For a given bandwidth, the electronic gain is proportional to the damping as detailed in Appendix D; thus, small amounts of pure signal generator noise result in significant rebalance torque errors. Pure signal generator noise is defined as not originating in actual motion of the float. Possible sources of pure signal generator noise are Barkhausen noise in the magnetic materials and preamplifier noise at the carrier frequency.

An alternate viewpoint argues that for a given loop bandwidth increasing damping decreases the displacement for a given input so that eventually the actual motions which determine the forces are lost in the signal generator noise.

For 50 ppm navigation which implies a velocity error-of-error of 0.7 cm/sec and to expedite calibration so that filtering and excessive sampling (10,000) points are not required, a damping constant less than 10^7 dyn-cm-s is required.

3.7 REACTION TORQUES CAUSED BY AXIAL SUSPENSION

Previous multisensor testing demonstrated a large reaction torque in the transverse channels caused by the axial suspensions. With passive suspensions a quiescent force is exerted at each end which oppose one another. With machining tolerances, these forces are not colinear so that a couple exists about a transverse axis. The multisensor was wired with active time shared axial suspensions so that the quiescent forces with perfect flotation would be zero, and hence, the reaction torques would be reduced.

3.8 ADJUSTMENTS OF DAMPING CONSTANTS—INTERACTION BETWEEN INPUT AND OUTPUT AXES COUPLED THROUGH ANGULAR MOMENTUM

The multisensor's three dimensional damping characteristics should be altered for several reasons. As discussed in Section 3.7, damping about the transverse axes must be reduced to decrease noise in the torque rebalance signal caused by signal generator uncertainty. A decrease in radial and axial damping constants would decrease reaction time because of more rapid transients. Lower fluid viscosity facilitates filling and reduces contamination and density gradient problems.

In reducing fluid viscosity and damping constants, the following effects must be considered:

- (1) Time constants for single axes; and
- (2) Two-degrees-of-freedom motion coupled through wheel angular momentum.

For this discussion, a single-degree-of-freedom gyroscope (or, alternatively, a gyro which obeys single-axis theory) may be controlled by designing the torques about the output axis as a dynamic function of

the float rotation about the output axis. Similarly, the input axis control torques are functions of the float-case angle about the input axis.

When reducing damping, single axis effects such as the time constants determined by the damping constant divided by the moment of inertia and the permissible float motions must be considered. Since the design proposed here will result in time constants equivalent to those presently used, this topic will not be pursued.

When altering damping constants, the interaction of input and output axis loops which are coupled through the wheel momentum must be considered. With active suspensions whose bandwidths are comparable to those of multisensor applications, the single axis theory is valid (the poles of the coupled system approximate those developed from single-axis theory) when the product of the damping constants about the input (C_I) and output (C_O) axis is greater than 100 times the angular momentum (H) squared. For lower damping products, suitable control requires that the torque about the output and input axes be functions of both the input and output angles.

For many practical designs and bandwidths, Appendix C demonstrates that inertia terms may be negligible even with low damping. Thus, the motion equations (C-3) and (C-4) for the input axis are virtually identical with that of the output axis. The form of the two equations is identical except that the coefficients of the float-case angles are defined by different quantities.

For present Draper designs,

$$C_I C_O > 100 H^2$$

and the torque about the output axis is controlled as a function of the output-axis angle and similarly for the input axis. The similarity of the two equations then dictates that for:

$$H^2 < 100 C_I C_O$$

The torque about the input axis should be a function of the angle about the output axis and similarly the torque about the output axis should be a function of the angle about the input axis. As in the single axis situation, the two equations are effectively decoupled; however, the

dynamics of the individual loops are now dominated by the angular momentum. This situation is identical to that of single-axis theory where the loop response is dominated by the damping constant.

The above observation may be applied directly to multisensor design. Consider the feasibility instrument, fluid viscosity could be selected so that the damping constant about the spin axis is roughly 2×10^5 dyn-cm-s, a figure which allows good loop response and little problem from signal generator noise. The input and output damping product would be less than $H^2/100$. The crossfeedback described in the previous paragraph would stabilize the input and output axis loops with excellent dynamic characteristics. That is, the three rotational loops could be designed with suitable dynamic characteristics.

3.9 CONTROL OF ROTATIONAL AND TRANSLATIONAL MOTIONS

With cylindrical multisensor designs, the radial positions at both ends of the float are measured and radial forces are applied at both ends. Since the radial forcers are multisensor outputs, the implications of forcer connections and control design are discussed.

The radial position signals indicate the displacement of the float's ends with respect to the null position. Because the permitted float-to-case rotations are small, the signals can be summed to yield translation of the float center or differenced to obtain float rotation.

With double wound forcers which are included in the feasibility instrument, the following design options for forcer connections are defined:

- (1) End control (Figure 3-1) where the forces in each end are controlled independently; and
- (2) Mode control (Figure 3-2) where the windings are connected so that ideally forces and torques about the float center may be applied independently.

The mathematical implications of these controls are discussed in Appendix B.

Presently the feasibility multisensor employs end control with the force at a given end controlled by the displacement at that end. This option was selected because of the ease with which the precision pattern field could be obtained.

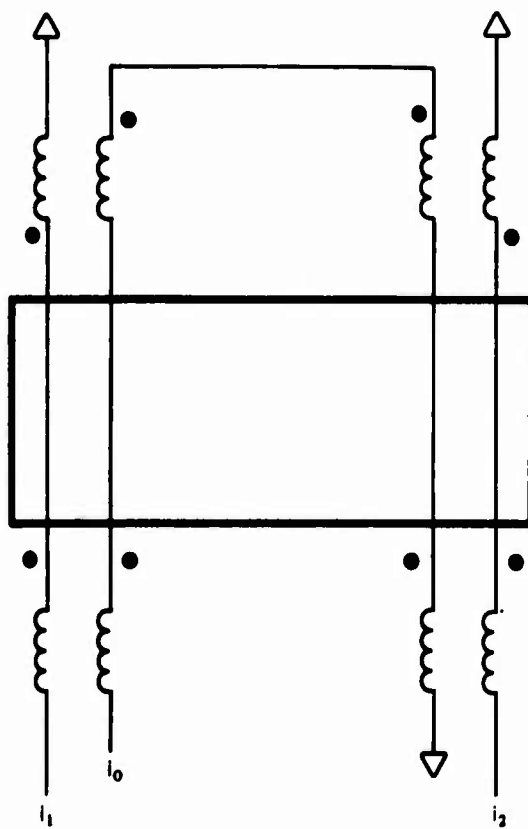


Figure 3-1. Schematic of radial forcer connections, individual end control.

The dynamic compensators which related position to current (hence, force) were selected to obtain the desired rotational response while accepting an underdamped, more slowly decaying, translational signature as discussed in Appendix B. The slower mode did not hamper the feasibility instrument's performance; however, independent loop tuning can be obtained by crossfeedback, where the displacement at the opposite end is also used to control the force. Crossfeedback can be used to electronically decouple the modes as discussed in Appendix B.

The common mode rejection of the translational motion (which is undesirable because of its strong temperature dependence as discussed in paragraph 3.4) was accomplished in calculations external to the control loops. Because of the uncertainty in establishing the scale factors of the two forcings (Appendix F and Section 2), probably only 95 - 97 percent of the common mode was rejected.

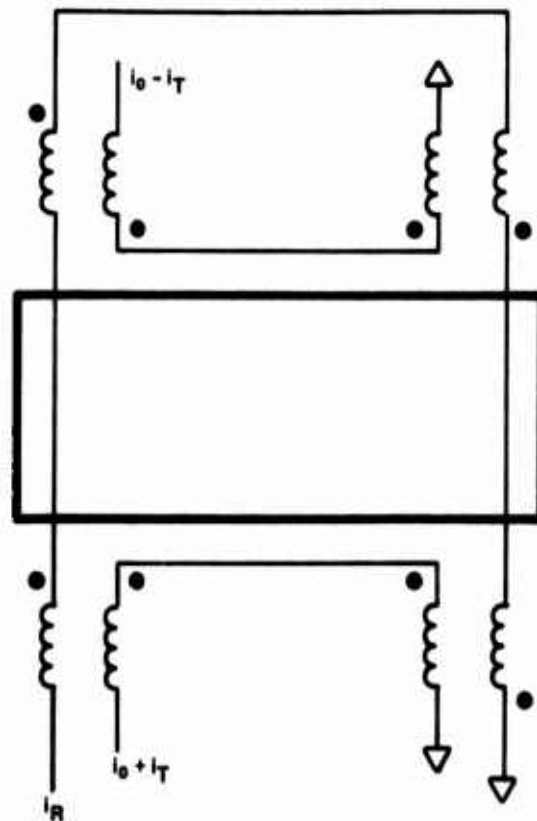


Figure 3-2. Schematic of radial forcer connection, separate rotational and translational mode control.

The mode control permits the common mode to be rejected mechanically. Because of forcer and instrument dissimilarity, the rejection would probably be 97 percent successful. But the rotational torque could be trimmed by adding a small portion of the translational force so that mode control promises common-mode rejection greater than 99 percent.

The separation of the modes is required to implement the lightly damped mechanization described in the previous section. Once the rotational torques are separated from the forces, the connections can be arranged to permit single-degree or lightly damped operation.

3.10 MAXIMUM CASE RATES

The work statement specifies that case rates of 300 deg/s (or 5 rad/s) should be considered. In determining maximum permissible case rate, the following factors must be considered:

- (1) At steady-state is sufficient torque available about both the input and output axes to rebalance the momentum-case rate product;
- (2) Provided sufficient torque is available, can the damping and loop bandwidth be tuned so that the float does not hit the stops during a transient; and
- (3) Will terms such as the inertia difference times the product of case rates require compensation in navigation.

Appendices B, C, or D may be extrapolated to demonstrate that the float can be restrained from case contact with the proposed integral control loops. Assume a change from 0 to 5 rad/s can be represented by a ramp of 1 rad/s/s. From (D-4), for the 22 Hz bandwidth, tuning with angular momentum equal loop damping, the displacement is 600 μ in. However, the problem of resolving meru with maximum rates of 1 rad/s must be resolved (see Section 4).

For strapdown application, compensation for the cross-product terms will be required. An angular momentum of 20,000 dyn-cm corresponds to 0.0015 dyn-cm. The difference between moments of inertia about spin (approximately equal input) and output axis is roughly 5 gm-cm for a 10-size device. At a slew of 0.1 rad/s, the inertia difference results in a torque of 0.05 dyn-cm so that compensation is required.

SECTION 4

DESIGN PROJECTION

A preliminary design of a 10-size multisensor (nominal case diameter of one inch) appears in Figure 4-1. Important design parameters are listed in Table 4-1. A brief discussion of the design highlights is included.

The 10-size multisensor is designed with pendulosity of 1 gm-cm, slightly larger than the feasibility instruments. At 10 gravity, the required rebalance torque is 10,000 dyn-cm, a figure within the forcer capability by a factor of four. Since thermally induced errors scale as a characteristic dimension to the fourth power (paragraph 3.4, and Appendix E), a factor of ten improvement in acceleration sensitive stability could be realized.

The 10-size PIG (Pendulous Integrating Gyroscope) has demonstrated torque uncertainties which would give performance better than the one meru design guidelines with either the 5,000 or 10,000 dyn-cm wheel. To reduce compliance torques, hemispherical gas bearing wheels are selected. Although hysteresis motors perform acceptably (paragraph 3.5), further reduction of wheel hunting and more stable thermal environment are products of the permanent magnet wheel motor design depicted in Figure 4-1.

While smaller values of angular momentum could satisfy performance, 5000 were selected so that the gyro axes would operate in the lightly damped mode where

$$C_I C_O < \frac{H^2}{100}$$

In the lightly damped mode all axes could be designed with similar dynamic response as described in paragraph 3.3. The rotational and translational pull-in times are less than 9 seconds so that excellent warm-up characteristics will be achieved. The low viscosity fluid will greatly facilitate fill procedure.



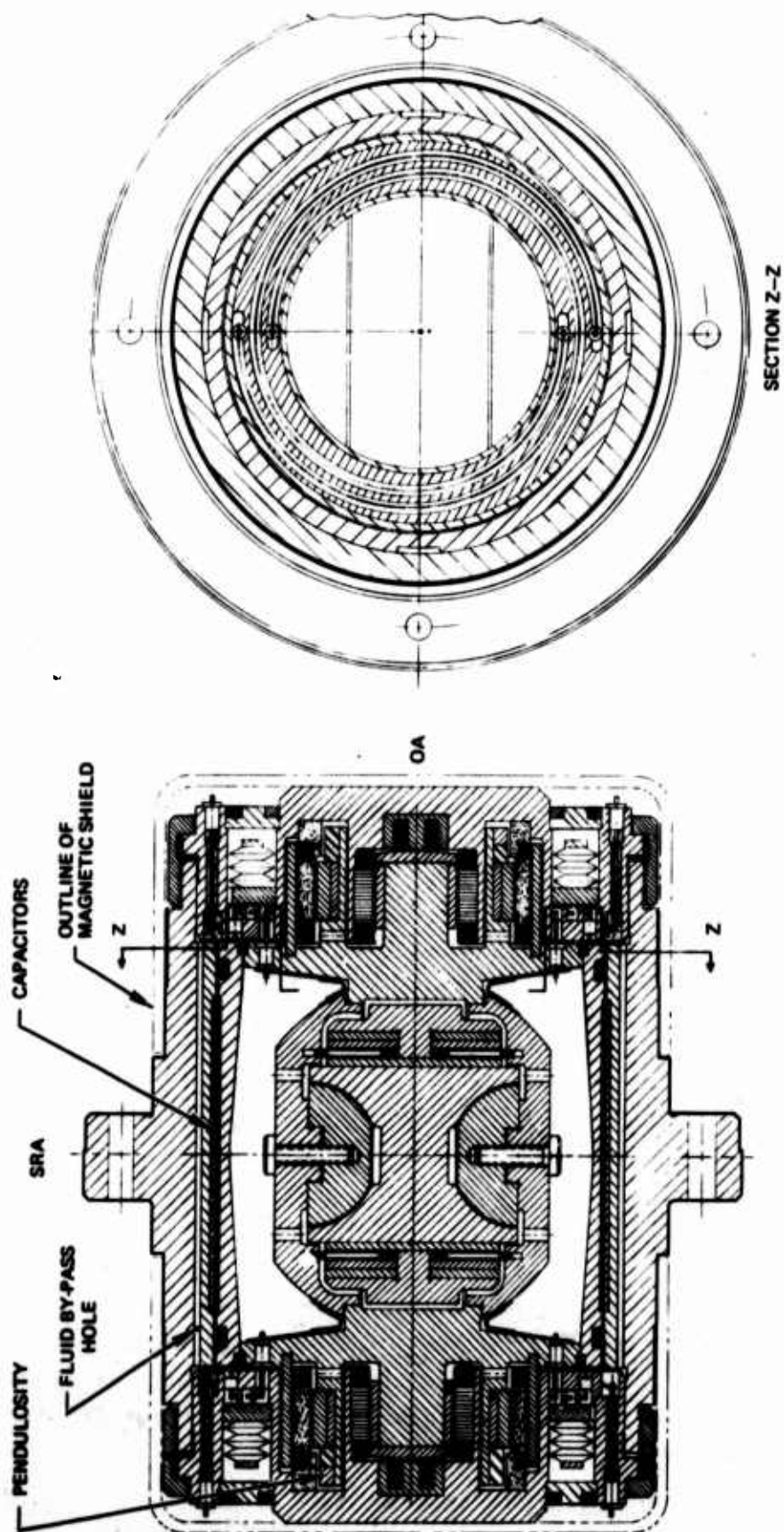


Figure 4-1. Multisensor (low damping - 10 size).

TABLE 4-1. DESIGN PARAMETERS FOR 10-SIZE MULTISENSOR.

| | |
|--------------------------------|--|
| Float Mass | 22 gms |
| Moments of Inertia About S | 20 gm-cm ² |
| Moments of Inertia About I | 20 gm-cm ² |
| Moments of Inertia About O | 15 gm-cm ² |
| Angular Momentum | $5 \times 10^3 - 2 \times 10^4$ dyn-cm |
| Pendulosity | 1 gm-cm |
| Fluid Viscosity μ | 3 cP |
| Damping Constants | |
| Radial Rotation (C_R) | 3×10^4 cP |
| OA Rotation (C_O) | 30 cP |
| Radial Translation (C_T) | 1.5×10^5 cP |
| Axial Translation (C_{AX}) | 1.5×10^5 cP |
| Torque Maximum | |
| Output Axis | 5 - 10,000 dyn-cm |
| Transverse | 4×10^4 dyn-cm |

Axial motion and the inherent coupling with the rotational measurement axis is reduced by the outward facing mass compensated bellows which the feasibility instrument did not possess.

To mechanize the control required for light damping, the forcer windings are double wound and connected in the mode control of paragraph 3.9. As demonstrated in the feasibility instrument, active control will be used to adjust dynamic control and to assure that the float's position with respect to the case remains constant. The radial and axial suspension rotors overlap their respective stators so that cross-coupling between axes is minimized. Because of the lightly-viscous damping fluid, the magnetic suspension clearances can be set

to optimize suspension force and efficiency. With high damping, reduction of the transverse-axis damping resulted in increased suspension clearance and, hence, reduced magnetic efficiency.

With permanent magnet gyro torquer with 5000 dyn-cm capability, case rates of 1 - 2 rad/s could be balanced. Since current readouts can only scan six orders of magnitude and since the ratio of 1 rad/s to 1 meru is 1.4×10^7 , a design trade-off between maximum case rate and resolution must be made. The following options are being considered for generating the radial signals required for control:

- (1) Two permanent magnet torquers about the output axis with capacitive pick-offs in the annulus to generate both radial and output axis signals. This option is shown in Figure 4-1. Because of the instrument's small size, questions over gyro signal resolution must be resolved. Because of their high impedance and the goal of not requiring additional flex leads, the capacitor signal generators require careful design to maintain elastic restraint at acceptable levels for gyro signal generator.
- (2) One permanent magnet, a microsyn signal generator, and capacitor pick-offs for the radial signals. The gyro would be controlled as in present instruments where the microsyn signal generator has proven itself. The capacitors could then be used in their most sensitive normal operation to generate the radial signals.
- (3) Use soft iron torquer and microsyn which double as the radial signal generator as in the feasibility instrument. With the low viscosity fluid, the noise propagation problem which appeared in the feasibility instrument can be avoided. The cross-coupling between forcer axes and gyro torquer can be compensated (the required term will exist in any case) as described in paragraph 3.3. Although the maximum torques generated with soft iron are an order of magnitude less than those of the permanent magnet torquer, present read-out devices can not scan the seven orders of magnitude between 1 rad/s and 1 meru.
- (4) Two microsins and magnetic torquer. The microsins could be used to simultaneously measure angle about the output axis and radial position as done in the present multisensor. To

minimize cross-coupling a separate torquer, either permanent magnet or soft iron, is added. A torquer or signal generator could be added about the instrument's circumference (belly) or added in the end housing areas. These options require further refinement.

SECTION 5

CONCLUSIONS AND RECOMMENDATIONS

5.1 CONCLUSIONS

Based on test results of a feasibility instrument, analyses, and design studies, the multisensor concept is suitable for navigation and should be pursued further.

With an instrument which was neither designed nor optimized as a multisensor, accelerometer stability of 50 μ g bias and 75 ppm scale factor were achieved in two position 100-hour tests. Despite the large (by gyro standards) output axis pendulosity, the gyro exhibited bias stability of 0.1 meru and acceleration sensitive stability of 0.3 meru/g.

Because of high damping about the transverse axes, and uncompensated bellows, transient behavior was not at operational standards; however, the sources of the transients are understood and design alterations have been presented which circumvent the deficiencies (see Section 4). The projected size 10 design will have radial and axial pull-in times less than one second because of the low viscosity fluid which is possible because of the cross-connected input-output axis control. By increasing pendulosity and because of the temperature dependent error's sensitivity to size, the projected design should have accelerometer performance significantly better than the feasibility instrument.

The multisensor program is more significant than a mere demonstration of a multisensor which can simultaneously measure angular rate and acceleration. Most importantly, torque summation about the transverse axis of a cylinder has been demonstrated. With the ability to sum torques about a transverse axis, one can envision an entire family of inexpensive multifunction instruments. From identical hardware with only slight modifications to the float, multisensors, two-degree-of-freedom gyros, two-degree-of-freedom accelerometers, and three-degree-of-freedom angular rate sensors can be built.

5.2 RECOMMENDATIONS

Recommendations for further testing of the present instrument and for design activities are listed.

To demonstrate improved performance, the present feasibility instrument should be tested with the following changes:

- (1) More insight into accelerometer bias could be obtained by replacing the present 200 ppm suspension capacitors with 20 ppm capacitors.
- (2) Accelerometer bias stability improvements from more accurate cancellation of the accelerometer elastic restraint should be investigated.

The feasibility multisensor should be tested in continuous tumble tests. The tumble test will allow the multisensor to be evaluated in a dynamic environment and will investigate the stability of the axes.

The feasibility instrument should be rewired externally to mechanize the mode control of paragraph 3.9. The output axis signal generator will control the output axis torques and similarly for the input axis. Stability and sensitivity tests would then be conducted in order to compare performance with mode control to that with end control.

If mode control is successfully demonstrated, the instrument should be disassembled, cleaned, and refilled with fluid whose viscosity is 3 cP. The control would be rewired so that the output-axis torque is controlled by the float-case angle about the input axis. The lightly damped tests will verify the instrument design projected in Section 4. Particular points to be demonstrated are:

- (1) Fast transients with axial and radial pull-in times of order, one second;
- (2) Stability with lightly viscous damping fluid;
- (3) Similar dynamic performance about the three rotational axes;
- (4) Reduction of noise in accelerometer channels.

In conjunction with the testing described above, design activity is required with particular emphasis on signal generator design and operational requirements. As discussed in Section 4, at least four options are available for generating the output axis angle and radial

displacements necessary to implement active control. The options and trade-offs should be carefully studied to establish a design optimized with respect to performance and cost.

In order to design suitable instruments, the multisensor's system applications should be studied so that the feasibility programs are geared toward the proper operating environment. In particular, maximum slew rates and minimum sensitivity (paragraph 3.10 and Section 4) should be resolved.

While the projected design of Section 4 was based on beryllium technology, design effort should be focused on low-cost multisensors made from molded components.

APPENDIX A

MULTISENSOR EQUATIONS OF MOTION

A.1 SUMMARY

Equations of motion are derived for the multisensor. The float is modeled as a rigid body which has six-degree-of-freedom with respect to the case. The wheel is modeled as a rigid cylinder which spins with respect to the float about its (the wheel's) symmetric axis. While several simplifications and assumptions are made, the characteristics essential for multisensor analysis are retained. Because several of the six-degrees-of-freedom are only loosely coupled, the six equations of motion are not solved simultaneously. Additional appendices investigate in more detail certain characteristics of the equations which directly impact multisensor performance

A.2 NOMENCLATURE

For the ensuing analysis the following conventions will be followed:

- (1) Vectors will be denoted by an overline and matrices by double overline. A superscript indicates the reference frame in which the vector is measured. Two letter subscripts will be employed. The first subscript indicates the coordinate frame where the vector originates and the second, the ending point of the vector. For example, \bar{a}_{ic}^f indicates the acceleration of the case with respect to inertial space in float coordinates. The vector triad is ordered as spin, input and output.
- (2) The acceleration (\bar{a}_{ic}^c) of the case's nominal center and the angular rotation ($\bar{\omega}_{ic}^c$) of the case with respect to inertial space will be considered as inputs. \bar{a}_{ic}^c includes gravitational attraction.

$$\bar{a}_{ic}^c = \begin{bmatrix} a_S \\ a_I \\ a_O \end{bmatrix} \quad (A-1a)$$

$$\bar{\omega}_{ic}^c = \begin{bmatrix} \omega_S \\ \omega_I \\ \omega_O \end{bmatrix} \quad (A-1b)$$

where S, I, and O denote spin, input, and output, respectively.

- (3) Three-degrees-of-freedom are given by displacement vector from the nominal center of the case to the nominal center of the float; that is,

$$\bar{r}_{cf}^c = \begin{bmatrix} x_S \\ x_I \\ x_O \end{bmatrix} \quad (A-2)$$

- (4) Three additional degrees of freedom are defined by the angular rotation of the float with respect to the case. The rotation matrix from float to case coordinates is given by:

$$\bar{C}_c^F = \begin{bmatrix} 1 & \theta_O & -\theta_I \\ -\theta_O & 1 & \theta_S \\ \theta_I & -\theta_S & 1 \end{bmatrix} \quad (A-3)$$

where small angles have been assumed. The angles are measured about the nominal case axes to the nominal float axes as indicated by the subscripts.

- (5) The acceleration of the nominal float center with respect to inertial space is given approximately by:

$$\bar{a}_{iF}^C = \bar{a}_{iC}^C + \ddot{\bar{r}}_{cF}^C \quad (A.4a)$$

where the products of case rates ($\bar{\omega}_{iC}^C$) and float to case displacements (\bar{r}_{cF}^C) have been assumed small.

- (6) The angular velocity of the float with respect to inertial space in float coordinates is given within the limit of small angle approximations by:

$$\bar{\omega}_{iF}^F = \begin{bmatrix} \dot{\theta}_S \\ \dot{\theta}_I \\ \dot{\theta}_O \end{bmatrix} + \bar{C}_c^F \bar{\omega}_{iC}^C \quad (A.4b)$$

for this use, \bar{C}_c^F can be assumed identity.

A.3 EQUATIONS OF MOTION

Application of Newton's Laws to the float result in six scalar equations which permit solution for the six-degrees-of-freedom. For linear translation:

$$\Sigma \bar{F} = m \bar{a}_{i-cm}^C \quad (A-5)$$

and for rotation

$$\Sigma \bar{M} = \frac{d}{dt} \bar{H} \quad (A-6)$$

where

Σ denotes summation

F = forces

M = applied torques

H = angular moment of the float

$\frac{d}{dt}$ = differentiation with respect to time

m = mass of float including wheel

\bar{a}_{i-cm}^C = acceleration of float center of mass which is approximately \bar{a}_{iF}^F by design.

Differentiation of the float's angular momentum is:

$$\frac{d\bar{H}}{dt} = \frac{d}{dt} \left[\bar{I} \bar{\omega}_{iF}^F \right] + \bar{\omega}_{iF}^F \times \left[\bar{I} \bar{\omega}_{iF}^F \right] + \frac{d}{dt} \bar{H}_w + \bar{\omega}_{iF}^F \times \bar{H}_w \quad (A-7)$$

where: $\bar{I} = \begin{bmatrix} I_S & 0 & 0 \\ 0 & I_I & 0 \\ 0 & 0 & I_O \end{bmatrix}$ is the inertia matrix or sensor.

I includes both the inertias of the float and the wheel. As a first approximation, cross products of inertia are neglected.

$$\bar{H}_w = \begin{bmatrix} H \\ 0 \\ 0 \end{bmatrix} = \text{spin angular momentum of wheel}$$

where:

$$H = I_w \Omega$$

I_w = inertia of wheel about its spin axis

Ω = angular velocity of wheel with respect to float

The sum of the forces is represented:

$$\Sigma \bar{F} = \bar{F}_{sus} + \bar{F}_{vis} + \bar{F}_{buoy} + \bar{F}_{add} \quad (A-8)$$

where:

\bar{F}_{sus} = suspension forces which are discussed further in Appendices B, C, and F.

\bar{F} = fluid forces exerted by fluid during float motion

$$= \begin{bmatrix} C_T & \dot{x}_S \\ C_T & \dot{x}_I \\ C_{AX} & \dot{x}_O \end{bmatrix}$$

the fluid forces are assumed to functions of the translation velocity in the given direction; however, this simple model may be inaccurate. Reference 5 discusses more accurate models.

F_{buoy} = buoyant forces exerted by fluid. The buoyant force is described by the vector relation:

$$\bar{F}_{\text{buoy}} = \bar{B} a_{ic}^C$$

where the matrix \bar{B} is a function of temperature distribution. As a first approximation, let the matrix \bar{B} equal a scalar B multiplied by the identity matrix.

The sum of the applied torques is represented as:

$$\Sigma \bar{M} = \bar{M}_{\text{sus}} + \bar{M}_{\text{vis}} + \bar{M}_{\text{buoy}} + \bar{M}_g + \bar{M}_{g^2} + \bar{r}_{Fb} \times \bar{F}_{\text{buoy}} + \bar{M}_{\text{add}} \quad (\text{A-9})$$

where:

\bar{M}_{sus} = torques applied by the magnetic suspensions which are discussed in Appendices B, C, and F.

\bar{M}_{vis} = torques applied by fluid during float motion.

$$= \begin{bmatrix} C_R & \dot{\theta}_S \\ C_R & \dot{\theta}_I \\ C_O & \dot{\theta}_O \end{bmatrix}$$

As for the viscous forces, this simple model may be inaccurate.

- \bar{M}_{buoy} = temperature sensitive torques exerted by fluid independent of float motion. These torques, also called convection torques, are discussed in greater detail in Appendix E.
- \bar{M}_g = torques caused by the noncoincidence of the center of mass and the origin about which torques are summed. Note that the nominal center for torque summation is arbitrarily selected. In float coordinates:

$$\bar{M}_g = -\bar{r}_{F-\text{cm}}^F \times m\bar{a}_{IF}^F$$

where:

$\bar{r}_{F-\text{cm}}^F$ is the displacement from the origin to the center of mass, a constant vector in float coordinates. For most multisensors, study \bar{a}_{IF}^F can be set equal to \bar{a}_{ic}^C since the float case angles are restricted to values less than 0.001 rads by the float case clearance. The input of this term is discussed following (A-11).

\bar{M}_{g2} = torques proportional to acceleration squared which may be represented as:

$$\bar{M}_{g2} = \begin{bmatrix} -k_{II}a_Ia_O - k_{IS}a_Sa_O - k_{IO}a_O^2 + k_{OI}a_I^2 + k_{OS}a_Sa_I + k_{OO}a_Oa_I \\ -k_{OO}a_Oa_S - k_{OI}a_Ia_S - k_{OS}a_S^2 + k_{SO}a_O^2 + k_{SI}a_Ia_O + k_{SS}a_Sa_O \\ -k_{SS}a_Sa_I - k_{SO}a_Oa_I - k_{SI}a_I^2 + k_{IS}a_S^2 + k_{IO}a_Oa_S + k_{II}a_Sa_I \end{bmatrix}$$

where:

k_{ij} are constant coefficients which represent structural and bearing compliance.

$\bar{r}_{Fb} \times \bar{F}_{\text{buoy}}$ is caused by the buoyant force's not acting through the float coordinate center.

\bar{M}_{add} are other torques such as those caused by flex leads or unmodeled interactions of magnetic fields.

With the simplifying assumptions notes, (A-7), (A-8), and (A-9) are substituted into (A-5) and (A-6) to obtain the equations of motion in a form useful for additional study. The equations of motion for translation are:

$$m\ddot{x}_S + C_T \dot{x}_S = (B-m) a_S + F_{\text{sus}}(S) + F_{\text{add}}(S) \quad (\text{A-10a})$$

$$m\ddot{x}_I + C_T \dot{x}_I = (B-m) a_I + F_{\text{sus}}(I) + F_{\text{add}}(I) \quad (\text{A-10b})$$

$$m\ddot{x}_S + C_{AX} \dot{x}_O = (B-m) a_O + F_{\text{sus}}(O) + F_{\text{add}}(O) \quad (\text{A-10c})$$

For rotation, the motion equations are:

$$\begin{aligned} I_S \ddot{\theta}_S + C_R \dot{\theta}_S &= a_I^P - a_O U_I + M_{\text{sus}}(S) + M_{g^2}(S) + M_{\text{add}}(S) \\ &+ M_{\text{buoy}}(S) - \dot{H} - I_S \dot{\omega}_S + (I_I - I_O)(\omega_I + \dot{\theta}_I)(\omega_O + \dot{\theta}_O) \end{aligned} \quad (\text{A-11a})$$

$$\begin{aligned} I_I \ddot{\theta}_I + C_R \dot{\theta}_I + H \dot{\theta}_O &= -a_S^P + a_O U_S + M_{\text{sus}}(I) + M_{g^2}(I) + M_{\text{add}}(I) \\ &+ M_{\text{buoy}}(I) - H \omega_O - I_I \dot{\omega}_I + (I_O - I_S)(\omega_S + \dot{\theta}_S)(\omega_O + \dot{\theta}_O) \end{aligned} \quad (\text{A-11b})$$

$$\begin{aligned} I_O \ddot{\theta}_O + C_O \dot{\theta}_O - H \dot{\theta}_I &= a_S U_I - a_I U_S + M_{\text{sus}}(O) + M_{g^2}(O) + M_{\text{add}}(O) \\ &+ M_{\text{buoy}}(O) + H \omega_I - I_O \dot{\omega}_O + (I_S - I_I)(\omega_S + \dot{\theta}_S)(\omega_I + \dot{\theta}_I) \end{aligned} \quad (\text{A-11c})$$

where:

$$\begin{aligned} P &= m r_{F-\text{cm}}^F(O) - B r_{Fb}^F(O) \\ &= \text{pendulosity along the output axis. The pendulous torques which the suspensions rebalance are the couple between the acceleration and buoyant forces.} \\ U_S &= m r_{F-\text{cm}}^F(S) - B r_{Fb}^F(S) \\ &= \text{unbalance along spin axis.} \\ U_I &= m r_{F-\text{cm}}^F(I) - B r_{Fb}^F(I) \\ &= \text{unbalance along input axis.} \end{aligned}$$

Ideally, the unbalance terms U_S and U_I should be zero.

APPENDIX B

COUPLED ROTATIONAL AND TRANSLATIONAL MOTION

B.1 SUMMARY

To further understanding of suspension tuning in the multisensor, a float permitted two-degree-of-freedom (2-DOF) is studied. The permitted motion is rotation and linear translation with forces applied at the float ends.

The control requirements necessary to decouple the modes and the effects of control strategy on the two modes, are discussed. The active suspensions used for the feasibility multisensor are studied.

The principal conclusions are:

- (1) Float suspensions should be designed with consideration of both rotational and translational modes.
- (2) For the control used in the feasibility instrument, the rotational mode is quicker than the translational mode.

B.2 BASIC MODEL

As depicted in Figure B-1, rotation about the center of mass and translational motion of the cm, are permitted. The equations of motion to be analyzed are Newton's law for translational motion:

$$F + F_1 + F_2 = x(ms^2 + C_t s) \quad (B-1)$$

and for rotational motion:

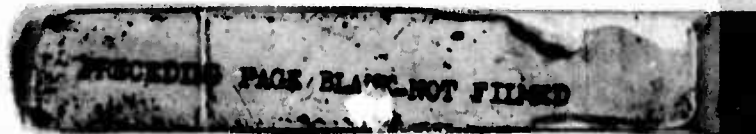
$$M + F_1 l_1 - F_2 l_2 = \theta (I s^2 + c_r s) \quad (B-2)$$

where:

s = the Laplace operator d/dt .

F_1, F_2 = suspension forces.

F = external force such as buoyancy.



B.3 EQUATIONS OF MOTION WITH SUSPENSION FORCES

Several expressions are derived to relate various suspension control strategies to the resulting rotational and translational modes. General expressions are derived and extraneous terms will be discarded when appropriate.

The suspension control laws written in terms of the cm motion and rotation about the cm are:

$$\begin{bmatrix} F_1 \\ F_2 \end{bmatrix} = - \begin{bmatrix} G_{1x} & G_{1\theta} \\ G_{2x} & G_{2\theta} \end{bmatrix} \begin{bmatrix} x \\ \theta \end{bmatrix} \quad (B-3)$$

where the G's are arbitrary compensators so that both passive and active suspensions can be handled. In matrix form, the dynamic equations are:

$$\left[\begin{array}{c|c} ms^2 + C_t S + G_{1x} + G_{2x} & G_{1\theta} + G_{2\theta} \\ \hline G_{1x} l_1 - G_{2x} l_2 & IS^2 + C_R S + G_{1\theta} l_1 - G_{2\theta} l_2 \end{array} \right] \begin{bmatrix} x \\ \theta \end{bmatrix} = \begin{bmatrix} F \\ M \end{bmatrix} \quad (B-4)$$

Since signal generators usually measure the displacement at the float ends, (B-3) and (B-4) are rewritten with x_1 and x_2 , the displacement, at the float ends (see Figure B-1)

$$\begin{bmatrix} x_1 \\ x_2 \end{bmatrix} = \begin{bmatrix} 1 & l_1 \\ 1 & -l_2 \end{bmatrix} \begin{bmatrix} x \\ \theta \end{bmatrix} \quad (B-5)$$

where:

- l_1 = the distance from end 1 to the cm and similarly for l_2 .
- M = externally applied torque (for example, torques caused by fluid motion).
- m = float mass.
- c_t = damping constant for translational motion.
- x = displacement of center of mass.

- I = moment of inertia about center of mass
- c = damping constant for rotational motion
- θ = angular displacement about cm

The generalized coordinates x and θ are selected since these variables permit the simplest description of the resulting motions. Specifically, if pure torques are applied to the float, the resulting motion can be viewed as a rotation about the center of mass which does not move translationally.

Solving (B-5) for the position of the mass center and the angular position:

$$\begin{bmatrix} x \\ \theta \end{bmatrix} = \frac{1}{l_1 + l_2} \begin{bmatrix} l_2 & l_1 \\ 1 & -1 \end{bmatrix} \begin{bmatrix} x_1 \\ x_2 \end{bmatrix} \quad (B-6)$$

Substitution of (B-6) into (B-4) gives the suspension control law in terms of the end displacements:

$$\begin{bmatrix} F_1 \\ F_2 \end{bmatrix} = \frac{\begin{bmatrix} G_{1x} l_2 + G_{1\theta} & G_{1x} l_1 - G_{1\theta} \\ G_{2x} l_2 + G_{2\theta} & G_{2x} l_1 - G_{2\theta} \end{bmatrix}}{l_1 + l_2} \begin{bmatrix} x_1 \\ x_2 \end{bmatrix} \quad (B-7)$$

This work will discuss strategies for controlling the suspension forces in general. Specific examples pertaining to the feasibility multisensor will be presented.

B.4 DISCUSSION ON DECOUPLING

With freedom to select the four compensators of (3), the designer has sufficient degrees of freedom to decouple the translational and rotational modes by selecting:

$$G_{2\theta} = -G_{1\theta} \quad (B-8a)$$

$$G_{2x} = \frac{l_1}{l_2} G_{1x} \quad (B-8b)$$

Sufficient freedom then remains to independently tune the rotational and translational loop; that is, with (B-8), (B-4) becomes:

$$\left[\begin{array}{c|c} ms^2 + C_t s + G_{1x} \left(\frac{l_1 + l_2}{l_2} \right) & 0 \\ \hline 0 & Is^2 + C_r s + G_{1\theta} (l_1 + l_2) \end{array} \right] \begin{bmatrix} X \\ \theta \end{bmatrix} = \begin{bmatrix} F \\ M \end{bmatrix} \quad (B-9)$$

With (B-8), the control law for decoupled motion when the end positions are measured is determined from (B-7):

$$\begin{bmatrix} F_1 \\ F_2 \end{bmatrix} = \underbrace{\begin{bmatrix} G_{1x} l_2 + G_{1\theta} & G_{1x} l_1 - G_{1\theta} \\ \hline G_{1x} l_1 - G_{1\theta} & G_{1x} \left(\frac{l_1}{l_2} \right)^2 + G_{1\theta} \end{bmatrix}}_{l_1 + l_2} \begin{bmatrix} X_1 \\ X_2 \end{bmatrix} \quad (B-10)$$

Thus, in general, decoupled motion cannot be attained by controlling the force with only the measurement from that end. Since the forces must be measured at both ends, the complexity of mechanizing (B-7) is not exorbitant. In summary, the requirements for complexity decoupling the loops have been derived in (B-8) and (B-10).

B.5 END DISPLACEMENT MEASUREMENT WITHOUT CROSSFEEDBACK

The multisensor feasibility is tuned with active suspensions and compensators $G(s)$ so that:

$$\begin{bmatrix} F_1 \\ F_2 \end{bmatrix} = \begin{bmatrix} G(s) & 0 \\ \hline 0 & G(s) \end{bmatrix} \begin{bmatrix} X_1 \\ X_2 \end{bmatrix} \quad (B-11)$$

A general expression for systems with end displacement measurement and without crossfeedback (F_1 is not a function of x_2 and similarly for F_2 , x_1) is derived from (B-7) by setting:

$$G_{1\theta} = G_{1x}l_1 \quad (B-12a)$$

$$G_{2\theta} = -G_{2x}l_2 \quad (B-12b)$$

Substitution of (B-12) into (B-4) yields the equivalent of motion for the rotational and translational modes:

$$\begin{bmatrix} ms^2 + C_T s + G_{1x} + G_{2x} & G_{1x}l_1 - G_{2x}l_2 \\ \hline G_{1x}l_1 - G_{2x}l_2 & Is + C_R s + G_{1x}l_1^2 + G_{2x}l_2^2 \end{bmatrix} \begin{bmatrix} X \\ \theta \end{bmatrix} = \begin{bmatrix} F \\ M \end{bmatrix} \quad (B-13)$$

In general, the modes are not decoupled; however, for most practical systems (even the multisensor with pendulosity along the output axis) l_1 is approximately l_2 and G_{1x} is approximately G_{2x} so that the translational and rotational modes are effectively decoupled. Mass m and inertia I can be neglected compared to the damping constant C_R and C_T and the motion equations for systems which measure end displacement and do not employ crossfeedback become:

$$\begin{bmatrix} C_T s + 2G_{1x} & 0 \\ \hline 0 & C_R s + 2G_{1x}l_1^2 \end{bmatrix} \begin{bmatrix} X \\ \theta \end{bmatrix} = \begin{bmatrix} F \\ M \end{bmatrix} \quad (B-14)$$

Although the equations are decoupled, the freedom to independently tune the rotational and translational loops has been lost (if the lengths are assumed fixed). This loss of freedom is caused by the decision not to employ crossfeedback. Thus, if one loop is well tuned, less desirable dynamic performance might result for the other loops.

With passive radial suspensions, both modes are first order with different characteristic times. For active suspension, the mode shapes become more complicated so that the $G_{1x}(s)$ selection is more interesting.

B.6 THE MULTISENSOR RADIAL SUSPENSION

As presently configured, the multisensor has active radial suspensions that result in dynamic equations of the form (B-14). This active suspension is:

$$2G_{1x} l_1^2 = \frac{C_R k_R (S+a)}{S (S+b)} \quad (B-15)$$

The equations of motion for the translational and rotational modes are then:

$$\theta \left[S^3 + bS + k_R (S+a) \right] = \frac{M}{C_R} \quad (B-16a)$$

$$X \left[S^3 + bS + k_T (S+a) \right] = \frac{F}{C_R} S(S+b) \quad (B-16b)$$

where:

$$k_T = \frac{C_R k_R}{C_T l_1^2}$$

Thus, the dynamic performances differ because of the different loop gains which are caused by the rotational and translational damping constants not being equal and the relation between force and torque through the moment arms. The different performance are then related to the pole positions on the root locus diagram. Selection of performance on one loop decides the gain and, hence, pole positions for the other loop.

For the feasibility multisensor:

$$C_R/C_T = \frac{1}{2} (\text{cm})^2$$

$$l_1 = 2.8 \text{ cm}$$

the dynamic compensator was originally selected so that:

$$k_R = 1.41 \times 10^4 \frac{1}{s^2}$$

$$A = 22.8 s^{-1}$$

$$B = 173 s^{-1}$$

The gain of the translational loop is then:

$$k_T = 900 1/s^2$$

The eigenvalues for the rotational mode are:

$$-34.4, \quad -69.7 \quad + \quad 67.3j$$

and for the translational mode:

$$-168., \quad -2.04 \quad \pm \quad 10.2 j$$

Further insight into these responses is offered by the root locus of Figure B-2. Note that the translational loop is underdamped (damping ratio - 0.2) and decays much more slowly than the rotational loop. The responses of the two loops are compared in Figure B-3 for step inputs of force and torque.

By using crossfeedback (B-10), the two loops can be tuned independently if improved performance is desired. Note that the loops can be decoupled by the windings discussed in paragraph 3.9. The cross-connection allows application of the translational force independently of the rotational torque.

Because of noise described in Section 2 and paragraph 3.6, the loops used through multisensor tests were tuned so that closed-loop poles were 1/30 of those used in examples.

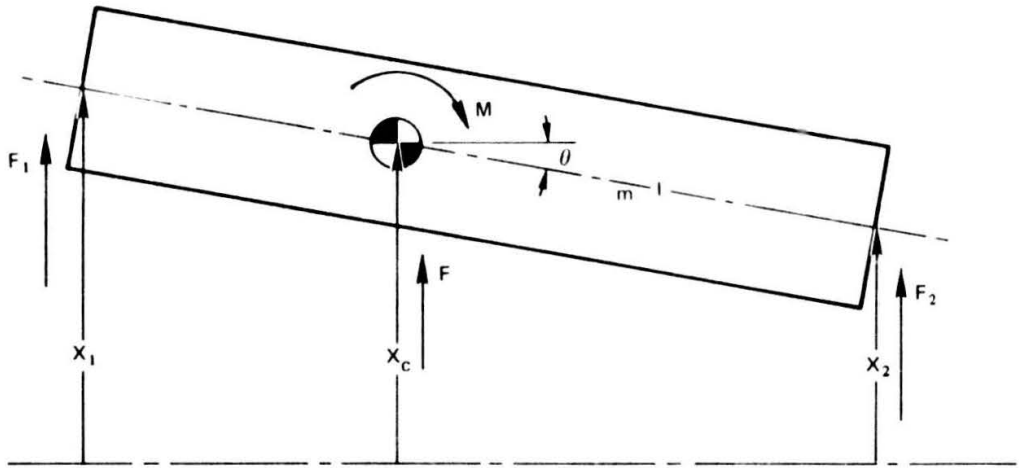


Figure B.1. Coordinates for rotational-translational model.

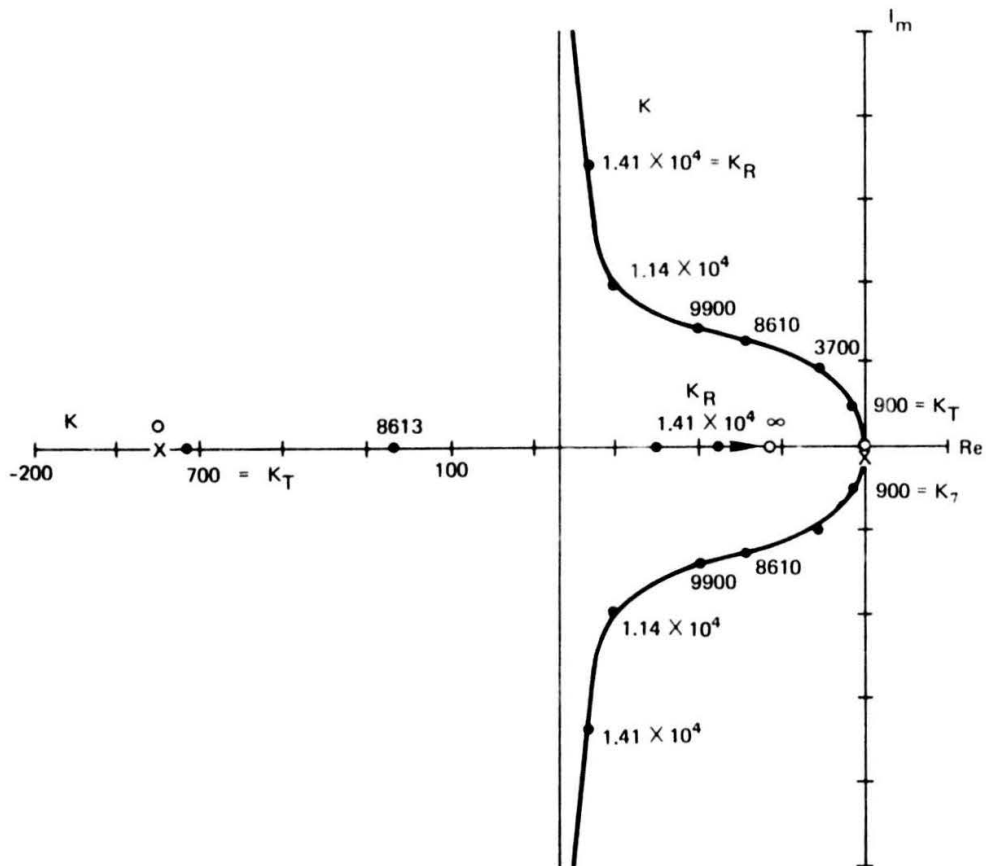


Figure B.2. Root locus for multisensor suspension.

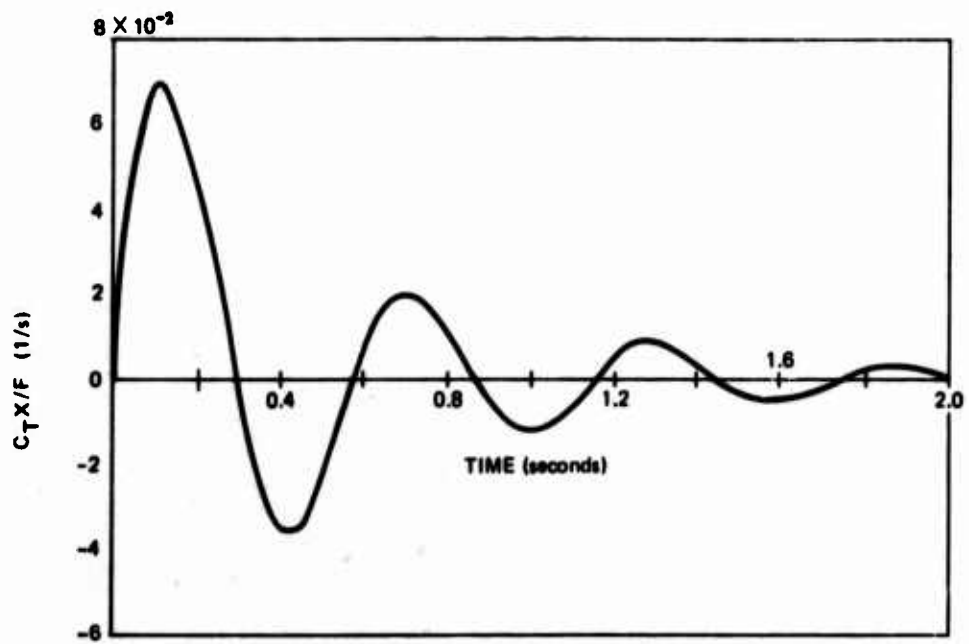
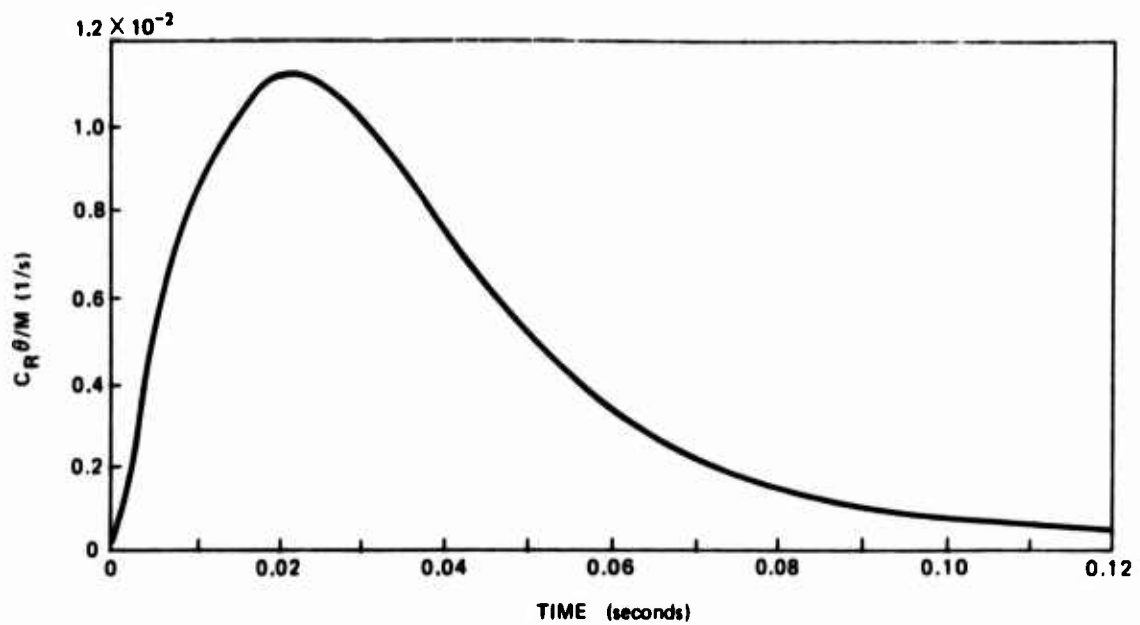


Figure B.3. Time traces for active suspension (Equation B-16) end measurement, no crossfeedback.

APPENDIX C

TWO-DEGREE-OF-FREEDOM FLOAT DYNAMICS WITH WHEEL COUPLING

C.1 SUMMARY

The behavior of a simplified multisensor model which focuses on the interaction of the control loops about input and output axes coupled by the wheel angular momentum is studied. The study indicates the conditions under which control loops can be designed from single-loop analyses and indicates possible instrument output errors which result from the intercoupling phenomena.

Considerations of damping constants discussed in Appendix D require the two-degree-of-freedom analysis enclosed herein. The similarity between lightly and highly damped instruments is emphasized (see paragraph C.7). As will be discussed further, the lightly damped approach allows excellent instrument response about the three rotational axes and enables rapid radial and axial translation which permits rapid warmup while facilitating instrument fill.

C.2 SCOPE

For a simplified linearized model, the angular-moment coupling of the control loops about the input and output axis of a gyroscopic device is studied. The analysis is presented in a general framework so that results are applicable to gyros, PIGAs, and multisensors. Specifically the following matrix equation is studied:

$$\left[\begin{array}{c|c} SI_I + C_I & H \\ \hline -H & SI_O + C_O \end{array} \right] \begin{bmatrix} S\theta_I \\ S\theta_O \end{bmatrix} = \begin{bmatrix} M_I - M_{RI} \\ M_O - M_{RO} \end{bmatrix} \quad (C-1).$$

where:

- θ = float-case misalignment
- H = angular momentum



- I = moment of inertia
 C = damping constant
 S = Laplace transform operator
 M = externally applied torque such as $H\omega$ (gyroscopic moment) or $P\alpha$ (pendulosity)
 M_R = rebalance torque applied by suspension (M_R is usually a function of the float-case misalignment)

Subscripts

- I = input axis
 O = output axis

For most single-degree-of-freedom analyses, the two equations are treated separately, i.e., H is assumed not to affect the loop performance. This report studies in detail the effects of various control strategies for M_R on the instrument performance described by (C-1).

C.3 JUSTIFICATION FOR NEGLECTING INERTIA

The eigenvalues (poles) of the open-loop system are

$$\lambda = -\frac{1}{2} \left[\frac{C_O}{I_O} + \frac{C_I}{I_I} \pm \sqrt{\left(\frac{C_O}{I_O} - \frac{C_I}{I_I} \right)^2 - \frac{4H^2}{I_I I_O}} \right] \quad (C-2)$$

and

$$\lambda = 0, 0$$

For typical instruments

$$H \simeq C_O = 1.6 \times 10^5 \text{ dyn-cm-s}$$

$$C_I \simeq 1.6 \times 10^6 \text{ dyn-cm-s}$$

$$I_O \simeq I_I = 200 \text{ gm-cm}^2$$

$$\lambda = -800 \text{ s}^{-1}, -8 \times 10^6 \text{ s}^{-1}, 0., 0.$$

Since gyros and accelerometers are usually tuned for a closed-loop bandwidth in the vicinity of 25 Hz (157 rad/s) as a first-order approximation, the fast open-loop poles may be neglected. In root locus terms, this assumption may be diagrammed as in Figure C-1. Since the fast poles are far from the region where the open-loop poles will be moved for closed-loop operation, the fast poles can be omitted as a first approximation. Omitting the fast poles (implies neglecting I_O and I_I in Equation (C-1)).

Similarly, consider a typical lightly damped situation.

$$H \simeq C_I = 1.6 \times 10^5 \text{ dyn-cm-s}$$

$$C_O = 1.6 \times 10^2 \text{ dyn-cm-s}$$

$$I_O \simeq I_I = 200 \text{ gm-cm}^2$$

$$\lambda = -400 \pm 693j, 0., 0.$$

The first eigenvalue has an undamped natural frequency of 800 rad/s; thus, although the output axis is lightly damped, the first poles are far from the region of interest (Figure C-1b) and for a first approximation both I_O and I_I can be neglected (although mid-range points exist where this assumption is invalid). Note that this result contradicts single-loop theory which would say the pole for the output axis is $C_O/C_I = 1 \text{ rad/s}$.

C.4 REDUCED MOTION EQUATIONS

Neglecting the inertias in Equation (C-1) and solving for the angles

$$\frac{d}{dt} \begin{bmatrix} \theta_I \\ \theta_O \end{bmatrix} = \frac{\begin{bmatrix} C_O & -H \\ H & C_I \end{bmatrix} \begin{bmatrix} M_I - M_{RI} \\ M_O - M_{RO} \end{bmatrix}}{C_O C_I + H^2} \quad (C-3)$$

The above is a fundamental demonstration of the coupling between input and output axes; that is, torques applied about both the input and output axes affect both θ_I and θ_O . For H small compared to C_I or C_O , the equations for θ_I and θ_O decouple, a phenomenon discussed further.

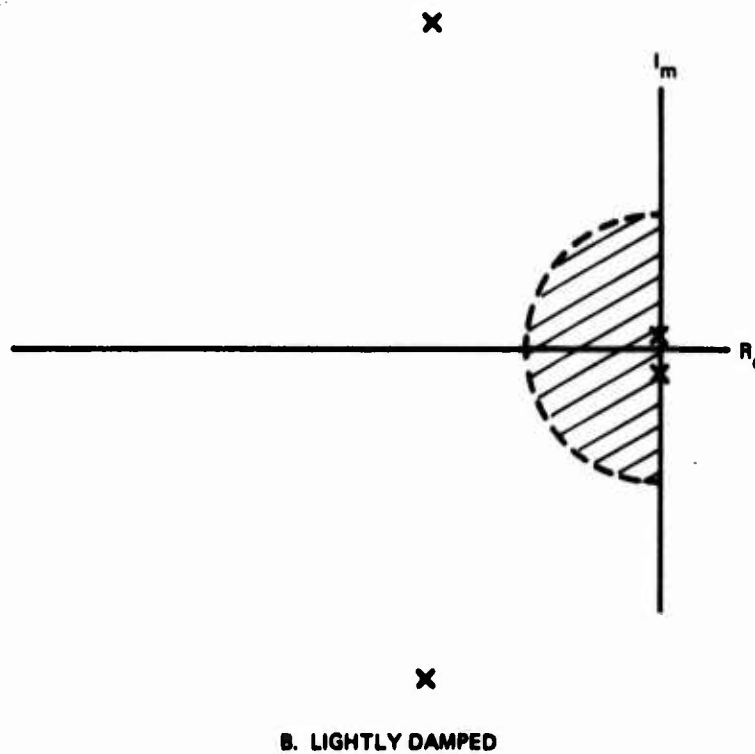
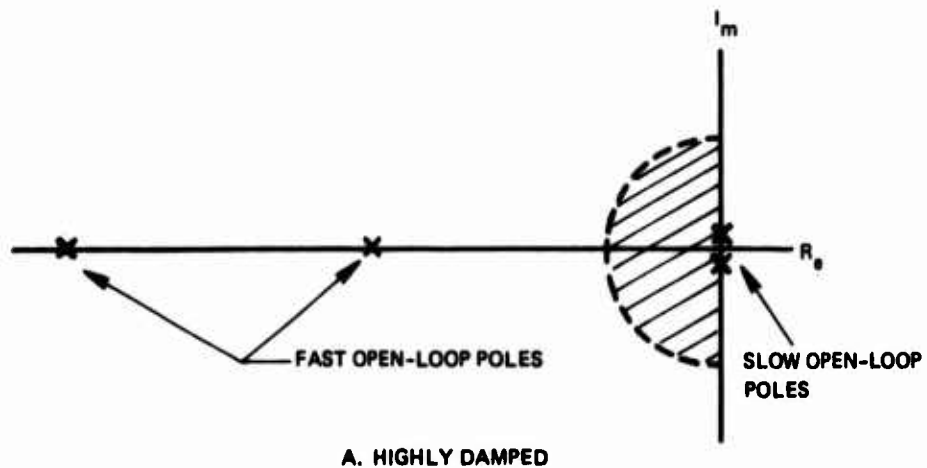


Figure C-1. Schematic root locus justifying omission of inertia from motion equation. Poles at origin will only be moved in shaded area far from fast poles.

C.5 GENERAL EQUATIONS FOR TWO-DEGREE-OF-FREEDOM WITH CONTROL

Consider the rebalance torques described by the control laws

$$\begin{bmatrix} M_{RI}(s) \\ M_{RO}(s) \end{bmatrix} = \begin{bmatrix} G_{II}(s) & G_{IO}(s) \\ G_{OI}(s) & G_{OO}(s) \end{bmatrix} \begin{bmatrix} \theta_I(s) \\ \theta_O(s) \end{bmatrix} \quad (C-4)$$

For generality, each rebalance torque is a function of both angles. Precise expressions for the G's are discussed later. Inserting (C-4) into (C-3), the transfer matrix relating the angles to the torque is

$$\begin{bmatrix} \theta_I \\ \theta_O \end{bmatrix} = \frac{\begin{bmatrix} SC_O + G_{OO} & -SH - G_{IO} \\ SH - G_{OI} & SC_I + G_{II} \end{bmatrix} \begin{bmatrix} M_I \\ M_O \end{bmatrix}}{\left[s^2(C_I C_O + H^2) + s(C_I G_{OO} + C_O G_{II} + HG_{IO} - HG_{OI}) + G_{II} G_{OO} - G_{IO} G_{OI} \right]} \quad (C-5)$$

Substituting Equation (C-5) into Equation (C-4) determines the rebalance torques as functions of the input torques.

$$\begin{bmatrix} M_{RI} \\ M_{RO} \end{bmatrix} = \frac{\begin{bmatrix} s(C_O G_{II} + HG_{IO}) + G_{II} G_{OO} - G_{IO} G_{OI} & s(-HG_{II} + G_{IO} C_I) \\ -s(C_O G_{OI} + HG_{OO}) & s(C_I G_{OO} - HG_{OI}) + G_{II} G_{OO} - G_{IO} G_{OI} \end{bmatrix}}{\text{DEN}} \times \begin{bmatrix} M_I \\ M_O \end{bmatrix} \quad (C-6)$$

where

DEN is the demoninator of Equation (C-5). Also

$$\begin{bmatrix} M_I - M_{RI} \\ M_O - M_{RO} \end{bmatrix} = \frac{\begin{bmatrix} S^2(C_I C_O + H^2) + S(C_I G_{OO} - H G_{OI}) & -S(H G_{II} + G_{IO} C_I) \\ -S(C_O G_{OI} + H G_{OO}) & S^2(C_I C_O + H^2) + S(C_I G_{OO} + H G_{IO}) \end{bmatrix}}{\text{DEN}} \times \begin{bmatrix} M_I \\ M_O \end{bmatrix} \quad (C-7)$$

At this point, several general observations are offered. In general, the float-case-angle misalignments and both rebalance torques are influenced by torque inputs about both axes. Later discussion will demonstrate some simplifications which occur in practical situations and will discuss the implications of the cross-coupling on instrument performance.

Note, from Equations (C-3) and (C-4) or (C-5), if $G_{IO} = -SH$, or $G_{OI} = SH$, the equations decouple. Specifically, the denominator becomes:

$$\text{DEN} = (S C_I + G_{II})(S C_O + G_{OO}) \quad (C-8)$$

and the poles for each loop can be determined independently. Also, $G_{IO} = -SH$ eliminates the influence of M_O on θ_I (and similarly for G_{OI} , M_I , and θ_O).

Another option is the elimination of input M_O effects on rebalance M_{RI} by judicious selection of the crossfeedback compensator G_{IO} , Equation (C-6) or (C-7). In this situation, the system poles are not decoupled as in Equation (C-8).

As will be discussed further, a situation that appears frequently in instrument design is zero crossfeedback; that is $G_{IO} = G_{OI} = 0$, for which

$$\text{DEN} = S^2(C_I C_O + H^2) + S(C_I G_{OO} + C_O G_{II}) + G_{OO} G_{II} \quad (C-9)$$

For H^2 small compared to $C_I C_O$, the loops decouple; however, the HS terms in (C-1), (C-3), (C-6) and (C-7) indicate that $H\dot{\theta}_I$ is acting like an input in the θ_O-M_O loop (and similarly $H\dot{\theta}_O$ in the θ_I-M_I loop).

C.6 MULTISENSOR ACTIVE CONTROLS

A numerical example is presented to demonstrate the performance of an optimized multisensor where both the input and output axes are controlled actively with loops whose bandwidth is approximately 22 Hz. Both loops are equipped with integral compensation so that under no coupling the dynamic response of the loops are identical. Parameter values are listed in Table C-1.

TABLE C-1. VALUES FOR INTEGRAL-INTEGRAL STUDY.

| | | |
|----------|---|---|
| C_O | = | 1.6×10^5 dyn-cm-s |
| H | = | 1.6×10^5 dyn-cm-s |
| C_I | = | $\left\{ \begin{array}{l} 1.6 \times 10^4 \text{ dyn-cm-s} \\ 1.6 \times 10^5 \text{ dyn-cm-s} \\ 1.6 \times 10^6 \text{ dyn-cm-s} \\ 1.6 \times 10^7 \text{ dyn-cm-s (used in plots)} \\ 1.6 \times 10^8 \text{ dyn-cm-s} \end{array} \right.$ |
| G_{II} | = | $\frac{C_I (1.41 \times 10^4) s^2 (S+22.8 s^{-1})}{S(S+173 s^{-1})}$ |
| G_{OO} | = | $\frac{C_O (1.41 \times 10^5) s^2 (S+22.8 s^{-1})}{S(S+173 s^{-1})}$ |

Table C-2 compares system eigenvalues as the damping about the input axis C_I varies. $H^2/C_I C_O$, less than 0.01, is required for open-loop design to give accurate pole placement in cross-coupled design.

TABLE C-2. POLES AS C_I CHANGES FOR INTEGRAL-INTEGRAL STUDY.

| C_I (dyn-cm-s) | $\frac{H^2}{C_I C_O}$ | Poles (S^{-1}) | | | |
|---------------------|-----------------------|-----------------------|--------------|-------------------|-------------------|
| ∞ | 0 | -34.6 | -34.6 | -69.2 \pm 67.3j | -69.2 \pm 67.3j |
| 1.6×10^8 | 0.001 | -34.4 | $\pm 0.9j$ | -72.8 \pm 66.7j | -65.8 \pm 67.6j |
| 1.6×10^7 | 0.01 | -34.0 | $\pm 2.76j$ | -80.7 \pm 65.7j | -58.4 \pm 68.5j |
| 1.6×10^6 | 0.1 | -31.0 | $\pm 6.782j$ | -104 \pm 62.8j | -38.4 \pm 69.6j |
| 1.6×10^5 | 1.0 | -23.4 | $\pm 9.65j$ | -145 \pm 48.6j | -4.2 \pm 58.2j |

For $H^2/C_I C_O = 0.01$, the system's response for steps in input torque are plotted in Figures C-2 and C-3. Although the responses for θ_I/M_I , θ_O/M_O , M_{RI}/M_I , and M_{RO}/M_O are essentially those of uncoupled loops, the coupling through the numerators of the transfer matrices is clearly evident. In particular, the rebalance torque about the output axis caused by torques about the input axis ($H\omega_O = M_I$) must be considered in designing systems which employ multisensors. The active suspension has greatly reduced the permissible angular motion about the input axis and eliminated the slow time constants associated with the high rotational damping about the output axis and the relatively soft magnetic suspensions. The output axis error M_{RO}/M_I is similar in both cases.

C.7 LOW DAMPING CONFIGURATION

With the inertia terms neglected, the coupled equations of motion are symmetric in that the roles of damping and angular momentum can be exchanged. Specifically, if $H^2 > 100 C_I C_O$, let $G_{II} = G_{OO} = 0$ and use the crossfeedback compensators G_{IO} and G_{OI} . The equations of motion are then identical to those for the examples of (C-6) where the high damping $C_I C_O > 100 H^2$.

Section 3.5 discusses the difficulty of obtaining suitable dynamic performance for loops that have large damping constants. For low damping ($H^2 > 100 C_I C_O$) the roles of damping and angular momentum have been exchanged in the motion equations.

Practically, suitable dynamic control can now be designed for all three rotational loops. If a viscosity is selected so that the damping about the spin axis is in the desired range (about 2×10^5 dyn-cm-s), the input-output axis pair will be in the lightly damped region where the angular momentum, not the damping constant, dominates the dynamic response. Since H near 2×10^5 dyn-cm-s is easily achieved (where size 18 numbers have been used for example), desirable dynamic response can be achieved about all three axes. Also, the low viscosity fluid (approximately 1/100 to 1/1000 of that commonly used in single-degree instruments) will permit large reduction in the time associated with radial and axial pull-in.

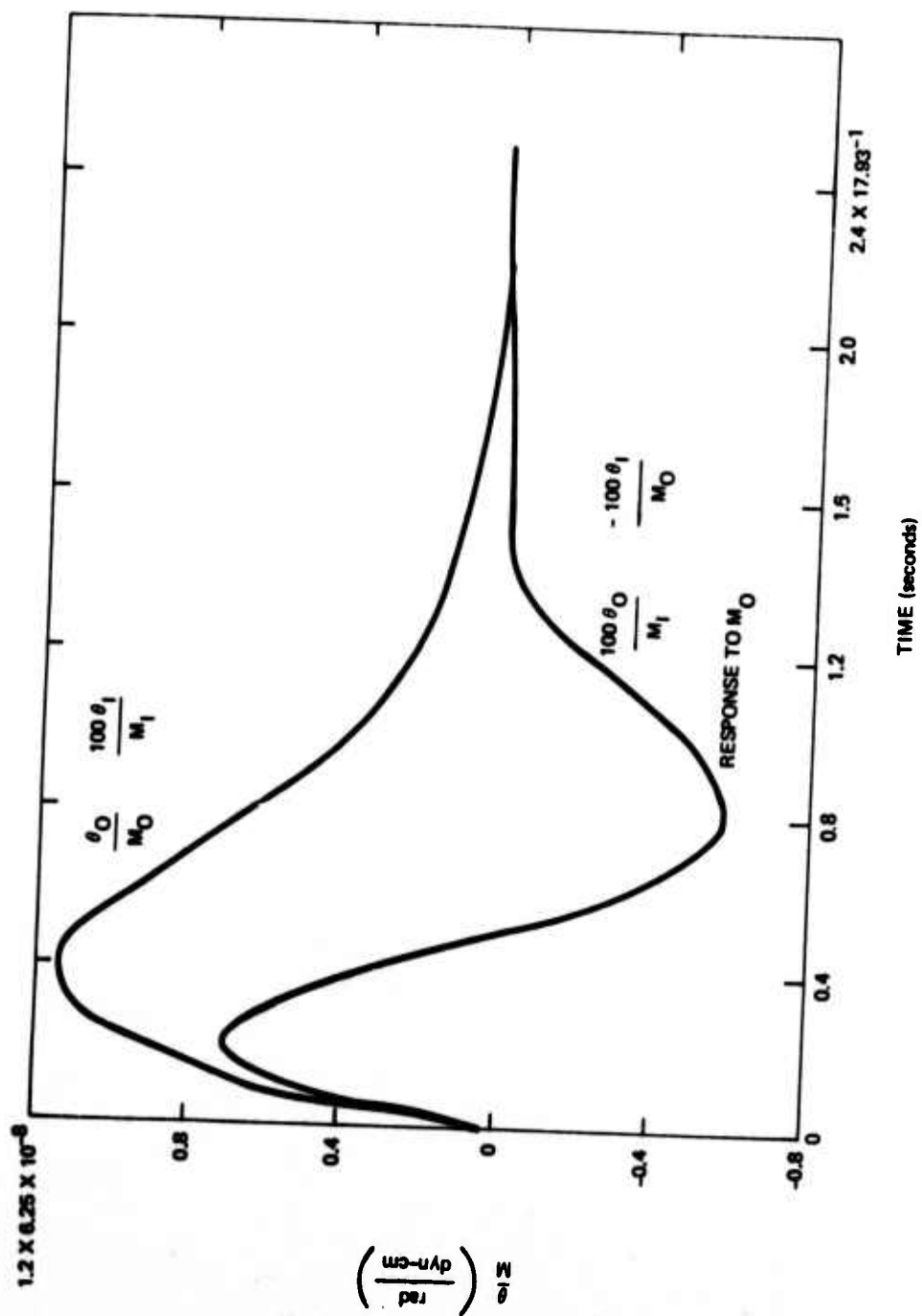


Figure C-2. Coupled integral loops. Float angles for steps in input torque.

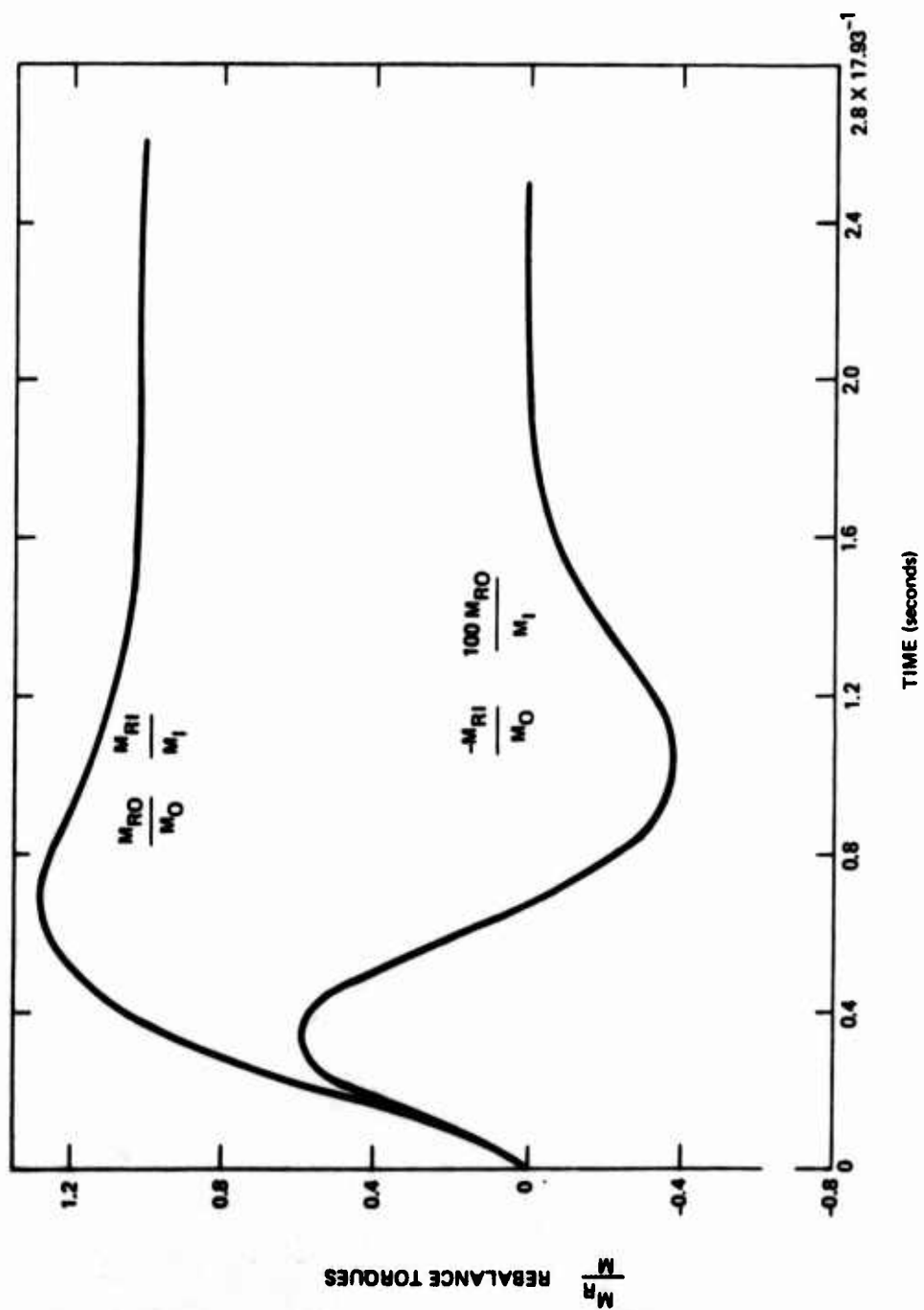


Figure C-3. Coupled integral loops. Rebalance torques for steps in input torques.

APPENDIX D

ACCELEROMETER RESOLUTION CONSIDERING ELASTIC RESTRAINT AND SIGNAL GENERATOR NOISE

D.1 SUMMARY

The uncertainty in the measured torques caused by uncertainty in the accelerometer signal generator is investigated. The effects of elastic restraint in the forcers are also included. The multisensor feasibility instrument is used as a baseline. The signal generator is modeled as white noise with an rms output of 1 milliarc s measured in the 0.1 to 50 Hz bandwidth.

Numerical examples based on the feasibility instrument demonstrate that elastic restraint should not be a significant problem in multisensor accelerometer channels provided that the radial transducer null does not shift, and that damping about a measurement axis should be less than 2×10^7 dyn-cm-s for an 18-size instrument.

For preliminary calculations, an approximate calculation demonstrates that 50 ppm accelerometer performance is equivalent to 0.7 cm/s velocity error for aircraft application.

D.2 ELASTIC RESTRAINT

A simple model of a clapper magnet pair arranged in push-pull appears in Figure(D-1). Retaining first order terms (no second order terms exist, but third and higher occur), the magnet force in the upward direction is:

$$F = \frac{\mu_0 N^2 A_P I_P^2}{g^2} \left[\frac{-I_S}{I_P} + \frac{x}{G} \right] \quad (D-1)$$

where:

N = number of turns in each coil

I_P = current in primary

G = normal air gap
 X = displacement
 A_p = area of one pole face

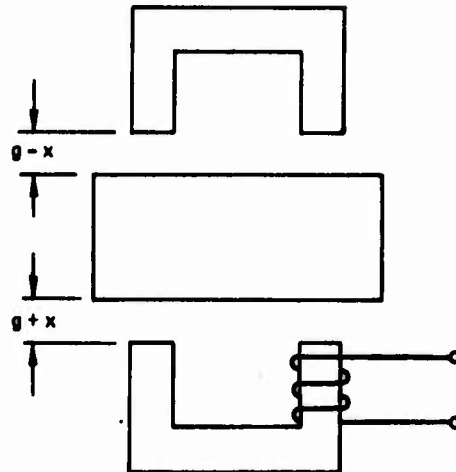


Figure D-1. Schematic of push-pull clapper forces.

The force is converted to torque about the float center (T) by multiplying suspension to center distance. Equation (D-1) may be rewritten as:

$$T = k_I I - k_X X \quad (D-2)$$

For the original multisensor feasibility instrument with primary current of 13.1 mA (two gravity accelerometer):

$$k_I = 95.4 \text{ dyn-cm/mA}$$

$$k_X = 8.2 \times 10^4 \text{ dyn-cm/cm}$$

By compensating the accelerometer signal generator primary, the elastic restraint can be reduced by two orders of magnitude; thus for design extrapolation:

$$k_x = 10^3 \text{ dyn-cm/cm}$$

is also used.

D.3 ACCELEROMETER EQUATIONS OF MOTION

The following assumptions are made in considering the resolution:

- (1) Translational motion of the float is ignored.
- (2) Two identical forces are assumed so that the torque exerted at one end is multiplied by two to obtain the total torque exerted by the magnetic suspensions.
- (3) Interactions about other rotational axes are ignored, so that only a single accelerometer channel need be studied. This is close to valid for torque summations about the spin axis.
- (4) The rotational damping, C , is high so that the float's inertia is negligible.
- (5) Uncertainty sources are actual float motions which are caused by uncertain torque inputs (M_N) and electrical noise (x_N) in signal generator.
- (6) The suspension is tuned by selection of the feedback compensator $CH(s)$. The reasons for including a factor equal to the damping will be explained later.

With the above assumptions, the system can be modeled by the block diagram of Figure D-2. The following quantities are defined.

- M = the applied torque to be measured
- M_N = noise torques applied to float
- M_E = torque error caused by elastic restraint
- M_R = torque applied by rebalance
- M_M = measurement torque. Ideally $k_x = 0$ so that measuring the current gives the correct rebalance torque at steady-state.
- M_S = total torque applied to float
- c = rotational damping coefficient
- θ = float angular deviation from null
- l = length of float

x = actual position of float

x_N = uncertainty in position measurement

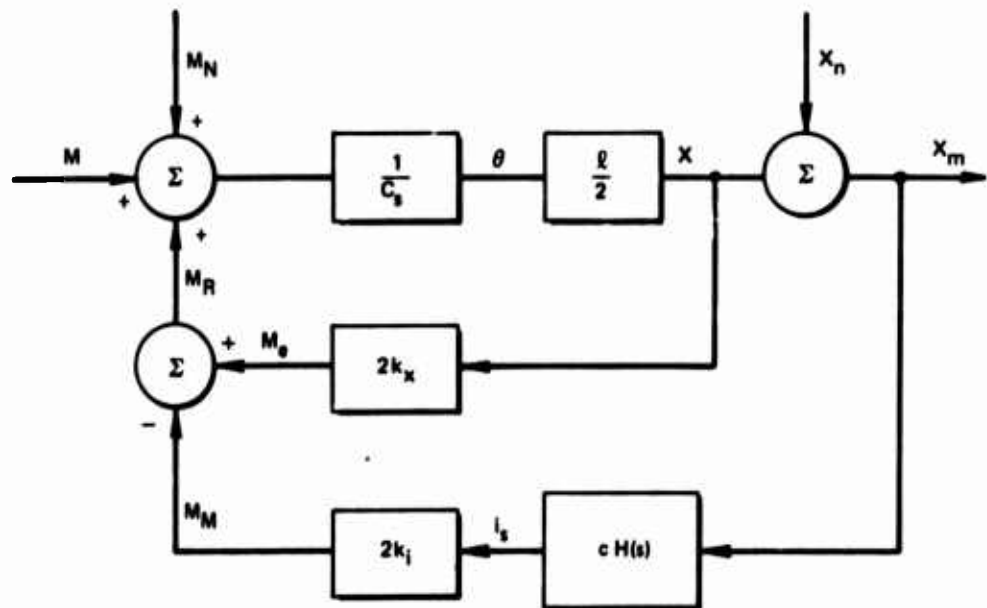


Figure D-2. Block diagram of idealized single loop of multisensor.

Write the feedback compensation as an integral with lead

$$cH(S) = \frac{ck_l (S+\alpha)}{S(S+\beta)} \quad (D-3)$$

The float position, x , is given by the transfer functions:

$$x(S) = \frac{(S^2 + \beta S) \frac{l}{c} \left[\frac{M + M_N}{2} \right] - k_I k_l (S + \alpha) x_N}{S^3 + S^2 \left[\beta - \frac{k_I l}{c} \right] + S \left[k_I k_l l - \frac{k_I l \beta}{c} \right] + k_I k_l l \alpha} \quad (D-4)$$

The measured torque is:

$$M_M(S) = \frac{k_I k_\ell^\ell (S+\alpha) (M+M_N) + 2k_I k_\ell C \left[S^2 + S \left(\alpha - \frac{k_x^\ell}{C} \right) - \frac{\alpha k_x^\ell}{C} \right] x_N}{S^3 + S^2 \left[\beta - \frac{k_x^\ell}{C} \right] + S \left[k_I k_\ell^\ell - \frac{k_x^\ell}{C} B \right] + k_I k_\ell^\ell \alpha} \quad (D-5)$$

D.4 LOOP COMPENSATION

Before proceeding to investigate the effects of noise sources and elastic restraint, the compensator $H(S)$ must be designed. For the multisensor feasibility with k_I of paragraph D.2 and $\ell = 5.6$ cm the following terms complete the torque loop:

$$k_\ell = 26.4 \text{ mA/cm-s-(dyn-cm-s)}$$

$$\alpha = 22.8 \text{ s}^{-1}$$

$$\beta = 173 \text{ s}^{-1}$$

With zero elastic restraint, the Bode plot for the closed loop accelerometer appears in Fig. D-3.

NOTE: The damping constant C has cancelled. (The physical C in the forward path is cancelled by the compensator's mathematical C .)

The system has a bandwidth of approximately 22 Hz (as described in Chapter 2, accelerometer loop bandwidth was reduced to 0.8 Hz).

D.5 DISCUSSION OF TRANSFER FUNCTIONS

For systems with typical bandwidth and damping constant, the elastic restraint, k_x , has only a small effect on the poles. Assume $C = 2.5 \times 10^5$ dyn-cm-s and parameters used in feasibility instrument. Referring to (D-5) and performing the calculations:

$$\beta - \frac{k_x^\ell}{C} = 173 - 2 \simeq 173 \simeq \beta$$

$$k_I k_\ell^\ell - \frac{k_x^\ell \beta}{C} = 1.41 \times 10^4 - 320 \simeq 1.41 \times 10^4 \simeq k_I k_\ell^\ell$$

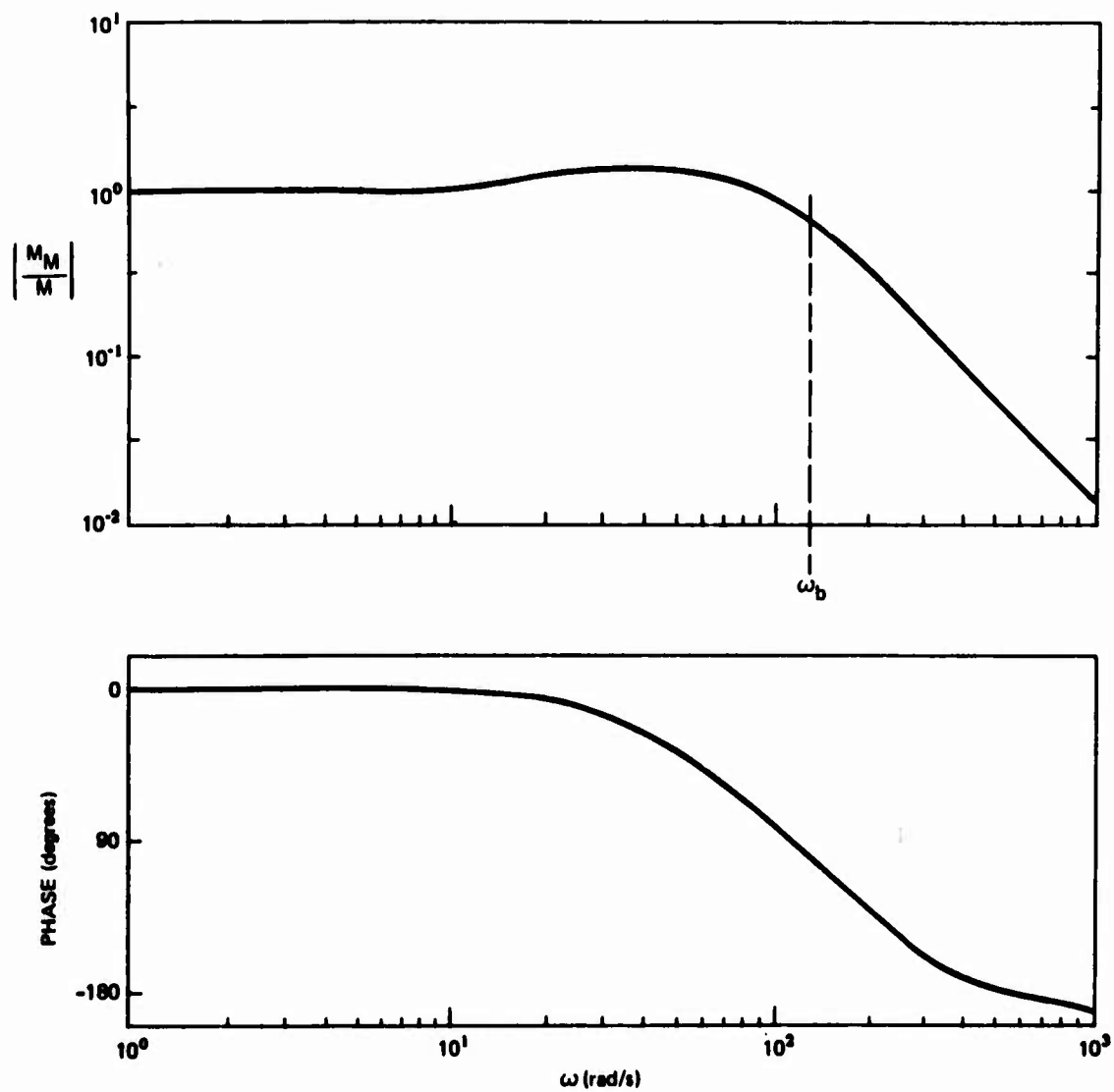


Figure D-3. Bode plot measured versus applied torque for multisensor accelerometer.

Thus, for systems with higher damping, elastic restraint can be ignored in the denominator. (Accelerometer loops will have higher damping constants.) If k_x affects poles, α , β , and k_l can be adjusted to maintain pole position. Thus, for systems where inertia can be neglected, if a desired response is given by $H(S)$ and the physical C is changed, one only need change the constant in the feedback loop proportionately.

For a given pole placement (i.e., given $HC(S)$), the float position is proportional to the applied torques but inversely proportional to the damping constant. High damping results in small motion so that the motions to be measured become comparable to the SG noise and resolution problems must be considered. The float's actual position is proportional to the SG noise input with no dependence on damping. The float's position does not depend on elastic restraint.

Referring to the measured torque (D-5), the measured torque is proportional to the applied torques with no dependence on damping constant. The interesting term is the dependence of measured torque on the signal generator noise input. With typical elastic restraint, the measured torque caused by SG uncertainty is proportional to the damping. For typical systems

$$\alpha - \frac{k_x l}{C} \simeq \alpha$$

and higher derivatives have a larger effect on rebalance noise (see paragraph D.5).

Since proposed accelerometer loops could have rotational damping three to four orders of magnitude higher than conventional measurement loops unless consideration is given to float shaping, the influence of the signal generator noise and the elastic restraint will be studied further.

D.6 MEASURED TORQUE UNCERTAINTY CAUSED BY SG NOISE IN THE FEASIBILITY INSTRUMENT

Consider the torque summation about the spin axis which is essentially decoupled from motions about the other axes. The following values are summarized for the multisensor feasibility instruments originally designed.

$$\begin{aligned}
\alpha &= 22 \text{ s}^{-1} \\
\beta &= 173 \text{ s}^{-1} \\
k_x &= 8.2 \times 10^4 \text{ dyn-cm/cm} \\
k_I &= 95.4 \text{ dyn-cm/mA} \\
k_\ell &= 26.4 \frac{\text{mA}}{\text{cm-s} (\text{dyn-cm-s})} \\
C &= 2.5 \times 10^8 \text{ dyn-cm-s}
\end{aligned}$$

SG noise with no float motion was experimentally described in measurements from 0.1 Hz to 50 Hz as white noise with spectrum of the float angle

$$\phi_\theta(S) = 3.3 \times 10^{-20} \text{ rad}^2/\text{rad/s} \quad (\text{D-6a})$$

which corresponds to 1 milliarc s measured from 0.1 to 50 Hz. Convert to position from angle with $\ell = 5.6 \text{ cm}$ gives the spectrum of x_N

$$\phi_{x_N}(S) = 2.59 \times 10^{-19} \frac{\text{cm}^2}{\text{rad/s}} \quad (\text{D-6b})$$

With known input spectrum and transfer function, the output spectrum can be determined. From the output spectrum, rms values of the expected values are determined. Table D-1 tabulates the rms measurement torque uncertainties for several conditions. Damping ratios of $C = 2.5 \times 10^5$ and $2.5 \times 10^8 \text{ dyn-cm-s}$ are compared for models with the estimated elastic restraint and zero elastic restraint.

The numerical examples which were tabulated for a loop whose bandwidth is 22 Hz demonstrates that the rms rebalance noise caused by the signal generator uncertainty is proportional to the damping constant for a given bandwidth. The presented data can be transformed to other bandwidths since the rms torque noise is proportional to the bandwidth to the three halves power. For damping constants of $2.5 \times 10^8 \text{ dyn-cm-s}$ which is representative of the feasibility instrument, the elastic restraint has little effect on the rebalance torque noise. For the

presently configured feasibility instrument with 0.8 gm-cm pendulosity, the rms noise is 0.12 gravity, a relatively high number which leads to the following questions:

- (1) What are the effects of the torque noise on stability testing of the feasibility instrument?
- (2) What are the implications for actual instrument design?

TABLE D-1. RMS TORQUE UNCERTAINTIES CAUSED BY SG NOISE.

| C (dyn-cm-s) | k_X dyn-cm cm | F_B (s ⁻¹) | rms M_M dyn-cm |
|-------------------|-----------------------|-----------------------------|---------------------|
| 2.5×10^5 | 0 | ∞ | 0.094 |
| 2.5×10^5 | 8.2×10^4 | ∞ | 0.094 |
| 2.5×10^6 | 0 | ∞ | 94 |
| 2.5×10^6 | 8.2×10^4 | ∞ | 94 |

Because of the coupling between the gyro torquer and the radial transducer, the effective noise in the signal was larger than that used in the above analyses. The loop bandwidth was reduced to 0.7 Hz and the loop output was filtered externally by an analog filter with 0.02 Hz bandwidth.

Very low frequency or steady-state null shifts do not appear in the spectra (D-6a). Using (D-5) to relate the measured torque to the signal generator null output at steady-state:

$$M_M = 2k_X X_N \quad (D-7)$$

With a pendulosity of 0.8 gm-cm and a design goal of 100 μ g bias stability, the drift in the measured torque must be less than 0.08 dyn-cm. To allow for other bias sources, the torques calculated from (D-7) should be less than 0.08. For this discussion 0.05 dyn-cm is selected. With $k_X = 8.2 \times 10^4$ dyn-cm/cm (the feasibility instrument tuned for 2g with no signal generator tuning), signal generator drift

of less than 3×10^{-7} cm is required. With $k_x = 10^3$ dyn-cm/cm (the feasibility instrument with signal generator tuning), 3×10^{-5} cm is required. Note that these results have no dependence on the damping constants. With series parallel tuning (SECTION 2), null shift (ΔX_N) can be related to capacitor changes (ΔC) by the approximate relation

$$\frac{\Delta X_N}{g_0} \approx \frac{\Delta C}{C_0}$$

where

C_0 is the nominal capacitance

g_0 is the nominal magnet pole face clearance

For the feasibility instrument g_0 is 0.015 cm and C is approximately 0.038 μ F. Thus capacitance changes must be less than 0.76 pF and 76 pF for the untuned and tuned signal generator respectively. These capacitor changes are relative changes. If all capacitors change identically, no shift occurs. The implications of capacitor changes are discussed in paragraph 3.6.

The following considerations of the signal generator noise on multisensors for flight use are discussed.

- (1) Elimination of capacitance sensitivity (this has been covered in the previous discussion of feasibility tests).
- (2) Effects of elastic restraint on velocity error; and
- (3) The trade between damping constant and loop bandwidth.

Since accelerometers are used to determine velocity, accelerometer specifications should be converted to velocity so that meaningful evaluation may be accomplished. If one desires 50 ppm accelerometer response and if a nominal operating velocity of 300 mile per hour is assumed, the velocity error must be less than 0.7 cm/s (50 ppm multiplied by 300 mile per hour).

Velocity errors caused by elastic restraint are discussed. Referring to Figure D-2 and Equation (D-4) and (D-5), and omitting signal generator and input noise; the error in the measurement torque is derived:

$$M_E = M - M_M \quad (D-8)$$

$$\frac{M_E}{M} = \frac{s^3 + s^2 \left(\beta - \frac{k_X^\ell}{C} \right) - s \frac{k_X^{\ell\beta}}{C}}{s^3 \left[\beta - \frac{k_X^\ell}{C} \right] s^2 + \left[k_I k_\ell - \frac{k_X^{\ell\beta}}{C} \right] s + k_I k_\ell \alpha}$$

For steady-state torque input (acceleration input), the measurement error is zero at steady-state; however, the integral of torque is proportional to velocity. For a step input in M , (corresponding to one gravity) the steady-state velocity error is:

$$\text{Steady-state velocity error} = \frac{\beta k_X (P_a)}{\alpha k_I k_\ell C}$$

where the torque M has been written as pendulosity times acceleration. With the tuning for 22 Hz bandwidth and compensator elastic restraint of 1000 dyn-cm, the steady-state velocity error for a one-gravity input in acceleration is

$$\text{Velocity steady-state} = \frac{2.5 \times 10^3 \text{ (dyn-cm-s)}}{C}$$

with damping constant of 5×10^5 dyn-cm-s or greater, the steady-state velocity error is less than 0.005 cm/s which is much less than the 0.7 cm/s equivalent to 50 ppm navigation.

The rebalance torque noise resulting from the signal generator noise is estimated at 94 dyn-cm (Table D-1) or 0.12 g with 0.8 gm-cm pendulosity. This calculation is based on the 22 Hz measurement bandwidth and the signal generator spectrum of (D-6). For the given loop dynamics, the integral of the rebalance torque is proportional to the flight velocity. With 0.8 gm-cm, the rms velocity is 1.1 cm/s which is greater than the 0.7 cm/s comparable to 50 ppm performance. In addition, calibration is difficult because the rms noise is three orders of magnitude greater than the calibration accuracy (50 ppm). Since bandwidth reduction is undesirable for operational systems, the multisensor transverse axes should be designed with damping an order of magnitude smaller, a suggestion which is explored in paragraph 3.8 and Section 4.

APPENDIX E

CONVECTION TORQUES ABOUT TRANSVERSE AXIS

E.1 SUMMARY

This Appendix demonstrates the convection pattern resulting from an end-to-end thermal gradient and the effects on accelerometer stability in the multisensor. For the multisensor feasibility instruments thermally induced torques of the order of 5 dyn-cm/g-°F (°F of end-to-end thermal difference) can be expected.

E.2 DISCUSSION

An approximation of the effects of an end-to-end thermal gradient in the multisensor is obtained for the model of a cylindrical float depicted in Figure E-1. Similar analyses have been conducted about the cylinder axis. The following assumptions are made:

- (1) Fluid inertia may be neglected;
- (2) Using the coordinates of Figure E-1, a linear thermal gradient exists along the float so that the temperature $T(Z)$ at any point in the fluid is given by:

$$T = T(Z) = T_0 \left(1 - \frac{\Delta T z}{l/2} \right) \quad (E-1)$$

where:

T_0 = mean temperature;

ΔT = temperature difference between ends

- (3) The cylindrical float is coaxial with the cylindrical case;
- (4) Gravity is perpendicular to the float's axis as shown in Figure E-1;



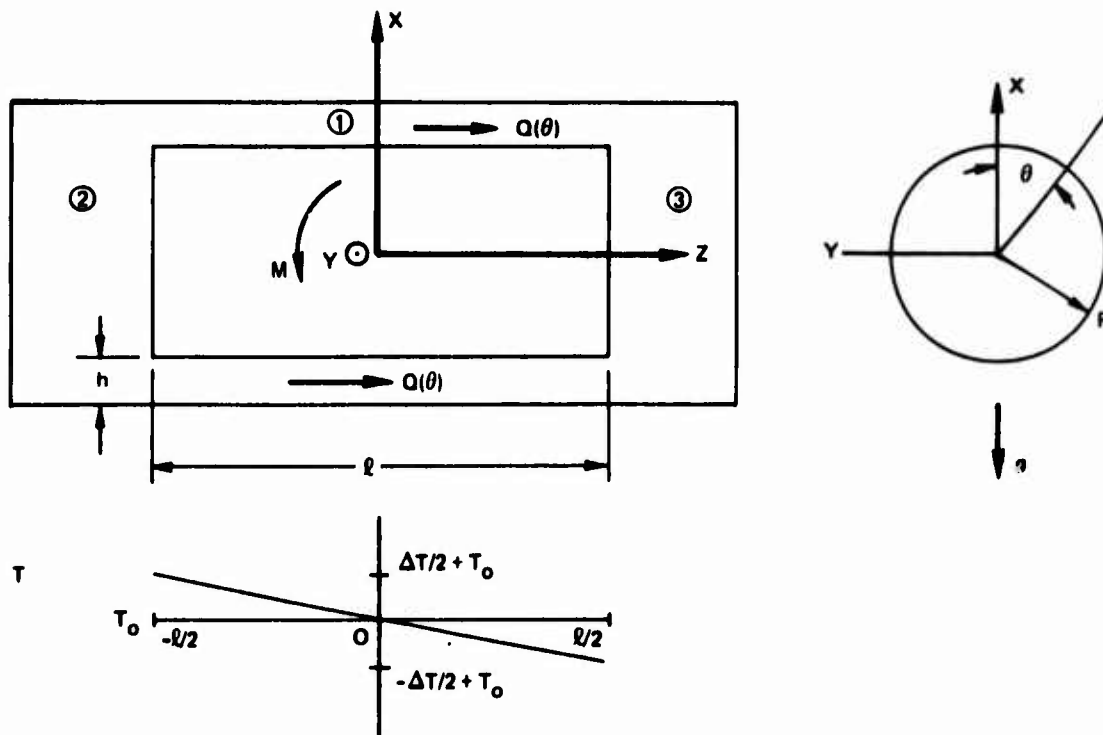


Figure E-1. Coordinates for convection analysis.

- (5) The fluid flow can be divided into three regions of interest: region 1 is an annulus of radius R , length l and thickness h . Flow in the annulus is in the Z direction only, an assumption whose validity will be demonstrated later. Assuming h much smaller than l and R , the pressure gradient in the annulus is:

$$\frac{\partial P}{\partial Z} = \frac{-12 \mu Q(\theta)}{h^3} \quad (E-2)$$

where:

P = pressure is a function of axial position Z and circumferential angle θ

Q = volume flow/unit length in Z direction and a function of θ

μ = absolute viscosity which is assumed uniform

- (6) The end volumes are large so that viscous effects are small. The pressure gradient then depends upon gravity. With the temperature gradient defined by (E-1), the pressure gradient in region 2 is:

$$\frac{\partial P}{\partial X} = \rho_O g \left(1 + \frac{k_T \Delta T}{2} \right) \quad (E-3)$$

where:

g = specific force

k = fluid volume gradient

ρ_O = fluid density at reference condition

In region 3, the pressure gradient is given by:

$$\frac{\partial P}{\partial X} = \rho_O g \left(1 - \frac{k_T \Delta T}{2} \right) \quad (E-4)$$

Proceed to solve for the fluid pressure. Circumnavigating the float by the path depicted in Figure E-1, the path integral must be zero:

$$\rho \operatorname{div} P \cdot d\bar{x} = 0 \quad (E-5)$$

Substituting (E-2), (E-3) and (E-4) into (E-5), allows solution for $Q(\theta)$

$$Q(\theta) = - \frac{h^3 k_T \Delta T \rho_O g R \cos \theta}{12 \mu \ell} \quad (E-6)$$

Integration of (E-4) gives the pressure gradient, at the left end:

$$P \left(-\frac{\ell}{2}, \theta, R \right) = P_O + \rho_O g R \left(1 + \frac{k_T \Delta T}{2} \right) (1 - \cos \theta) \quad (E-7)$$

where

$$X = R \cos \theta$$

and where P_O is a reference pressure which need not be determined for this work.

Integration of (E-2) with the boundary condition (E-7) gives the pressure in the annulus:

$$P(\theta, z) = P_0 + \rho_0 g \left(1 + \frac{k\Delta T}{2} - \rho_0 g R \cos \theta + \left[\frac{k_T \Delta T}{\ell} \rho_0 g R \cos \theta \right] z \right) \quad (E-3)$$

Note that (E-8) is a steady-state solution for the pressure distribution and that (E-6) is convection path. Return and verify assumption 5 where circumferential flow in the annulus was assumed zero. For flow along the circumference:

$$\frac{12 \mu Q_R}{h^3} = -\frac{1}{R} \frac{\partial P}{\partial \theta} + \rho_0 \left(1 - \frac{k_T \Delta T}{\ell} z \right) g \sin \theta \quad (E-9)$$

Substitution of (E-9) into (E-8) gives O_R equal zero which verifies the assumption.

Since the pressure distribution and the flow are known, the forces and moments acting upon the float can be determined.

The force in the vertical (X) direction:

$$F_X = \rho_0 g \pi R^2 \ell \quad (8.10)$$

In the (Y) direction

$$F_Y = 0 \quad (E.11)$$

and in the axial direction

$$F_Z = 0 \quad (E.12)$$

Since the flow for positive X is the negative of the flow for negative X (the $\cos \theta$ in (E-6)), the solution for the bottom half is antisymmetric with respect to the solution for the upper portion so that (E-12) results.

From the pressure, the torque induced by normal pressure forces is derived. For this symmetric example, all torques are about the Y axis. The contribution from the ends is:

$$\frac{M_{\text{end}}}{\Delta T} = \frac{\pi R^4 k_T \rho_O g}{4} \quad (\text{E-13})$$

The torques generated by the normal pressures in the annulus is:

$$\frac{M_{\text{ann}}}{\Delta T} = \frac{\pi}{12} \rho_O g R^2 \ell^2 k_T \quad (\text{E-14})$$

The torques caused by the pressures in the annulus and in the ends are in opposite directions, thereby, tending to cancel one another. Since the ends were assumed large so that flow rates were small, no viscous shear force is contributed in the end regions. In the annulus, the shear stress exerted by the fluid on the float is:

$$\tau_z = \frac{6\mu Q(\theta)}{h^2} \quad (\text{E-15})$$

and the torque is:

$$\frac{M_{\text{vis}}}{\Delta T} = \frac{\pi}{2} h R^3 k_T \zeta_O g \quad (\text{E-16})$$

Estimate the effect of thermal gradient on a multisensor accelerometer where the following parameters are from the feasibility instrument:

$$R = 2 \text{ cm}$$

$$\ell = 4 \text{ cm}$$

$$k_T = 4 \times 10^{-4}$$

$$g = 980 \text{ cm/s}^2$$

$$\rho_O = 2.655 \text{ gm/cm}^3$$

The estimated torques are:

$$\frac{M_{\text{end}}}{\Delta T} = 13 \text{ dyn-cm/}^\circ\text{F}$$

$$\frac{M_{\text{ann}}}{\Delta T} = -17 \text{ dyn-cm/}^\circ\text{F}$$

The viscous torques are negligible since $h \ll l$ or R . With $h = 0.0254$ cm, the viscous torque is:

$$\frac{M_{vis}}{\Delta T} = 0.3 \text{ dyn-cm/}^{\circ}\text{F}$$

With pendulosity of 800 dyn-cm at one gravity, the scale factor sensitivity is:

$$SF \simeq \frac{4}{800} = 5000 \frac{\text{ppm}}{^{\circ}\text{F}}$$

APPENDIX F

STATIC CROSS-COUPLING IN MULTISENSORS

F.1 SUMMARY

Based on physical phenomena and misalignment of forces and torques, an error model for multisensor 1 g and earth-rate tests is formulated. The model will be used for locating instrument axes and determining coupling between accelerometer and gyro functions.

The model indicates that large pendulous unbalance along OA appears as acceleration-sensitive drift which previous multisensor tests demonstrated to be in the range of typical gyros.

For calibrating the accelerometer, precise knowledge of the current-torque relation is not required; that is, signal-acceleration calibration can be performed directly. The accelerometer output contains a scale factor which should be set to tune out translational motion effects. Cross-coupling effects will determine the position of the accelerometer IA so that the axis will not coincide with IRA or the gyro IRA.

F.2 MULTISENSOR MODEL AT STEADY-STATE

As a first approximation, only steady-state will be considered. Second-order terms will be neglected. At steady-state, Newton's laws must be satisfied for the rotational motion

$$\Sigma \underline{M} = \underline{M}_M + \underline{M}_g + \underline{M}_{g^2} + \underline{M}_R + \underline{M}_B = \omega \times \underline{H}_S \quad (F-1)$$

and translational motion

$$\Sigma \underline{F} = \underline{F}_M + \underline{F}_B + \underline{F}_R = 0 \quad (F-2)$$

where:

- \underline{F}_B = buoyancy
- \underline{F}_M = magnetic suspension force
- \underline{F}_R = reaction force
- \underline{M}_B = buoyant torque
- \underline{M}_g = acceleration-proportional torques
- \underline{M}_{g^2} = acceleration-squared torques
- \underline{M}_M = magnetic-suspension torques
- \underline{M}_R = reaction torque
- ω = angular velocity of float ω/IS
- \underline{H}_S = angular momentum of wheel

Note, since $\underline{\omega} = \omega_E = 7.27 \times 10^{-5}$ rad/s, many $I\omega_x\omega_y$ terms have been neglected.

Determine the vectors in Equation (F-1) and (F-2) for the spin, input and output axes. Define the coordinate triad (S, I, O). The rate of change of angular motion is determined:

$$\underline{\omega} \times \underline{H}_S = \begin{bmatrix} 0 & -\omega_O & \omega_I \\ \omega_O & 0 & \omega_S \\ -\omega_I & \omega_S & 0 \end{bmatrix} \begin{bmatrix} H_S \\ H_I \\ H_O \end{bmatrix} = \begin{bmatrix} \omega_I H_O - \omega_O H_I \\ \omega_O H_S - \omega_S H_O \\ \omega_S H_I - \omega_I H_S \end{bmatrix} \quad (F-3)$$

where H is written with 3 components since float and reference axes do not coincide. H_I and H_O are assumed small.

In float coordinates, torques proportional to acceleration are determined from

$$\underline{M}_g = \begin{bmatrix} Pa_I - U_I a_O \\ -Pa_S + U_S a_I \\ U_I a_S - U_S a_I \end{bmatrix} \quad (F-4)$$

where:

a = acceleration

U_I, U_S = mass unbalance (small) along input and spin axes

P = pendulosity (large mass unbalance) along output axis

The g^2 terms are

$$\frac{M}{g^2} = \begin{bmatrix} -k_{II}a_Ia_O - k_{IS}a_Sa_O - k_{IO}a_O^2 + k_{OI}a_I^2 + k_{OS}a_Sa_I + k_{OO}a_Oa_I \\ -k_{OO}a_Oa_S - k_{OI}a_Ia_S - k_{OS}a_S^2 + k_{SO}a_O^2 + k_{SI}a_Ia_O + k_{SS}a_Sa_O \\ -k_{SS}a_Sa_I - k_{SO}a_Oa_I - k_{SI}a_I^2 + k_{IS}a_S^2 + k_{IO}a_Oa_S + k_{II}a_Sa_I \end{bmatrix} \quad (F-5)$$

Compliance terms are usually small (15 meru/ g^2 for example); thus, compliance multiplied by another small quantity is negligible.

Define the vector of reaction torques

$$\underline{M}_R = \begin{bmatrix} M_{RS} \\ M_{RI} \\ M_{RO} \end{bmatrix} \quad (F-6)$$

and a vector of buoyancy torques

$$\underline{M}_B = \begin{bmatrix} M_{BS} \\ M_{BI} \\ M_{BO} \end{bmatrix} \quad (F-7)$$

The reaction forces which are caused by magnetic misalignments and flex leads are:

$$\underline{F}_R = \begin{bmatrix} F_{RS} \\ F_{RI} \\ F_{RO} \end{bmatrix} \quad (F-8)$$

and the buoyancy forces:

$$\underline{F}_B = \begin{bmatrix} B_S a_S \\ B_I a_I \\ B_O a_O \end{bmatrix} \quad (F-9)$$

where B is the buoyancy along the indicated axis. As discussed in Appendix A, this representation of buoyancy is probably an oversimplification.

Neglecting elastic restraints, a valid assumption with null seeking suspensions and nonlinearities, the magnitude of the forces and torques is proportional to the secondary current in the device. Because of forcer misalignments magnetic anomalies, and float-case misalignments, the magnetic forces do not align themselves perfectly with the float's S-I-O-triad. Thus, the forces and torques may be expressed by the matrix relation:

$$\begin{bmatrix} M_S \\ M_I \\ F_S \\ F_I \\ M_O \\ F_O \end{bmatrix} = \begin{bmatrix} \bar{r}_{11} & \bar{r}_{12} & r_{13} & r_{14} & \bar{r}_{15} & \bar{r}_{16} \\ r_{21} & r_{22} & \bar{r}_{23} & \bar{r}_{24} & \bar{r}_{25} & \bar{r}_{26} \\ r_{31} & r_{32} & \bar{r}_{33} & \bar{r}_{34} & \bar{r}_{35} & \bar{r}_{36} \\ \bar{r}_{41} & \bar{r}_{42} & r_{43} & r_{44} & \bar{r}_{45} & \bar{r}_{46} \\ \bar{r}_{51} & \bar{r}_{52} & \bar{r}_{53} & \bar{r}_{54} & r_{55} & \bar{r}_{56} \\ \bar{r}_{61} & \bar{r}_{62} & \bar{r}_{63} & \bar{r}_{64} & \bar{r}_{65} & r_{66} \end{bmatrix} \begin{bmatrix} i_{S1} \\ i_{S2} \\ i_{S3} \\ i_{S4} \\ i_{S5} \\ i_{S6} \end{bmatrix} \quad (F-10)$$

where the overline indicates a small quantity (if forcers were ideal these quantities would be zero) and i = current in forcer axis indicated in Figure F-1.

Equation (F.10) is very general and includes all possible linear cross-couplings.

Incorporate Equation (F.1) through (F.10) to determine the currents in the radial forcers and gyro torquer.

$$\begin{bmatrix} i_{S1} \\ i_{S2} \\ i_{I1} \\ i_{I2} \\ i_O \\ i_{AX} \end{bmatrix} = \begin{bmatrix} \bar{q}_{11} & q_{12} & q_{13} & \bar{q}_{14} & \bar{q}_{15} & \bar{q}_{16} \\ \bar{q}_{21} & q_{22} & q_{23} & \bar{q}_{24} & \bar{q}_{25} & \bar{q}_{26} \\ q_{31} & \bar{q}_{32} & \bar{q}_{33} & q_{34} & \bar{q}_{35} & \bar{q}_{36} \\ q_{41} & \bar{q}_{42} & \bar{q}_{43} & q_{44} & \bar{q}_{45} & \bar{q}_{46} \\ \bar{q}_{51} & \bar{q}_{52} & \bar{q}_{53} & \bar{q}_{54} & q_{55} & \bar{q}_{56} \\ \bar{q}_{61} & \bar{q}_{62} & \bar{q}_{63} & \bar{q}_{64} & \bar{q}_{65} & q_{66} \end{bmatrix}$$

$$\times \begin{bmatrix} -Pa_I + \overline{U_I a_O} - \bar{M}_{RS} - \bar{M}_{BS} - \bar{M}_{g^2 S} + \overline{\omega_I H_O} - \overline{\omega_O H_I} \\ + Pa_S - \overline{U_S a_I} - \bar{M}_{RI} - \bar{M}_{BI} - \bar{M}_{g^2 I} + \overline{\omega_O H_S} - \overline{\omega_S H_O} \\ - \overline{B_S a_S} - \bar{F}_{RS} \\ - \overline{B_I a_I} - \bar{F}_{RI} \\ + \overline{U_S a_I} - \overline{U_I a_S} - \bar{M}_{RO} - \bar{M}_{BO} - \bar{M}_{g^2 O} + \overline{\omega_S H_I} - \overline{\omega_I H_S} \\ - \overline{B_O a_O} - \bar{F}_{RO} \end{bmatrix}$$

where the overline indicates small quantities and

$$q = \underline{r}^{-1}$$

For an ideal instrument, the overlined terms are small and the following relations are based on geometric considerations.

$$q_{12} \simeq -q_{22} \quad (F-12a)$$

$$q_{13} = q_{23} \quad (F-12b)$$

$$q_{14} \simeq -q_{41} \quad (F-12c)$$

$$q_{34} = q_{44} \quad (F-12d)$$

The approximate equal signs of Equations (F-12a) and (F-12c) are caused by the instrument's pendulosity which causes the geometric float center to differ from the center of gravity so that slightly different moment arms exist for the two forcers.

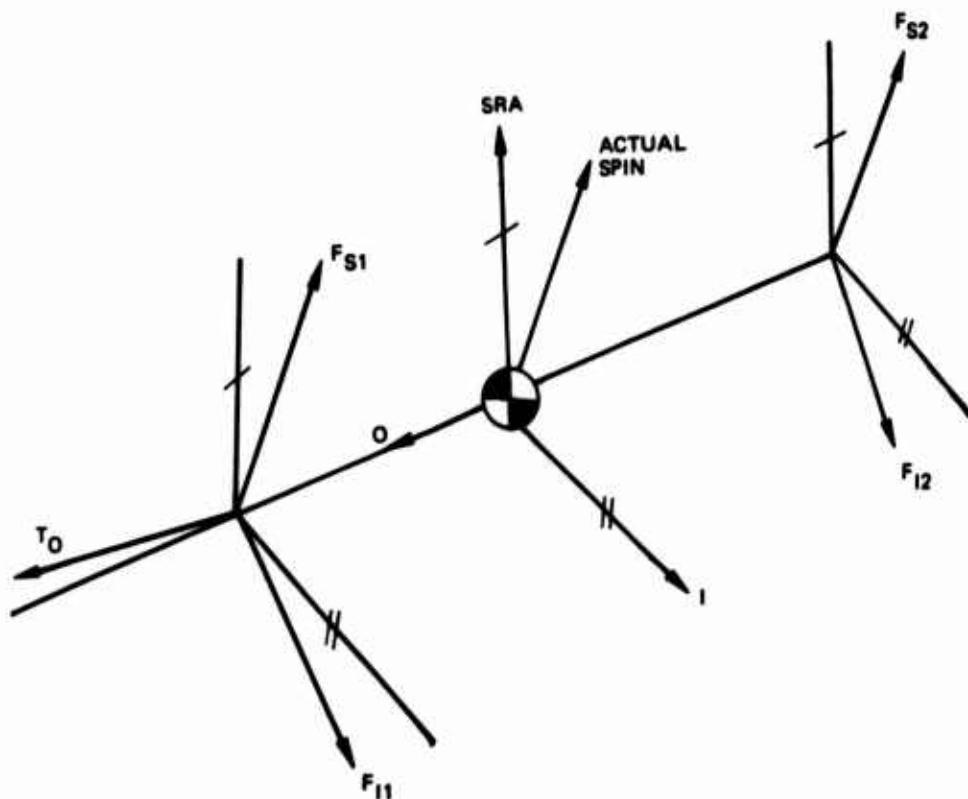


Figure F-1. Schematic of forces and torques in multisensor.

Previous multisensor analysis has assumed that the accelerometer readout for acceleration along the input axis was the rebalance torque about the spin axis which is roughly determined by the radial suspension forces exerted along the input axis. Therefore, define the accelerometer output signal S_I as follows

$$S_I = i_{I1} - k_I i_{I2} \quad (F-13)$$

where k_I is a constant whose selection will be discussed further. Substitution of Equation (F-11) into (F-13) results in

$$\begin{aligned}
S_I = & (q_{31} - k_I q_{41}) \quad (-Pa_I + \overline{U_I a_O} - \overline{M_{RS}} - \overline{M_{BS}} - \overline{M_{g^2 S}} + \omega_I \overline{H_O} - \overline{\omega_O H_I}) \\
& + (\overline{q}_{32} - k_I \overline{q}_{42}) \quad (Pa_S + \omega_O H) \\
& + (q_{34} - k_I q_{44}) \quad (-\overline{B_I a_I} - \overline{F_{RI}}) \\
& + (\overline{q}_{35} - k_I \overline{q}_{45}) \quad (-\omega_I H)
\end{aligned}
\tag{F-14}$$

where second-order terms have been neglected.

Expressions similar to Equation (F-14) can be derived for the currents i_{S1} and i_{S2} and for the gyro torquer current

$$\begin{aligned}
i_O = & q_{55} \quad (-\omega_I H_S + \overline{U_S a_I} - \overline{U_I a_S} - \overline{M_{RO}} - \overline{M_{BO}} - \overline{M_{g^2 O}} + \omega_S H_O) \\
& - \overline{q}_{51} \quad (Pa_I) + \overline{q}_{52} \quad (\omega_O H + Pa_S)
\end{aligned}
\tag{F-15}$$

F.3 COMMENTS

The position of the axes and the cross-couplings at steady-state do not depend on the signal generators (neglecting SG null shifts, see Appendix C). At steady-state Newton's laws, Equations (F-1) and (F-2) must be satisfied. Thus, in Equations (F-14) and (F-15), one is concerned only with the steady-state current and not with the path the current followed to reach said level.

In the gyro torquer current Equation (F-15), the cross-coupling \overline{q}_{52} will cause the instrument's measured input axes to be located at a position other than perpendicular to the spin axis and to the axis of symmetry of the float. (This observation pertains to all gyros.) Because of the cross-coupling \overline{q}_{51} and \overline{q}_{52} , the pendulosity along the output axis appears as a gyro acceleration drift coefficient, Equation (E-15). Measurements of the multisensor feasibility instrument's acceleration drifts were in the same range as those for similar instruments so that one may conclude these couplings are small.

Consider the accelerometer signal S_I , Equations (F-13) and (F-14). Any value of k_I (except that which zeroes or makes small the first expression in Equation (F-14)) will give acceleration information at steady-state. Thus, the precise relation between current and torque need not be determined. The relation between current and acceleration is sufficient. The current weighting factor should be selected so that

$$(q_{34} - k_I q_{44}) = 0$$

(F-16)

This minimizes the effects of translational motion on the accelerometer readout (F-14), while Equation (F-12c) indicates acceptable gain for Pa_I . Thus, error torques associated with a change in flotation temperature are greatly reduced since $B_I a_I$ is usually large compared to other thermal error sources. The modes associated with the transient motion might be slower than the rotational modes (see Appendix B). Selecting k_I according to Equation (F.16) eliminates the slow modes from the accelerometer signal S_I although the slow mode remains in the float's actual behavior.

Proper k_I could be chosen by:

- (1) Raising the instrument temperature uniformly, and/or
- (2) Moving the float translationally and allowing return to equilibrium. k_I is adjusted until the translational effects are not seen in S_I .

The a_O and a_S terms reflect that the multisensor input axis will not be on IRA and probably will not coincide with the gyro input axis. Additionally, the accelerometer signals will contain rate information because of the coupling phenomena. Multisensor cross-coupling tests will attempt to evaluate these effects.

REFERENCES

1. Wrigley, W., W. Hollister, W. Denhard, Gyroscopic Theory, Design, and Instrumentation, MIT Press, Cambridge, Massachusetts, 1969.
2. Miller, B., "Light, Compact Navigator Designed", Aviation Week and Space Technology, McGraw-Hill Book Company, New York, 9 February 1970, pp. 51-55.
3. Miller, B., "Guidance Unit Links Sensor Ideas", Aviation Week and Space Technology, McGraw-Hill Book Company, New York, 13 April 1970, pp. 48-53.
4. Miller, B., "Inertial Navaid Features New Multisensors", Aviation Week and Space Technology, McGraw-Hill Book Company, New York, 11 December 1971, pp. 44-46.
5. Weinberg, M., An Analytical Description of Torques and Forces Exerted on Cylindrical Float During Float Motion, The Charles Stark Draper Laboratory, Inc., (CSDL), Report C-4712, August 1976.
6. Weinstock, H., The Effects of Gyroscopic Unbalance Torques, CSDL Report E-1798, January 1962.
7. Draper, C.S., L. Trilling, W.G. Denhard, R.H. Wilkinson, Torque Induced by Convective Effects Acting on a Cylinder Floated in a Thin Layer of Viscous Fluid", CSDL Report R-587.
8. Lawson, R., M. Weinberg, Multisensor Feasibility Evaluation Test Outline, submitted to AFAL as Contractual Obligation, 25 February 1976.
9. Koenigsberg, W.D., Spectral Analysis of Random Signals-Techniques and Interpretation, CSDL Report E-2771, June 1973.
10. Truncala, A., W. Koenigsberg, R. Harris, Spectral Density Measurements of Gyro Noise, CSDL Report E-2641, February 1976.
11. Salamin, E., G.J. Bukow, Large Space Telescope Control Moment Gyro Test Program, CSDL Report R-846, July 1975.